This is to certify that the
dissertation entitled

COMBUSTION AND CHEMICAL KINETICS STUDY OF JET
FUEL, BIOGAS AND SOLID FUEL IN DIFFUSION FLAMES

presented by

Saeid Jahangirian

has been accepted towards fulfillment
of the requirements for the

Doctoral degree in Mechanical Engineering

Major Professor's Signature

10/26/09

Date

COMBUSTION AND CHEMICAL KINETICS STUDY OF JET FUEL, BIOGAS AND SOLID FUEL IN DIFFUSION FLAMES

By

Saeid Jahangirian

A DISSERTATION

Submitted to
Michigan State University
in partial fulfillment of the requirements
for the degree of

DOCTOR OF PHILOSOPHY

Mechanical Engineering

2009

ABSTRACT

COMBUSTION AND CHEMICAL KINETICS STUDY OF JET FUEL, BIOGAS AND SOLID FUEL IN DIFFUSION FLAMES

By

Saeid Jahangirian

This study is organized into three parts focusing on jet fuel combustion, biogas combustion, and solid fuel microgravity combustion.

In Part I, combustion and chemical kinetics of high molecular weight hydrocarbon blends at the onset of soot formation are studied. The chemical structure of ethylene counterflow diffusion flames doped with trace amounts of jet fuel or two promising jet fuel surrogates is analyzed by gas sampling via quartz microprobes and GC/MS. A dataset for the pyrolysis, oxidation and sooting behavior of jet fuel in diffusion flames is provided. The critical fuel decomposition products and soot precursors, such as acetylene, benzene and toluene, are compared to evaluate surrogate formulations. The data for C7-C12 alkanes are consistent with typical decomposition of large alkanes with both surrogates (6 and 2-component) showing good qualitative agreement with jet fuel in their pyrolysis trends. The acetylene profiles present a unique multimodal behavior. Good agreement between jet fuel and the surrogates is found with respect to critical soot precursors such as benzene and toluene.

In Part II, combustion and kinetics of biogas, which is a viable alternative gas turbine fuel, is modeled in premixed and non-premixed configurations. A modeling study is conducted on blends of CH_4 and CO_2 simulating biogas from digestion plants or

landfills to compare predictions for four non-sooting counterflow diffusion flames and to examine their thermal and chemical structure. In addition to evaluation of thermal influences of biogas CO_2, the chemical influences of CO_2 are quantified because CO_2 dilution through chemical effects is shown to reduce soot precursors, emissions of NOx and greenhouse gases even without flame temperature reduction.

In Part III, diffusion flames spreading near solid fuel surfaces are investigated numerically and analytically in 2-D domains for both unconfined and confined environments. A model of surface-attached solid fuel flames with weak convection is constructed. Flame spread over thin fuels is studied in a confined geometry because of its implications for fire safety in normal gravity. It is demonstrated that the buoyancy is suppressed in the MSU Narrow Channel Apparatus, which produces test conditions that can simulate conditions achieved in actual microgravity.

DEDICATION

اول دفتر به نام ایزد دانا

This book is dedicated to

my mother, Houra, my father, Hassan, and my wife, Tayebeh.

ACKNOWLEDGEMENTS

I express my sincere gratitude to my advisors, Dr. Indrek Wichman and Dr. Abraham Engeda, at Michigan State University for their continuous support, friendship and encouragement during my graduate studies. I gratefully thank Dr. Alessandro Gomez at Yale University, where a valuable part of this dissertation was conducted during a sabbatical leave from Michigan.

I am very grateful for having an exceptional doctoral committee and would like to sincerely thank Dr. Charles Petty and Dr. Farhad Jaberi, for their continual encouragement, and their valuable comments and criticisms.

I would like to gratefully acknowledge the financial support of AFOSR (Grant #FA9550-06-1-0018, Dr. Julian Tishkoff, Program Manager) and the supply of jet fuel from Dr. James (Tim) Edwards (Wright-Patterson Air Force Base). I also wish to express gratitude to the Microgravity Combustion Branch at NASA Glenn Research Center for funding this project under contract #NCC3-662. Financial support of the MSU Turbomachinery Laboratory for biogas research is greatly appreciated.

I would like to thank Dr. Sandra Olson and Dr. Fletcher Miller of the NASA Microgravity Combustion Division for their technical advice and their ongoing encouragement. Discussions with Dr. Charles McEnally in the Department of Chemical Engineering at Yale University are also acknowledged.

My journey through these years was much easier with the friendship of many friends and colleagues especially Mehdi Abarham.

Finally and most importantly, my deepest thanks to my wife, Tayebeh, for all her support and patience during the years I worked on my Ph.D. research. It was her encouragement, love, and passion that gave me strength and confidence to look for the best, pass all obstacles, and plan for reaching to great horizons.

TABLE OF CONTENTS

LIST OF TABLES

LIST OF FIGURES

Images in this dissertation are presented in color.

NOMENCLATURE

Abbreviations

NG	Natural gas
RNG	Renewable natural gas
LNG	Liquefied natural gas
BG	Biogas
GT	Gas turbine
GHG	Green house gas
PIV	Particle image velocimetry
LDV	Laser doppler velocimetry
LIF	Laser induced florescence
DLN	Dry low NOx
GC	Gas chromatography
MS	Mass spectroscopy
RR	Reaction rate
PAH	Polycyclic aromatic hydrocarbons
TSI	Threshold sooting index
CN	Cetane number
F-T	Fischer-Tropsch
$EICO_2$	Carbon dioxide emission index
AD	Anaerobic digestion

LHV	Lower heating value
EGR	Exhaust gas recirculation
SD	San Diego detailed reaction mechanism
SP	Stagnation plane
NCA	Narrow Channel Apparatus
ZGRF	Zero Gravity Research Facility at NASA
MCH	Methylcyclohexane
TMB	Trimethyl benzene

Symbols

φ	Global Equivalence ratio, $\varphi=(Air/Fuel)_{stoich}/(Air/Fuel)_{actual}$
C_P	Constant pressure specific heat, kJ/kg-K
H	Enthalpy, kJ/kg
S	Entropy, kJ/kg-K
S_L	Laminar flame speed, cm/s
s	Swirl number
S_T	Turbulent flame speed, cm/s
δ	Flame thickness, mm
a	Strain rate, 1/s
Da	Domköhler number
Ka	Turbulent Karlovitz number
α	Thermal diffusivity, m^2/s
V	Flow velocity, cm/s

ρ	Mixture density, kg/m^3
X	Mole fraction
Y	Mass fraction
R	Gas constant, kJ/kmol-K or radius, m
P	Pressure, atm
T	Temperature, K
z_f	Stoichiometric mixture fraction
L	Burner separation, mm
r	Radial coordinate, mm
z	Axial distance in counterflow burner, mm
g	Gravity level, 1g=9.8 m/s^2, 0g = 0 m/s^2
h	Gap spacing, cm
D	Diffusion coefficient, m^2/s
ν	Viscosity, m^2/s
V_{blow}	Fuel surface blowing velocity, cm/s
V_{buoy}	Buoyancy-induced velocity, cm/s
V_{diff}	Diffusive velocity, cm/s
V_{flow}	Forced flow velocity, cm/s
V_{therm}	Thermal expansion velocity, cm/s
v, V_y	Velocity in the y direction, cm/s
q''	Heat flux, W/cm^2, 0 = adiabatic
π	pi, 3.14159…..

u	Velocity in the x direction, cm/s

Superscripts

o	Standard-state

Subscripts

k, i	Species (components) in a mixture
F	Fuel
O	Oxidizer
FF	Fuel fraction in fuel inlet (surface)
OO	Oxidizer fraction in oxidizer inlet
f	Flame
ad	Adiabatic
ig	Ignition
∞	Far field value
cf	Cross flow
j	Jet flow
max	Maximum value
min	Minimum value
S	Surface, solid
mix	Mixture

Chapter 1 Introduction

Combustion research can be broadly classified into two categories: simple fluid mechanics, but complex kinetics, including real fuels such as blends of large hydrocarbons; or, the reverse, complex fluid mechanics, but simple chemical kinetics. Fundamental studies on both categories are necessary before starting to face the greater challenge of complex fluid mechanics and complex chemical kinetics [1].

This thesis is organized into three parts (Parts I-III) focusing, respectively, on jet fuel combustion, biogas combustion, and solid fuel combustion in microgravity conditions. It focuses mostly on diffusion flames and ranges from studies on complex chemistry with simple fluid mechanics (as in Part I) to problems involving complex patterns of heat and flow transfer modeled with a simple underlying chemistry (as in Part III). In Parts I to III, a broad range of fuels are studied, which are, respectively, in liquid, gaseous, or solid state.

In Part I, combustion of jet fuel and jet fuel surrogates, which are blends of large molecular weight fuels with complex kinetics, is experimentally studied. The objective is to study the structure of jet fuel doped diffusion flames at the onset of soot formation. In Part II, a combustion and chemical kinetic modeling is performed for biogas, which is produced from anaerobic digestion of biodegradable materials and is presently a viable alternative fuel (e.g., for gas turbines). Finally, in Part III, flame-surface interactions and combustion of solid fuels in simulated microgravity conditions are numerically and analytically investigated. Thin biomass samples (e.g., thin cellulosic fuels) are the principal solid fuels used.

The dissertation is organized so that this short introduction is followed consecutively by Parts I to III. Each part starts with a chapter in which a review of previous work, the motivation of research, and an introduction to the methodology of research conduct are all thoroughly presented. The second and third chapters of each part define the metrics of the problem after which results are presented and discussed. Conclusions in Chapter 11 include all concluding remarks as well as recommendations for future work pertaining to Parts I to III. Chapter 11 is followed by appendices. References for all parts are listed in 0.

Research in Part I, was conducted at Yale Center for Combustion Studies under the Air Force Office of Scientific Research (AFOSR) jet fuel surrogate program. A background of the research on jet fuel and its surrogates is presented in Chapter 2. In Chapter 3, the experimental procedure followed for the detailed chemical analysis of simple or complex fuels is explained. In Chapter 4, a well-defined baseline ethylene diffusion flame under incipiently sooting conditions is perturbed with the addition of either jet fuel or two jet fuel surrogates. Attempts are made to validate the surrogate formulations with respect to the flame structure and to provide an experimental database for the pyrolysis and oxidation behavior of jet fuel at the onset of sooting in diffusion flames.

Research in Part II on biogas combustion is motivated by the worldwide interest in alternative fuels, especially for stationary power generation. Particularly, it is of interest to the U.S. Departments of Energy and Agriculture as well as many State Governments.

In Chapter 5, the latest progress and challenges in biogas research are discussed. Also, biogas benefits, production methods and compositions are explained. In Chapter 6, a chemical kinetics study is performed for simulated biogas blends in premixed flames. First, a laminar counterflow diffusion flame configuration is chosen to evaluate some detailed and reduced mechanisms in regard to their applicability for the biogas chemical kinetics study. Gas phase equilibrium calculations are then performed, followed by ignition delay time and laminar flame speed calculations. In Chapter 7, thermal and chemical structure of biogas counterflow diffusion flames is examined. A detailed kinetic modeling of CO_2 diluted methane blends, which are typical biogas blends, is conducted. In addition, thermal and chemical influences of CO_2 content of biogas on flame temperature and emissions of NOx, soot and green house gases are evaluated.

Microgravity flame spread over solid fuels, investigated in Part III, is conducted in collaboration with NASA Glenn Research Center under the NASA microgravity program. Chapter 8 explains the motivation to investigate diffusion flames near solid fuel surfaces in either an "open" or a "confined" environment. In Chapter 9, an analytical and numerical model of surface-attached solid fuel flames with weak convection is constructed. The ultimate purpose of this study is to establish a model to examine flame structure, heat transfer, and reaction rate in flames attached to solid fuel surfaces, particularly surfaces in which multiple flames (or flamelets) may exist. In Chapter 10, flame and flamelet spread over thin solid fuels in simulated microgravity conditions is studied. Numerical analyses are compared with two sets of experiments involving flame spread in a Narrow Channel Apparatus (NCA, available at MSU and NASA) in normal gravity, and the others taking place in actual microgravity in the NASA drop facilities.

Part I

Experimental Study of Jet Fuel Combustion

Chapter 2 Background and Introduction to Jet Fuel and Jet Fuel Surrogate Combustion

Transportation fuels, including jet fuels, constitute a significant share of the world's energy consumption. Common jet fuels include Jet A-1, Jet A, and JP-8. They comprise hundreds of aromatic compounds and aliphatic components, such as straight chain paraffins, branched chain paraffins, cycloparaffins, and alkenes [2]. The increasing need for energy security as well as imposing stringent emission regulations for NOx, CO, particulates, and green house gases such as CO_2 necessitates: 1) Improved chemical modeling of conventional aviation fuels such as JP-8; 2) Development and commercialization of alternative transportation fuels like Fischer-Tropsch (F-T) jet fuels. Depending on the source of the parent crude and the refinery process, the jet fuel composition may vary significantly. The future fuel supply will become more and more diversified and burning a broad range of fuels as well as reduction of pollutant (e.g. soot) formation will pose new challenges to the implementation of their combustion. This trend will necessitate fundamental studies in well-defined and well-controlled environments to establish, among other aspects, the chemical kinetic behavior of these complex fuel blends.

Characterization and simulation of jet fuel chemical kinetics and transport is only practical by identifying surrogate mixtures having a relatively small number of components. The surrogate physical and chemical properties should capture essential features of real fuels in prototypical combustion conditions. The chemical community selects and characterizes surrogate fuel formulations. Normal paraffins, iso-paraffins, cyclo-paraffins, olefinic species, single ring aromatics, and multi-ring aromatics are typical constituents for a surrogate mixture. Colket et al. [3] proposed a road map for future development of surrogate fuels, which resulted from discussions at a number of meetings of a surrogate fuel working group. Developed surrogate formulations would need experimental validation with respect to the real jet fuels. Surrogate mixtures have been defined and tested in many experimental conditions and configurations, including flow/stirred reactors, shock tubes, premixed flames, pool fires, and counterflow diffusion flames. A comprehensive review was presented by Dagaut et al. [4]. Parallel attempts are made to compile semi-detailed kinetic mechanisms for a suggested surrogate. Each kinetic modeling should also be validated with experimental data of both the surrogate and the real jet fuel. Once the surrogate formulation and the semi-detailed kinetic mechanism are validated, the next step will be a systematic reduction of the surrogate kinetic mechanism. Reduced mechanisms can potentially be utilized in CFD codes with a significantly lower computational cost.

2.1. Jet fuel surrogates

In the late 1980's, Wood et al. [5] formulated a 14-component JP-4 surrogate based on its compound class composition and distillation curves. Subsequent efforts by Schulz et al. [6] led to a 12-component jet fuel surrogate. Feasibility, simplicity, fuel class similarity, and cost are essential criteria that guided subsequent work aimed at decreasing the number of components to produce more manageable formulations. Violi et al. [7] reported a six-component Utah surrogate designed to match the volatility of jet fuel and its overall sooting behavior based on smoke point tests. Five-component surrogates e.g. the Drexel surrogate [8] or the Utah/Violi Surrogate #3 [7], four-component surrogates e.g. the surrogate in [9], and three-component surrogates e.g. the UC San Diego/Milan surrogate [10] have also been reported. More recently, the number of components has further decreased with the minimization effort culminating in the two-component Aachen surrogate [11]. Single-component surrogates, though initially contemplated, are now generally thought to lack the necessary flexibility to match the jet fuel performance in a sufficiently broad parameter space. In recent work in pressurized flow reactors, Natelson et al. [12] experimentally studied jet fuel and a three-component jet fuel surrogate suggested by the surrogate fuels working group at pressures as high as 0.8 MPa. The three-component surrogate showed higher reactivity than jet fuel suggesting that an improvement is possible by adding iso-paraffins. Experiments by Holley et al. [13] in a counterflow non-premixed configuration found that the six-component Utah surrogate [7] increased ignition propensity and resistance to extinction compared to jet fuel. This behavior was attributed to mismatched transport properties. Vasu et al. [14] measured ignition delay times of jet fuels in a shock tube and compared them with predictions of some current kinetic mechanisms [15, 16]. The five-component Utah surrogate (Violi Surrogate #3 [7]), when used with the Milan mechanism [15], revealed the closest agreement in ignition delay times, especially in capturing the high-temperature trend. This work has continued on individual components of the surrogate mixture, *n*-dodecane ($n\text{-}C_{12}H_{26}$) and methylcyclohexane (MCH), with shock-tube experiments on the former [17] and with measurements of OH time-histories of oxidation behind reflected shocks for the latter [18].

2.2. Surrogates for alternative jet fuels

Alternative jet fuels can be derived from shale, coal, biomass, or natural gas. Fischer-Tropsch (F-T) jet fuels are derived from synthesis gas ($CO+H_2$) made from natural gas using the Fischer-Tropsch process [19]. These fuels can significantly reduce particulate matter (PM) emissions. The complex F-T jet fuels are drawing more and more interest worldwide and in the U.S. The U.S. Department of Defense and the Department of Energy are jointly working through programs such as the Clean Fuels Initiative to develop F-T jet fuels and to assess their national security benefits and weigh them against cost and availability concerns [20].

JP-8 mixed with synthetic jet fuels (synjet) makes an aviation fuel blend e.g. F-T Jet A-1 (S-8). Since the F-T jet fuels consist mainly of paraffins [21], which in case of S-8 are alkanes with one or two attached methyl groups [22], a surrogate for these fuels should likely include *iso*-paraffin as a major component. The reason for this extent of isomerization is to meet the jet fuel density and freeze point specifications [19]. Recently, Natelson et al. [23] experimentally studied the pre-ignition and autoignition behavior of the F-T jet fuels and possible surrogates to understand the influences of compositional differences on the chemistry of pre-ignition and autoignition. Kahandawala et al. [24] investigated JP-8, an F-T synthetic jet fuel, and a one-component surrogate synjet fuel (2-methylheptane) in a shock tube and showed that both surrogate and actual synjet, and JP-8 fuels had similar ignition delays. Mawid [25] suggested a two-component S-8 F-T surrogate, which showed a similar ignition behavior to a JP-8 surrogate.

2.3. Kinetic modeling of jet fuel surrogates

Jet fuel surrogate mechanisms consist of hundreds of species and thousands of reactions (e.g. Complete Ranzi mechanism: 310 species and 8335 reactions; Zhang mechanism: 208 species and 1087 reactions [16]; Mawid mechanism: 226 species and 3230 reactions [26]). These kinetic mechanisms for various surrogate blends have been computationally modeled in both premixed and non-premixed configurations.

Ignition delay times and laminar burning velocities of jet fuel surrogates have been calculated using FlameMaster [27] or CHEMKIN [28] codes. Honnet et al. [11] modeled a 2-component JP-8 surrogate (the Aachen surrogate) with FlameMaster. Vasu et al. [14] used CHEMKIN to find ignition delay times of 5- and 6- component jet fuel surrogates (Violi surrogates [7]). Dagaut et al. [29] used PREMIX [30] and PSR [31] CHEMKIN-based codes to model their 3-component jet fuel surrogate.

Counterflow diffusion flame codes such as OPPDIF [32] and FlameMaster [27] are well established and are widely used to study jet fuel surrogates [10, 11, 33, 34]. Highly optimized libraries and optically thin radiation models have been employed to evaluate the thermodynamic and transport properties, the chemistry, and the radiative flux [33]. When large chemical mechanisms are to be modeled, many modifications are necessary to the original codes. Many combustion mixtures of our interest include large jet fuel hydrocarbons or their surrogate components. These contain molecules of disparate molecular weight. Also, in the case of sooting flames, multi-ring PAH's can form heavy reaction intermediates. Relevant transport mechanisms and coefficients would be affected by such a "molecular weight contrast" [35]. All diffusivities (ν, α, D) in the computer code should be revisited to accommodate for such phenomena. For example, the code modified by the Smooke group at Yale [36] incorporated a modification of Fickian transport models and an inclusion of the Ludwig-Soret effect for heavy molecules.

To my knowledge, modeling the sooting or incipiently sooting surrogate-doped ethylene flames with the well-tested mechanisms like the Ranzi mechanism is yet to agree with experiments [37]. Also, the detailed chemical structure of counterflow diffusion flames has not been studied with simple jet fuel surrogates such as the Aachen surrogate.

2.4. Reduction of surrogate mechanisms

Several leading research groups are working on compilation and reduction of jet fuel reaction mechanisms. Among all reaction mechanisms studied by the Hanson group [14], the Ranzi mechanism [15] showed the closest agreement with the experimental ignition delay data. This kinetic mechanism is an example of successful mechanism compilation. It was compiled using existing hierarchically-constructed models for alkanes (*n*-dodecane, *iso*-octane, and *n*-tetradecane) and simple aromatics extended to account for the presence of tetralin and methylcyclohexane [33]. The Smooke group at Yale has used this mechanism in the non-sooting counterflow diffusion flames [36] and is attempting to reduce it.

Recently, a comprehensive discussion on the development of reduced mechanisms was presented by Lu et al. [38]. Various skeletal reduction methodologies have been employed to remove unimportant species and reactions from a detailed mechanism: directed relation graphs (DRG), DRG with error propagation (DRGEP), DRG-aided sensitivity analysis (DRGASA), computational singular perturbations (CSP), optimization, principal component analysis, detailed reduction, Jacobian analysis, and sensitivity analysis [38, 39]. One of the fastest skeletal reduction algorithms is DRG [40, 41], which have been recently used by Lu and Law for the reduction of *n*-heptane [39, 40] and *iso*-octane [40], and by Pepiot-Desjardins and Pitsch [42] for *iso*-octane (using DRG-based techniques). The skeletal reduction is followed by lumping and time-scale analysis. A novel lumping method was recently suggested by Pepiot-Desjardins and Pitsch [43] and used for *n*-heptane and *iso*-octane. Time-scale analysis methods may include QSSA, PEA, ILDM, and CSP [38].

2.5. Gas Chromatography and Mass Spectrometry (GC/MS)

Flame sampling involving the physical extraction of gaseous samples by a probe for subsequent chemical analysis provides a wealth of data about the underlying flame chemistry. Flame sampling is virtually indispensable for a detailed chemical kinetics study of high molecular weight hydrocarbons such as jet fuel or its surrogates. A GC/MS is used in this work for the chemical analysis. The GC/MS instrument is a complex piece of equipment composed of various parts; the operation of these parts allows achieving separation and identification/quantification of different species in a gas mixture [44].

The term gas chromatograph is often used to generically refer to the group of components (e.g., oven, chromatographic columns, etc.) operating to achieve species separation. The GC operates on gas mixtures, although analysis of liquid samples can also be performed by introducing the sample through appropriate injectors, after which the liquid is vaporized. Chromatographic separation of selected species in the gas mixture takes place within chromatographic columns. Identification and quantification of species as they emerge from the columns is performed by means of dedicated detectors. The time, under a given and fixed set of conditions, that each component of the sample is retained in the chromatographic column is called the retention time. The different species can be identified based on their retention time that is typically determined on the basis of the columns standard chromatograms. The separation of the mixture is recorded as a series of peaks. The area under each of these peaks is uniquely proportional to the concentration of that component in the original mixture. Integration of the area can be used for quantification provided that accurate calibration curves are available for the component.

The Mass Spectrometer (MS) allows for both identification and quantification of species. Because of its operational principle, the MS does not always require species separation. Other detectors (e.g. Flame Ionization Detector (FID) and Thermal Conductivity Detector (TCD)) are generally only used to quantify absolute or relative amounts of separated compounds. A software (Agilent Chemstation) is used to run analyses and analyze the data extracted from the GC/MS.

2.6. Experimental study of jet fuel combustion

In an earlier study at Yale [33], good agreement was reported for extinction strain rate and temperature profiles between jet fuel and a six-component surrogate in *non-sooting* counterflow diffusion flames. This contribution began in collaboration with the research groups at University of Utah and University of Milan, with the Utah group establishing the surrogate mixture formulation and the Milan group developing the chemical kinetic model for this surrogate including 221 species and 5032 reactions [33]. The formulation used in [33] and in all subsequent work at Yale departs slightly from the Utah surrogate in that the %vol composition of the six components (Surrogate #1) in

Violi et al. [7] was reinterpreted as molar fractions, which resulted in relative average changes of 27% in the component molar compositions. We shall refer to this surrogate as the Utah/Yale surrogate. More detailed investigations followed in the Yale laboratory, with the chemical analysis of the structure of a methane counterflow diffusion flame perturbed with thousands of ppm of either jet fuel or the six-component jet fuel surrogate [34, 45] in highly diluted and *non-sooting* flames, including detailed one-dimensional modeling using the Milan mechanism. The surrogate captured the general jet fuel behavior reasonably well except for ethylene and small aromatics such as benzene and toluene. The discrepancy in aromatics is cause for concern, if confirmed under sooting conditions, since aromatics are critical precursors to soot.

The sooting behavior of jet fuels, especially at take-off, is an issue in most aero-turbines for which non-premixed configurations are preferred. Therefore, any surrogate formulation needs to be validated with respect to this performance. Beyond global combustion properties, such as extinction, ignition, and flame speed of jet fuels, detailed probing ensures validation of surrogate composition in sooting conditions and also provides details on the structure of jet fuel sooting flames [46]. Gas sampling is problematic in the presence of large amounts of soot because of the inevitable clogging of the microprobe orifice. This problem can be circumvented if conditions of *incipient sooting* are chosen, in which the soot loading is kept at the minimum necessary to discern a faint blackbody luminosity in the flame. These are the conditions chosen in the present study.

A comprehensive investigation is conducted on the detailed flame structure of ethylene counterflow diffusion flames perturbed by trace amounts (2000 ppm, molar) of jet fuel and two surrogates via gas sampling and chemical analysis. The ultimate goal is to ascertain if the surrogate formulations are reasonably successful in mimicking the performance of jet fuel, especially with respect to the behavior of small aromatics for which discrepancies were observed under non-sooting conditions [36, 46]. In addition to attempting to validate the surrogate formulations with respect to the flame structure, the objective is also to provide a database for the pyrolysis and oxidation behavior of jet fuel in a diffusion flame at the onset of soot formation for other investigators to use in parallel research efforts. Two surrogates are examined: the six component Utah/Yale surrogate used in all previous work in the Yale laboratory [33, 34, 45], and a two component Aachen surrogate, that has been reported to mimic not only conditions of extinction and autoignition, but also to match the soot volume fraction behavior, especially under relatively high strain rates [11]. Semi-detailed chemical kinetic mechanisms are available for both surrogates [11, 47, 48]. The study of the Aachen surrogate is conducted in collaboration with the research groups at University of California San Diego and RWTH Aachen.

Chapter 3 Experimental Procedure for Detailed Chemical Analysis of Jet Fuel Doped Flames

In this chapter, details of the experimental procedure for the chemical analysis of jet fuel and its surrogates are explained. The experimental work included in this thesis was performed at the Yale Center for Combustion Studies at Yale University. The work presented in this thesis is the latest progress made in the experimental part of the jet fuel combustion research (started few years ago and supported by the AFOSR and ARO) at the Yale Center. The details of the experimental setup which includes a counterflow burner equipped with a semi-automated GC/MS are presented. Criterion for comparison of various ethylene diffusion flames either as baseline flames or flames doped with jet fuel and its surrogates are elaborated. The adjustments in boundary conditions are also discussed. Photographs of the experimental setup, used in this work, are presented in Appendix A.

3.1. Theory of counterlfow flames

Counterflow (opposed-flow) burner configurations have been extensively used in the study of *non-premixed* as well as *premixed* flames. The configuration has many desirable characteristics for experimental and computational studies. It is symmetric and the resulting flame is planer. Thus, detailed experimental and computational investigation of the flame structure can be conducted in the direction normal to it along the centerline. Both sides of the flow can be seeded with particles for LDV or PIV mapping of the flow field. A schematic of a counterflow diffusion flame, which can be generated by impinging a uniform oxidizer jet against a uniform fuel jet is shown in Figure 3-1. A photograph of a counterflow burner, used in this work, is presented in Appendix A.

In the counterflow configuration, buoyancy effect is small and the resulting flame is quite steady because the flow is usually dominated by forced convection [49]. In the laboratory, stability can be further facilitated by adding a guard flow (also called shroud flow) of inert gas and adjusting its flow velocity. This shroud flow also isolates the reactant jets from the environment. However, the shroud flow may have a drawback: it sometimes moves the flame. As a result, when computational profiles are to be compared with the experimental profiles a shift, which depends on the velocity of the shroud flow, may be indispensible to match profiles.

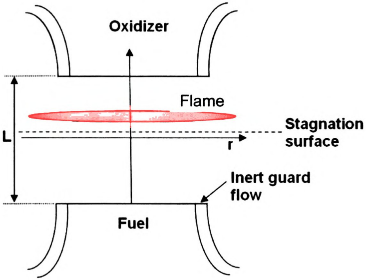

Figure 3-1. Schematic of a counterflow burner with a diffusion flame.

According to Law [49], "the inverse of the velocity gradient, 1/*a*, represents a characteristic flow time, which, when compared to the characteristic reaction time, yields the system Damkohler number". Because the flow velocity along the centerline near the stagnation region varies linearly with distance, the flow can be characterized by a single parameter, namely its velocity gradient *a*, which constitutes the local strain rate. In the laboratory, aerodynamically shaped nozzles usually generate uniform flows. The strain rate, *a*, can be approximated for the counterflow as [50]

$$a_O = \frac{V_O}{L}\left(1 + \frac{V_F\sqrt{\rho_F}}{V_O\sqrt{\rho_O}}\right), \tag{3-1}$$

$$a_F = \frac{V_F}{L}\left(1 + \frac{V_O\sqrt{\rho_O}}{V_F\sqrt{\rho_F}}\right), \tag{3-2}$$

where a, V and ρ are strain rate, velocity and density, respectively, subscripts O and F denote fuel and oxidizer and L is the distance between nozzles (or burner separation).

Seshadri and Williams [50] defined a density corrected strain rate, *a*, for the counterflow flame as

$$a = \frac{2V_O}{L}\left(1 + \frac{V_F\sqrt{\rho_F}}{V_O\sqrt{\rho_O}}\right), \tag{3-3}$$

where V_O and V_F are the flow velocities normal to the stagnation plane (SP) at the oxidizer and fuel boundaries, respectively, and ρ_O and ρ_F are the mixture densities at the oxidizer and fuel boundaries, respectively. Density corrected strain rates defined by Eq. (3-3) are used in this part.

The stoichiometric mixture fraction, z_f, is defined as

$$z_f = \frac{1}{1 + s Y_{FF} / Y_{OO}}, \qquad (3\text{-}4)$$

where s is the stoichiometric mass ratio of oxygen to fuel, Y_{FF} and Y_{OO} are the feed stream mass factions of the fuel (regardless of the chemical composition) and oxygen, respectively.

Highly turbulent counterflow flames have been recently proposed as a very useful benchmark of complexity intermediate between laminar flames and practical systems [1]. By operating in a turbulent Reynolds number regime of relevance to practical systems such as gas turbines and internal combustion engines, they retain the interaction of turbulence and chemistry of such environments, but offer several advantages from both a diagnostic and a computational viewpoint.

3.2. Experimental setup

Figure 3-2 shows a schematic of the experimental setup. It consists of a counter-flow burner [46], including a nitrogen shroud that shields the flame from room drafts and ensures burning in the controlled atmosphere that is determined by the composition of the feed streams. Carefully designed convergent sections allow for a top-hat velocity profile at each burner mouth. The inner diameter of the fuel and oxidizer outlets is 12.5 mm and the burner separation (*L*) is 14.1 mm. Slightly nitrogen-diluted air is used as the oxidizer while the fuel is nitrogen-diluted ethylene doped with either jet fuel or the surrogates. To ensure complete vaporization of the dopant liquid, an electrospray operated in the multi-jet mode [51] disperses the liquid fuel in the preheated fuel/nitrogen stream. This approach provides flexibility in flow rates without compromising the stability of the flame. To prevent condensation downstream of the electrospray unit, PID controllers keep the fuel line at 430K, which is well above the dew point of the dopant/C_2H_4/N_2 mixtures. Gas samples are extracted from the flame through a microprobe, consisting of a small silica probe with an outer diameter of 340 μm and an inner diameter of 170 μm. Details of the different microprobes used previously can be found in [34, 45].

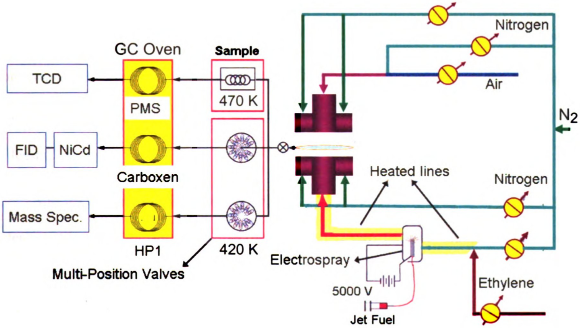

Figure 3-2. Schematic of the experimental setup.

The chemical analysis is performed by a gas chromatograph (Agilent 6890A) equipped with mass spectrometer (MSD, Agilent 5973N), thermal conductivity (TCD), and flame ionization (FID) detectors. The instrument is capable of quantifying complex hydrocarbon mixtures, CO, CO_2, O_2 and N_2. It uses two capillary columns, a Supelco Carboxen and an Agilent HP-1, connected to the FID and MSD, respectively. In addition, the TCD measures non-hydrocarbon stable gases separated by means of a third column (Alltech, Packed Molecular Sieve). Because of its much wider linear range, this detector is better suited than the MSD for the analysis of gases present as large fractions of the gas sample and/or in greatly varying amounts e.g. N_2 and O_2. A homemade nickel-based catalytic converter (Methanizer) allows for FID quantification of CO and CO_2 upon their conversion into methane in the presence of hydrogen. The system can separate and quantify H_2, N_2, O_2, CO, CO_2, light gaseous hydrocarbons and higher hydrocarbons up to at least C14.

Species are identified during the GC/MS data post-processing by both the column retention time and the molecule-specific mass spectrum. GC/MS analysis produces a wealth of information, but has one main drawback: it takes a very long time to perform a flame scan. At the small liquid flow rates of interest for jet fuel (e.g. 1.6 ml/hr), a syringe pump is used to deliver the fuel. Preserving a steady flame over the analysis time, which is on the order of one day, would be challenging: it would require repeated flame shut-offs for reloading of the syringes. Thermal transients would affect boundary conditions, and other inevitable consequences such as sampling probe distortions might cause reproducibility problems that affect the self-consistency of the data. To sidestep these problems, a semi-automated chemical analysis method is employed that consists of sampling the gas and storing it in a battery of sampling loops using two pneumatic-actuated injection valves and two multiposition valves, as shown in Figure 3-2 [12, 34, 45, 52, 53]. One of the pneumatic injection valves is responsible for the TCD analysis (top left in the figure) that is executed in real time, since it requires about two minutes per data point. The other valve controls the FID and the MS. Since these two instruments require a much longer time to complete a measurement, the samples are stored in two sets of 16 sample loops using two multi-position valves (Valco®) and analyzed overnight by a computer-automated sequence. An optimized time-temperature program for the chromatographic columns keeps the total analysis time at a minimum and ensures that aging of samples does not change the sample concentrations significantly.

Temperature measurements are performed using flame-welded, silica coated Pt-10%Rh/Pt thermocouples with a typical junction diameter and a wire diameter measuring on the order of 70 μm and 50 μm, respectively. Standard corrections for radiative losses are applied. In some temperature measurements, a gas sample probe is also placed within the flame to assess the probe's intrusiveness. As a result, any spatial offset between temperature profiles with and without the probe would be mostly due to the sampling probe intrusiveness. Temperatures of both feed streams at the burner outlets are measured by a K-type thermocouple.

Accuracy in the GC/MS analysis and reproducibility of the data were ensured by analyzing gas mixtures of known composition (Scotty®) and repeated sampling at the same position in the flame. Standard calibration gases (Scotty®) are used for calibration of light gaseous species. Aliquots of liquid hydrocarbons dissolved in acetone are injected into the GC/MS for the calibration of heavy liquid hydrocarbons. The total error is estimated at 7% for light species and 12% to 15% for the heavier ones.

3.2.1. The electrospray

It was mentioned earlier that an electrospray operated in the multi-jet mode disperses the liquid fuel in the preheated fuel/nitrogen stream. Figure 3-3 shows a schematic and photograph of the electrospray unit. For small flow rates (up to 10 mL/h), a tapered needle is used to disperse fuel. The ground electrode consists of a ring positioned 2 cm downstream the tip of the needle. A voltage between 4 and 6 kV is applied between the two electrodes. The spray is often run in the multi-jet mode, depending on the flow rate and voltage. To monitor the electrospray behavior and ensure that the liquid is well-dispersed into vapor without condensation, a transparent Pyrex electrospray chamber (evaporator) is used. This electrospray chamber is heated by

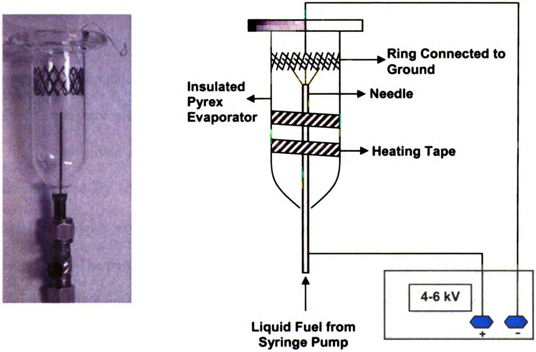

Figure 3-3. Schematic and photograph of the electrospray unit for liquid fuel dispersion.

heating tapes covered by an insulation layer. A thermocouple is positioned inside the chamber, very close to its wall, to monitor its temperature that is kept at around 160 °C to avoid condensation. The electrospray must be operated with particular attention. Two copper tubes (not shown in the Figure), painted in black to avoid glare, are mounted perpendicularly to the Pyrex evaporator to realize small "openings" in the insulation layer and enable occasional visualization of the spray behavior using a microscope. Sparks may cause misbehavior of the spray. They may also damage the temperature PID controllers that, at the very least, will require resetting. Beside the visualization of the electrospray with microscope from the black opening, current can be checked. The current through the voltage amplifier should be zero since no shortcut is desired while a steady multi-jet spray is present.

3.3. Criterion for flame comparison

Diffusion flames "doped" with trace amounts of prevaporized liquid fuel have shown many computational and experimental advantages. The advantages of doping a baseline flame were mentioned in the previous studies at Yale [34, 45]. This approach was first employed in non-premixed flames by Hamins et al. [54] and has been more extensively used by McEnally and Pfefferle [55, 56]. This approach minimizes the potential for vapor condensation* since the condensable species is at very small concentrations. The temperature-time history can be easily adjusted to be identical for all flames, so that this counterflow flame environment can be regarded as a flow reactor in which the residence time and the temperature profile are adjusted by varying the strain

---

* Evidence in preliminary experiments at Yale had showed that, probably because of condensation effects in the unheated probe, the species with largest molecular weights were underestimated.

rate and the feed stream composition, respectively. The temporal history is identical since the flames have essentially the same mass averaged velocities at the boundaries and identical temperature profiles, which leads to the same evolution of the velocity profile via gas expansion. Furthermore, critical, non-chemical variables, such as temperature and velocity, as well as probe-induced perturbations, can be evaluated once and for all in the baseline flame.

The counterflow configuration is chosen, as in previous studies at Yale, as the work horse for a systematic study of fuels with complex chemical kinetics and their coupling with transport in the simplest possible fluid dynamic environment: a one-dimensional laminar flow. It is amenable to detailed computational models that are now routinely applied in most combustion laboratories, at least for simple fuels. Since our goal is to focus on conditions yielding soot formation and since soot is an issue primarily in non-premixed flame environments [56], a non-premixed counterflow flame is appropriate for our study. For such a flame, the density corrected strain rate, a, was defined by Eq. (3-3) and the stoichiometric mixture fraction, z_f, was defined by Eq. (3-4).

The previous study at Yale [36] focused on a highly diluted *methane* baseline flame doped with 1000 ppm of jet fuel or the Utah/Yale surrogate under *non-sooting* conditions, with $T_{max} \approx 2012$ K, $a = 144$ s^{-1}, and $z_f = 0.76$. For comparison purposes, the boundary conditions for these non-sooting methane flames studied by Bufferand et al. [36] are presented in Table 3-1. Here we use an *ethylene* baseline flame, since C_2H_4 has a greater soot propensity than CH_4, so that its boundary conditions can be adjusted with ease for it to be at the onset of soot formation. To that end, the temperature/time history needs to

Table 3-1. Boundary conditions for the *non-sooting methane* flames doped with jet fuel and Utah/Yale surrogate from the previous study of Bufferand et al. [36] at Yale.

		Flame A Baseline	Flame B Jet Fuel	Flame C Utah/Yale Surrogate
Fuel Side	Molar Composition			
	N_2	0.897	0.902	0.902
	CH_4	0.103	0.097	0.097
	C2-C5 alkane impurities	232 ppm	218 ppm	218 ppm
	Jet fuel ($C_{11}H_{21}$)		992 ppm	
	Methyl-Cyclohexane			200 ppm
	Iso-Octane			100 ppm
	m-Xylene			150 ppm
	Tetraline			50 ppm
	Dodecane			300 ppm
	Tetradecane			200 ppm
	Mass Flux (g/(cm^2.min))	2.80	2.97	2.97
	Temperature (K)	379		
Oxidizer Side	Molar Composition			
	N_2	0.227		
	O_2	0.773		
	Mass Flux (g/(cm^2.min))	3.19	3.42	3.42
	Temperature (K)	340		
	Strain Rate (s^{-1})	134	144	144
	z_f	0.76		

favor soot formation, with higher temperatures and lower residence times [57-59], and the stoichiometric mixture fraction, z_f, would have to decrease sharply in comparison with our previous studies to values less than 0.5 to ensure that the flame locates itself on the *oxidizer* side of the stagnation plane and oxidation of soot precursors is avoided [60]. A value of $z_f = 0.18$ was chosen for all flames. The stoichiometric mass ratio of oxidizer to fuel, s, for the baseline flame is 3.42, whereas Y_{FF} and Y_{OO} are 0.27 and 0.2, respectively.

Table 3-2 specifies the overall mean strain rate and the boundary conditions (mole fractions, total mass flux and outlet temperatures of both fuel and oxidizer streams) for the five flames under consideration: the baseline ethylene flame, Flame A; the ethylene+jet fuel flame, Flame B, the ethylene+Utah/Yale surrogate flame, Flame C; the ethylene+Aachen surrogate flame, Flame D; and a fifth flame, Flame A*. The latter is a modified baseline ethylene flame whose total fuel carbon flux matches the doped flames. The total carbon flow rate is 3.81×10^{-2} mol/min and 3.96×10^{-2} mol/min for Flame A and Flame C, respectively. Flame A* is established by modifying the boundary conditions of Flame A to ensure the same z_f, temperature profile, and carbon molar flow rate as Flame C. To avoid clutter, the only data that will be presented for Flame A* is the concentrations of a few minor species such as aromatics. A chemical formula of $C_{11}H_{21}$ and density of 0.81 gr/cm^3 were used for jet fuel [61]. The jet fuel was provided by Wright-Patterson Air Force Base (POSF No. 4658). To account for the considerable variability in the composition of jet fuel from different refineries, an "average" jet fuel was synthesized by mixing together 5 Jet A fuels from different U.S. manufacturers. The composition of that blend in vol% is: 55.2% paraffins (n- and i-), 17.2% monocycloparaffins, 12.7% alkyl benzenes, 7.8% dicycloparaffins and 4.9% indans and Tetralin. The balance, ≈ 2%, is in naphthalenes and trycylcoparaffins.

Table 3-2. Boundary conditions for the *ethylene diffusion flames* under incipiently sooting conditions. The jet fuel was provided by WPAFB (POSF No. 4658).

		Flame A Baseline	**Flame A*** Equal Carbon	**Flame B** Jet Fuel	**Flame C** Utah/Yale Surrogate	**Flame D** Aachen Surrogate
Fuel Side	Molar Composition					
	N_2	0.7278	0.7280	0.7340	0.7339	0.7339
	C_2H_4	0.2722	0.2719	0.2641	0.2641	0.2641
	C2 (Ethane) impurities	637 ppm	636 ppm	618 ppm	618 ppm	618 ppm
	Jet Fuel ($C_{11}H_{21}$)			1953 ppm		
	Methyl-cyclohexane				394 ppm	
	Iso-Octane				197 ppm	
	m-Xylene				295 ppm	
	Tetralin				98 ppm	
	n-Dodecane				591 ppm	
	n-Tetradecane				394 ppm	
	Total=				1970 ppm	
	1,2,4-trimethylbenzene					450 ppm
	n-Decane					1520 ppm
	Total=					1970 ppm
	Mass Flux (g/(cm^2.min))	1.619	1.683	1.684	1.683	1.682
	Temperature (K)	407	407	407	407	407
Oxidizer side	Molar Composition					
	N_2	0.8070	0.8070	0.8070	0.8070	0.8070
	O_2	0.1843	0.1843	0.1843	0.1843	0.1843
	Mass Flux (g/(cm^2.min))	1.891	1.925	1.925	1.925	1.925
	Temperature (K)	370	370	370	370	370
	Strain Rate (s^{-1})	89.9	85.2	92.3	92.3	92.3
	z_f	0.18	0.18	0.18	0.18	0.18
	Carbon mole fraction %	54.45	54.39	54.97	54.85	54.74
	Carbon flow rate (mol/min × 10^{-2})	3.81	3.958	3.967	3.958	3.951
	V_O (cm/s)	33.17	31.03	33.77	33.77	33.77
	V_F (cm/s)	32.17	31.13	33.16	33.16	33.16

Table 3-3. Jet fuel surrogate mixtures; values are reported in molar %.

	Utah/Yale Surrogate	Aachen Surrogate
iso-octane	10	
methylcyclohexane (MCH)	20	
m-xylene	15	
n-dodecane	30	
n-tetradecane	20	
tetralin	5	
1,2,4-trimethylbenzene (TMB)		22.8
n-decane		77.2

The Utah/Yale surrogate is the six-component blend of well-known hydrocarbons used in the previous works at Yale [33, 45], while the Aachen surrogate is a two-component surrogate as used in [11]. Compositions of these surrogates are given in Table 3-3. The surrogate components are made by mixing high purity hydrocarbons (Sigma-Aldrich and Fluka $\geq$ 99% purity). Trace amounts of an ethane impurity in the C_2H_4 supply were revealed by chromatographic analysis at about 620 ppm. The ethane impurity of each flame has been listed in Table 3-2.

A photograph of Flame C, the baseline flame doped with the Utah/Yale surrogate, is shown in Figure 3-4. A layer of orange luminosity is visible underneath the flame chemiluminescence. The dopant concentration is chosen based on two considerations: (1) it should be sufficiently small so as not to change the overall flame structure and to preserve incipient sooting conditions, such that clogging of the microprobe orifice is avoided without resorting to special probes with attendant deterioration of the spatial resolution [62]; and (2) it should be sufficiently large so that the jet fuel/surrogate contribution to the production of critical species, such as soot precursors (e.g., small aromatics) can be discriminated from the contribution of the baseline flame. On the basis of these considerations, the ethylene flame was doped with 2000 ppm of either jet fuel or its surrogates. However, the addition of even such a small amount of these fuels increases the peak temperature by 20-30 K and the flame location shifts slightly toward the oxidizer side. To preserve the temperature-time history and ensure comparable Arrhenius kinetics among all of the flames, the temperature profile needs to be the same in all of them. Also, since the mixture fraction is a single-valued complementary error function of the axial position, fixing its value at $z_f = 0.18$ ensures that the flame position is unaltered by the perturbation. To maintain the same temperature profiles as in the baseline flame, we increased the inert mole fraction in the fuel stream, which leads to a small change in z_f and a further shift of the flame towards the oxidizer side. We compensated for this shift by a small increase in the oxidizer flow rate to move the stagnation flame in the opposite direction, towards the fuel side.

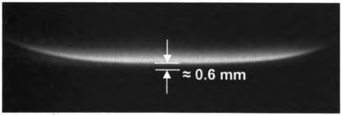

Figure 3-4. Photograph of the flame at the onset of sooting. The thickness of the sooting zone with orange luminosity underneath the blue zone is about 0.6 mm.

Chapter 4 Experimental Study of Ethylene Counterflow Diffusion Flames Doped with Jet Fuel and its Surrogates under Incipiently Sooting Conditions

In this chapter, results of the chemical analysis of jet fuel and its surrogates are presented. An ethylene counterflow diffusion flame doped with 2000 ppm on a molar basis of jet fuel, Utah/Yale surrogate or Aachen surrogate is studied under *incipiently sooting* conditions. As discussed earlier, the doped flames have identical stoichiometric mixture fractions and strain rates, resulting in a well-defined and fixed temperature/time history for all of the flames. Five flames are under consideration: the baseline ethylene flame, Flame A; the ethylene+jet fuel flame, Flame B, the ethylene+Utah/Yale surrogate flame, Flame C; the ethylene+Aachen surrogate flame, Flame D; and a fifth flame, Flame A*, which is a modified baseline ethylene flame whose total fuel carbon flux matches the Utah/Yale surrogate doped flame. Profiles of temperature, critical fuel decomposition products, and soot precursors are compared. These profiles include major species, C7-C15 alkanes and alkenes, C3-C6 alkanes and alkenes, C2 hydrocarbons, and some aromatic species. By comparing and contrasting the detailed structure of these flames, the surrogates' pyrolysis, oxidation, and most importantly the sooting behavior are examined.

4.1. Similarities in Temperature and Species Profiles among Flames

Figure 4-1 presents a comparison between the temperature profiles of Flame A (baseline), Flame C (doped with the Utah/Yale surrogate), and Flame A* (baseline with the same carbon mole flux as Flame C). Note that the temperature profiles are indistinguishable among the three flames, which means that our strategy of establishing virtually identical time-temperature histories is successful. Since the overall jet fuel heat release behavior was indirectly validated with the Utah/Yale surrogate in [33] and with the Aachen surrogate in [11] by examining the extinction behavior and the temperature profiles of such flames, the same concentration of jet fuel and of the Aachen surrogate should lead to identical temperature histories.

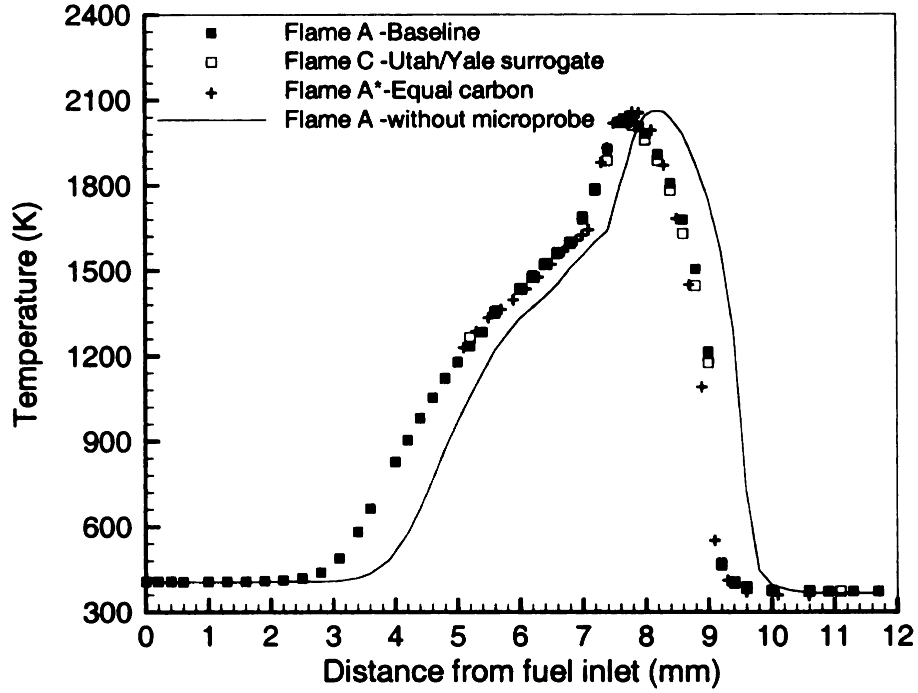

Figure 4-1. Temperature profiles. Symbols: Flames A, C and A* with microprobe in. Line: Flame A in the absence of microprobe.

The intrusiveness of any physical probe inserted into the flame is a common criticism raised to probe sampling. In addition to introducing a heat sink into the combustion environments, the probe may perturb the fluid dynamics of the flame [36]. McEnally et al. [55, 56] have comprehensively reviewed such pitfalls of flame sampling. *In situ* analysis, primarily by optical techniques, has the advantage of being essentially nonobstructive. However, it is usually less general, often applying to at most only a few of the species present in the flame [63]. To assess the probe perturbations, an additional temperature profile is shown for the baseline flame in the absence of the sampling microprobe. Comparison between the temperature profiles confirms an overall probe-induced perturbation that results in a 0.5 mm shift towards the fuel side, consistent with similar conclusions from OH planar laser induced fluorescence [36]. This shift accounts for roughly 7 % of the physical domain where chemistry is playing a role (the region between 2 and 9 mm from the fuel inlet), is therefore considered a modest shift.

Figure 4-2 compares some major species profiles among Flames A to D. Unless specifically noted in the subsequent figures, no experimental data of Flame A* are shown to avoid excessive cluttering of figures. Full-blue symbols are used for the baseline ethylene flame (Flame A), full-black symbols for the jet fuel doped flame (Flame B), open symbols for the Utah/Yale surrogate counterpart (Flame C), full-red symbols for the Aachen surrogate counterpart (Flame D), and + for the modified baseline flame (Flame A*) in this and all subsequent figures. Our goal was to perturb a well-defined baseline ethylene flame with the addition of trace amounts of jet fuel or surrogates. No distinction is observed in the profiles of the five flames with respect to CO and CO_2. O_2 was only measured in Flame A and is shown in the figure to illustrate the overall nonpremixed flame structure. The profiles of C_2H_4 are also identical, except at the fuel side boundary where the mole fraction has necessarily changed between the baseline flames (Flames A and A*) and the doped flames (Flames B, C, and D) because of the flow rate adjustments discussed in Section 3.3. As elaborated before, the temperature profiles (Fig. 3) of these flames are virtually the same. The absence of significant changes in the concentrations of CO and CO_2 and of temperature because of the presence of either jet fuel or the surrogates indicates that these species and the heat release are produced predominantly by the oxidation of C_2H_4. The blue flame in Figure 3-4 locates itself at approximately z=6.2-6.4 mm. The thickness of the orange sooting zone is about 0.6 mm. The asymmetry in the temperature profile is due to endothermic pyrolysis reactions between z = 5 and 7 mm. Detailed modeling of ethylene nonpremixed flames confirms the existence of such a zone [64]. The maximum CO_2 mole fraction is slightly larger than that of the methane non-sooting flames in our previous experiments [36], whereas the peak of CO mole fraction is nearly 1.5 times larger than that of the non-sooting flames. This difference is attributable to the nitrogen mole fraction in the fuel stream being smaller in the ethylene flames.

A drawback with probing of non-premixed flames in general is that the layer where interesting products are abundant is narrow and comparable to the spatial resolution of regular probes. The CO profiles of our sooting flames are wider than in [36]. One of the reasons for this behavior is that the strain rate of these flames is smaller than the strain rate of the non-sooting flames (the flame thickness scales inversely with $\sqrt{a}$). Having a wider region where chemical reactions are occurring makes the probing easier and more reliable, especially since we want to track the formation of aromatics.

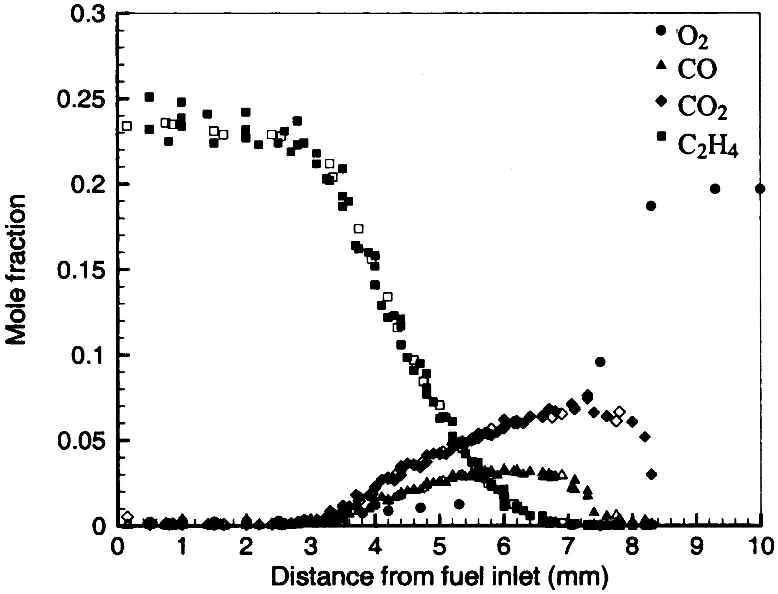

Figure 4-2. Major species profiles: Flame B (full black symbols), Flame C (open symbols), Flame D (red symbols) and Flame A (blue symbols).

Figure 4-3 compares the methane mole fractions among the five flames. Methane in the present study, unlike [36], is a minor species produced by pyrolysis and oxidation of the ethylene, and of the jet fuel or surrogates in concentrations below 100 ppm. The peaks of the methane profiles for all flames are located at z≈5.4 mm. The doped flames have virtually the same methane profiles, whereas the peaks of methane mole fraction for the baseline flames (Flames A and A*) are 15% smaller. The similarity of the methane profiles, combined with the similarities in major species and temperature that were previously discussed, lends credence to our use of these flames as a sort of flow reactor with virtually identical conditions, except for the imposed perturbation.

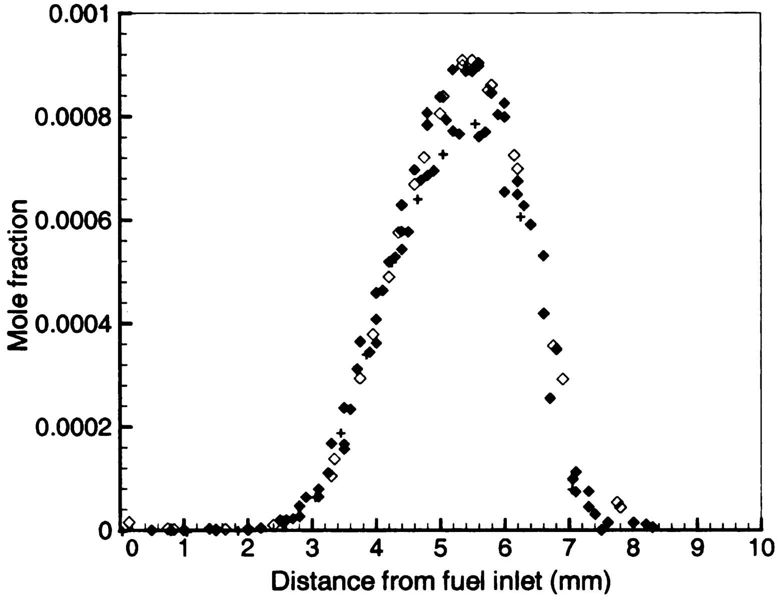

Figure 4-3. Methane mole fraction profiles: Flame B (full black symbols), Flame C (open symbols), Flame D (red symbols).

4.2. C7-C15 Alkanes

Figure 4-4 shows the profiles of the C7-C15 alkanes in the doped flames, B, C and D. Only one set of data is shown for the jet fuel doped Flame B to avoid cluttering of the figure. The iso-octane concentration in Flame B is about 0.5 ppm and it is not shown. Most alkanes in the jet fuel-doped Flame B (Figure 4-4a) disappear because of pyrolysis at z≈5 mm, except for decane, undecane, and tridecane that decay at z≈5.2 mm, and dodecane that disappears at z≈5.4 mm. In the Utah/Yale surrogate-doped Flame C, the disappearance of surrogate *iso* and *normal* paraffins is delayed to nearly z=5.4-5.5 mm.

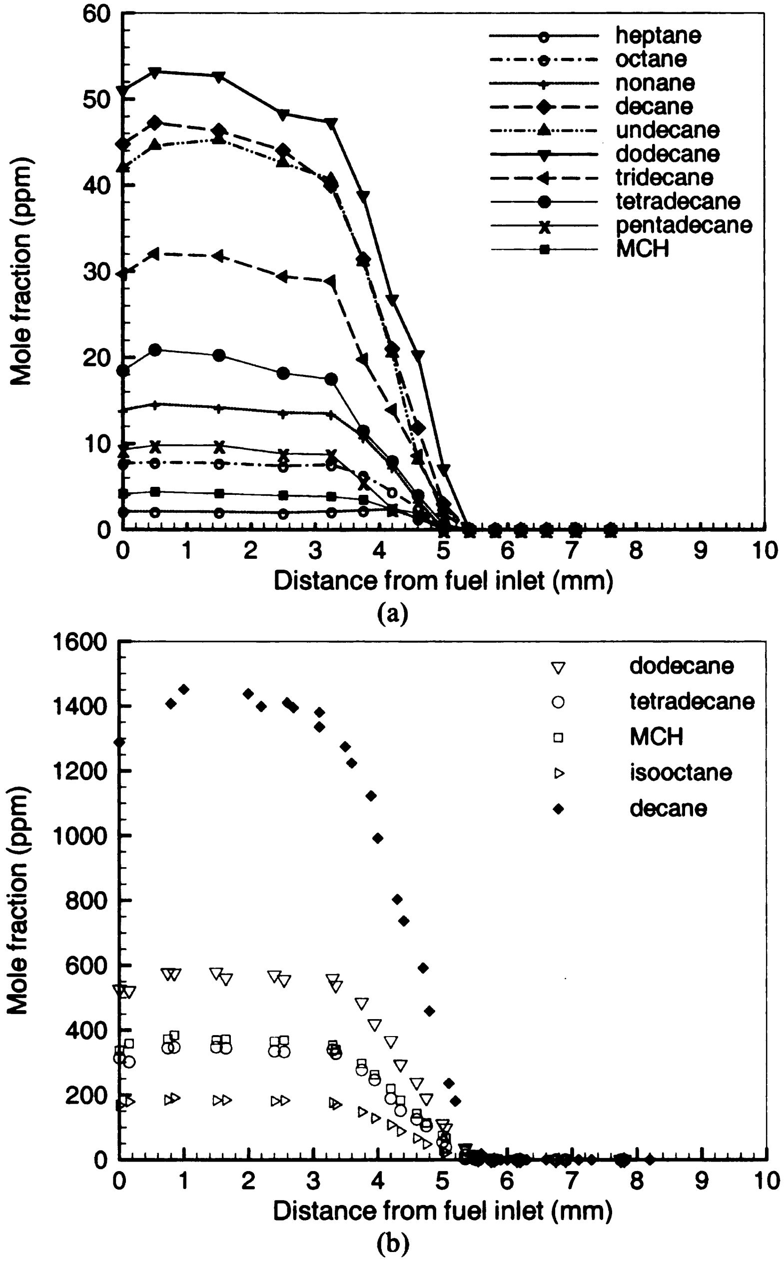

(a)

(b)

Figure 4-4. Comparison of C7-C15 Alkanes; a) Flame B, b) Flames C (open symbols) and Flame D (red symbols), Flame A (blue symbols) and Flame A* (+).

In the Aachen surrogate-doped Flame C that has only one alkane (decane), its disappearance occurs at z≈5.6 mm. The data presented here are consistent with typical decomposition of large alkanes. The observed profiles are reflective of the chemistry of jet fuel or the surrogates, since the oxidation of C_2H_4 does not yield any of these large alkanes, as also confirmed by preliminary simulations of the baseline flame with the semi-detailed Milan mechanism. Jet fuel and both surrogates show a reasonably good agreement in the pyrolysis trends of large alkanes.

Whereas the chromatograms of the surrogates are clean with distinct peaks (as shown in Figure 4-5) and the quantification of their components poses no difficulties, for complex fuel blends such as jet fuel that contain a large number of alkenes and alkylbenzenes having different isomers, the chromatograms are subject to interference. The quantification of these isomers is often affected by overlapping peaks from other molecules. As a result, the chromatogram, shown in Figure 4-6, contains a large "grassy" background and is very hard to analyze. The reason for the modest presence of alkanes in the jet fuel doped Flame B (Figure 4-4a), despite the fact that they are known to be major components of jet fuel, is because the total alkane component is spread over many different individual alkanes. The chromatogram was measured for a gaseous sample extracted near the burner mouth, that is, before any significant chemistry had taken place. The final number of species we were able to measure is 33, and another 20 were correctly identified but their quantification lacks the necessary accuracy. There is a plethora of smaller, unidentified peaks and a pedestal on which the peaks are superimposed. The presence of the pedestal prevents us from performing an accurate integration for these peaks. The dominant peaks in Figure 4-6 are associated with C9-C15 alkanes, whereas only a few of the smaller peaks, associated with smaller alkanes and aromatics, are marked. The quantified alkanes in Figure 4-6 are regarded as tracers for a broader group of large alkanes in jet fuel. Similarly, the quantified small aromatics are indicators of a larger number of similar molecules. Therefore, the present data provide a general picture of the chemical evolution in the pyrolysis and oxidation of jet fuel in a sooting diffusion flame, with the caveat that the comparison with surrogates can only be qualitative for C7-C15 alkanes or alkenes upstream of the flame zone.

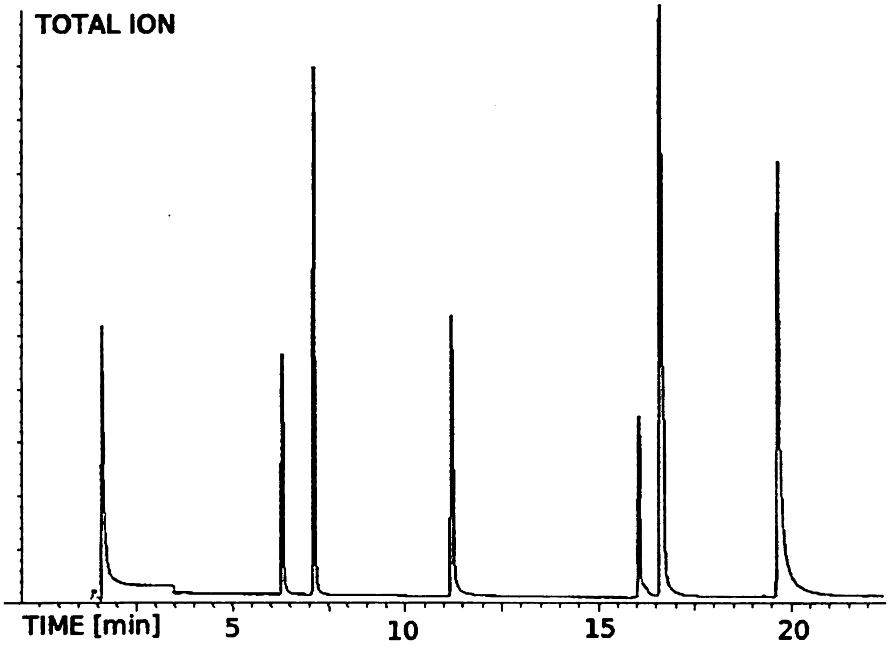

Figure 4-5. Utah/Yale surrogate chromatogram presenting distinct peaks in correspondence with nitrogen (leftmost peak) and the 6 components of the surrogate: from left to right, methylcyclohexane, *iso*-octane, *m*-xylene, tetralin, dodecane and tetradecane.

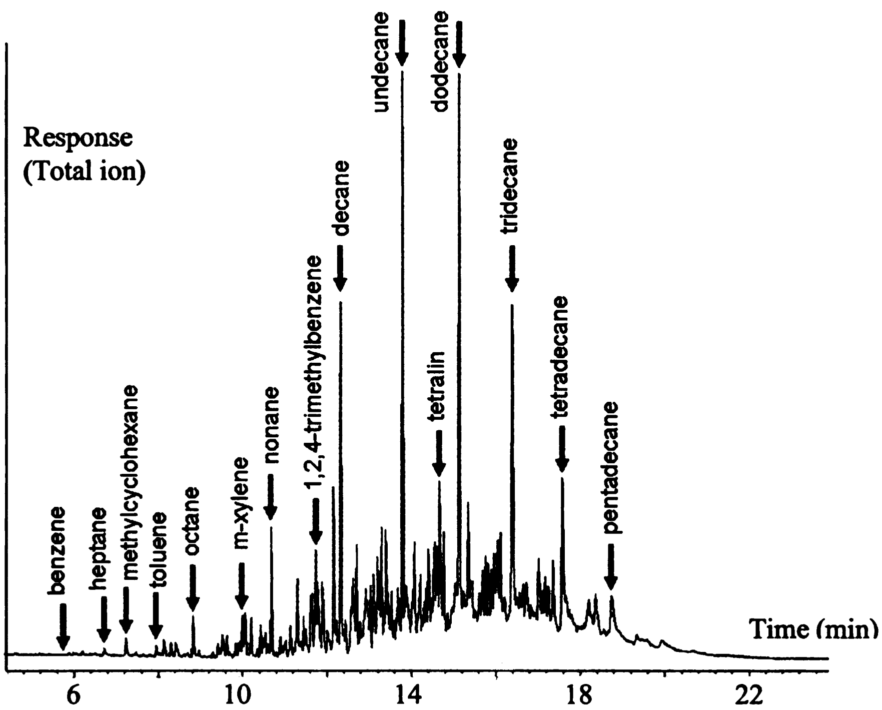

Figure 4-6. Typical jet fuel MS chromatogram, as measured from a gaseous sample extracted near the burner mouth. The arrows denote compounds that were identified and quantified.

A comparative analysis of the total carbon count helps us to evaluate the GC/MS performance with respect to large hydrocarbons. For our sooting Flames B, C and D a comparison of the total carbon counts from the liquid dopants is shown in Figure 4-7. The total carbon mole fraction excludes the contributions from major products CO and CO_2, and their primary source, C_2H_4. Unlike a similar figure in [36], it also excludes the contributions from acetylene since, as shown in Section 4.5 below, the production of acetylene is mostly attributed to the ethylene portion of the fuel. Therefore, the comparison in Figure 4-7 should account for all of the measured carbon in the parent liquid fuel dopant and their intermediate pyrolysis products. We measured approximately 6.4 times as much carbon at the fuel boundary in the surrogate-doped flames as in the jet fuel-doped flame. Yet, the actual carbon must be nearly the same at this location since the overall molecular weight and flow rates of the injected vapor are comparable in the three

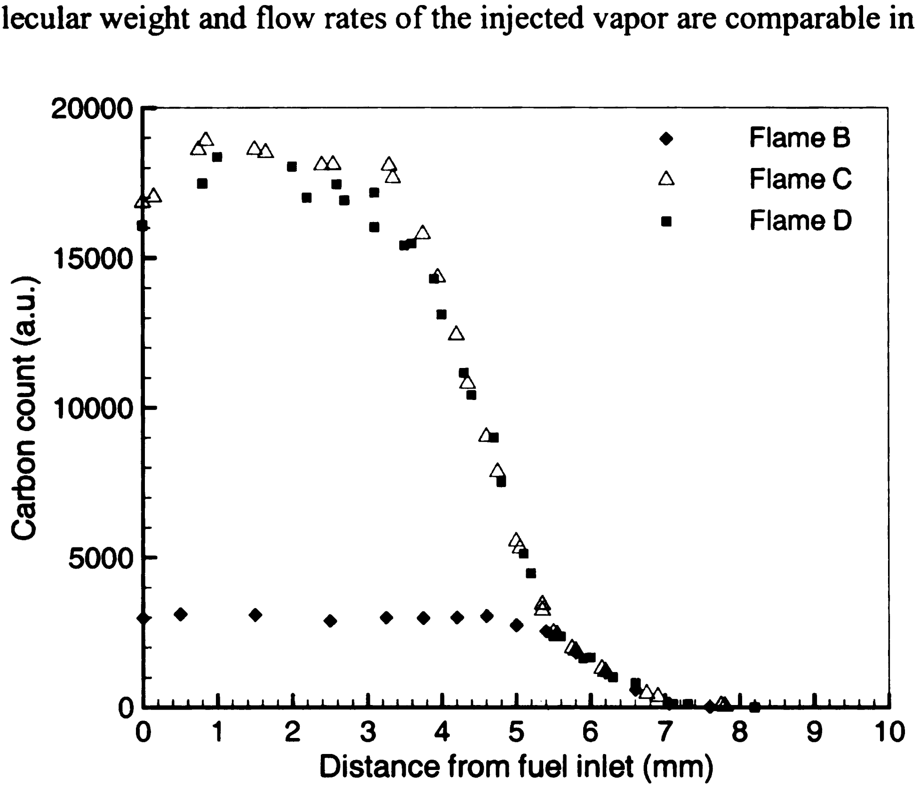

Figure 4-7. Partial carbon mole fraction profiles for Flame B (full symbols), Flame C (open symbols) and Flame D (red symbols). Contributions from ethylene, CO, CO_2, acetylene and ethane are not considered.

flames. The data for Flame B show a flat profile hovering around 3100 carbon ppm up to z ≈ 3.8 mm. For Flames C and D, the total carbon count has an initial plateau around 19,000 ppm up to z ≈ 3.3 mm, after which it monotonically decreases as CO and CO_2 are formed. This discrepancy suggests that we properly quantified only roughly 15% of the total carbon introduced as jet fuel vapor, whereas the fractions of carbon recovered from the Utah/Yale surrogate and the Aachen surrogate are roughly 93% and 92%, respectively. After z ≈ 5.4 mm, all three profiles follow a similar quantitative trend. At about $z \approx 7.7$ mm, the oxidation of dopants is completed and no carbon persists in hydrocarbons in these flames.

4.3. C7-C11 Alkenes

In the non-sooting methane flames doped with jet fuel, small quantities of 1-decene and 1-undecene were found immediately after the concentration drop of their parent alkanes [36]. None of these two olefins were detected in Flames A-D. Analysis of the C7-C11 olefins in the jet fuel doped Flame B is extremely difficult because of the overlapping spectra of multiple isomers. The largest olefins detected (and quantified) in the doped flames were 1-octene and 1-heptene. These olefinic species were not detected in Flame B. Figure 4-8 illustrates the profiles of 1-heptene and 1-octene for the Aachen

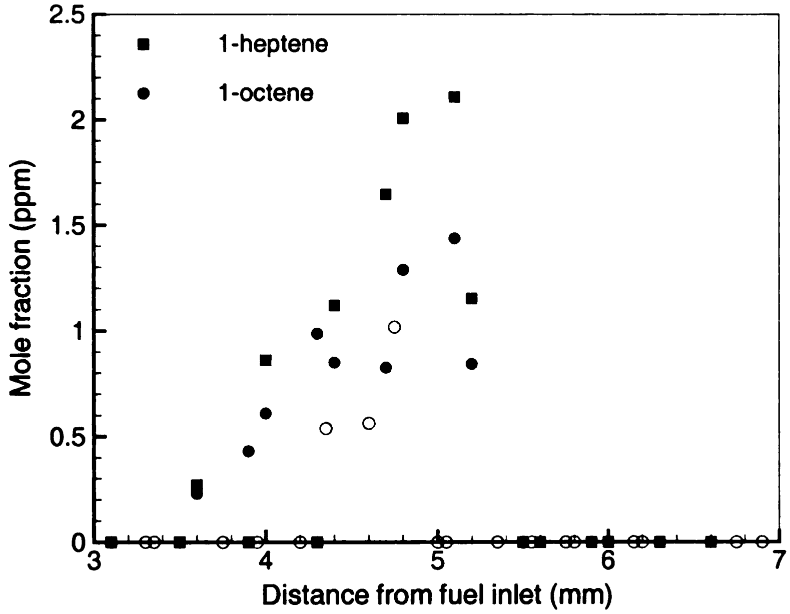

Figure 4-8. Comparison of 1-octene and 1-heptene profiles: Flame C (open symbols), Flame D (red symbols). None of these species was detected in Flame B.

and Utah/Yale surrogate doped flames (Flames C and D). The peak of 1-heptene and 1-octene appear after the concentration drop of the parent alkanes (see Figure 4-4). This is consistent with the well-known decomposition pathways for alkanes: H-atom abstraction or unimolecular dissociation to alkyl radicals, followed by beta scission of the alkyl radicals to olefins and additional alkyl radicals [57].

A difference between the surrogates with respect to the formation of olefins is observed in the presence of large olefins. As seen in Figure 4-8, in the Aachen surrogate Flame D, about 2 ppm of 1-heptene and 1.5 ppm of 1-octene were quantified near the peak of the C5-C6 olefins (z≈4.9 mm shown in Figure 4-9). On the other hand, in the Utah/Yale surrogate Flame C, only 1-octene was detected, but peaks for cyclohexene and methylcylohexene were observed. Figure 4-9 shows the profile of cyclohexene for Flame C.

4.4. C3-C6 Alkanes, alkenes and dienes

4.4.1. C5-C6 Alkenes

Figure 4-9 illustrates how C5 and C6 olefins, such as 1-pentene and 1-hexene, are formed as larger alkanes decompose in Flames A-D. There was no detectable 1-hexene in the baseline ethylene Flame A. Smaller concentrations of 2-hexene and 3-hexene, on the order of 1 ppm, were identified in some of the doped flames. The profiles of 1-pentene and 1-hexene show peaks at z≈ 4.9 mm. Comparison of Figure 4-9 with the profiles of alkanes in Figure 4-4 confirms that these olefins are formed as the fuel alkanes are decomposing. Flames B, C and D show good agreement in their 1-pentene profiles, with significantly larger concentrations as compared to the baseline Flame A. The agreement with respect to 1- hexene on the other hand is relatively poor, especially for Flame C. The Utah/Yale surrogate-doped flame has nearly 2.7 times as much 1-hexene as the jet fuel-doped flame, while the Aachen surrogate-doped Flame D has a peak 1-hexene value almost 50% larger than that of jet fuel doped flame.

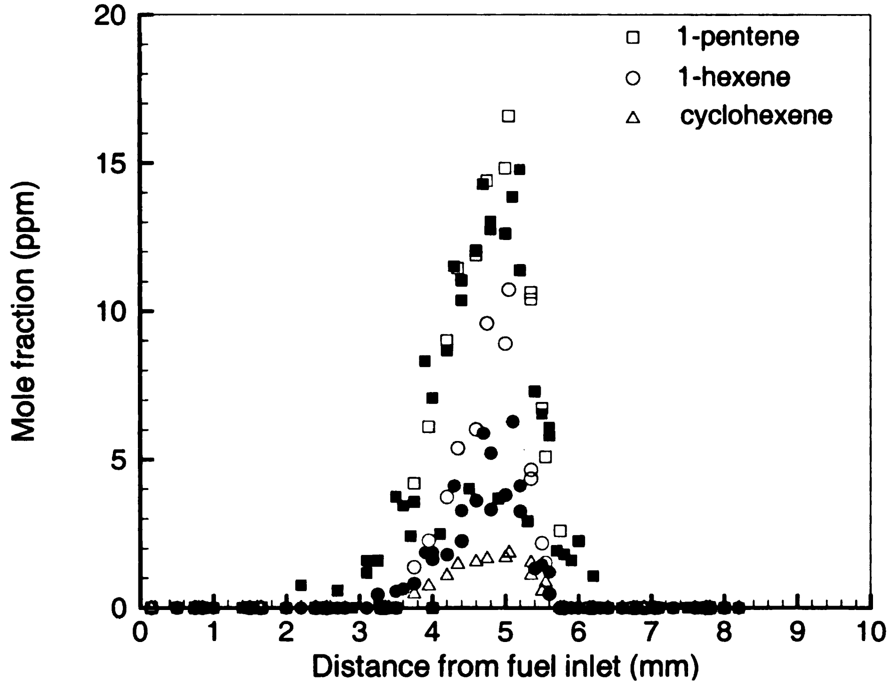

Figure 4-9. Comparison of C5-C6 alkenes profiles: Flame B (full black symbols), Flame C (open symbols), Flame D (red symbols) and Flame A (blue symbols).

4.4.2. Quantification of dienes

The overlapping spectra of multiple isomers make the analysis of larger olefins in the jet fuel doped flames extremely difficult. Similar challenges are posed by the quantification of dienes. The only diene that was detected and quantified in the jet fuel and other flames is cyclopentadiene (C_5H_6), which is shown in Figure 4-10. Oxidation of ethylene by itself produces cyclopentadiene in the order of 4 ppm. Both surrogates overpredict cyclopentadiene although they show a similar trend with respect to the location and magnitude of the peak. The Utah/Yale surrogate doped Flame C produces nearly 1.5 times more cyclopentadiene than the jet fuel doped Flame B. The cyclopentadiene peaks appear further downstream as compared to the peaks of C3-C8 olefins.

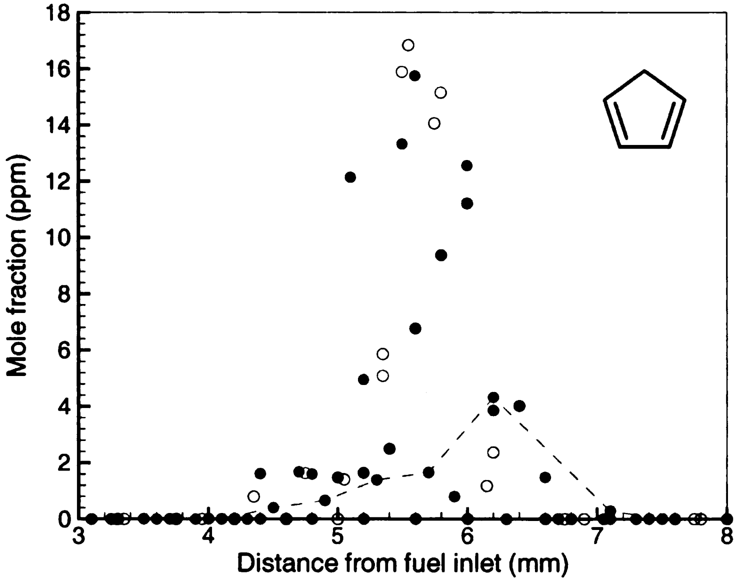

Figure 4-10. Comparison of cyclopentadiene profiles: Flame B (full black symbols), Flame C (open symbols), Flame D (red symbols) and Flame A (blue symbols).

4.4.3. C3 alkanes and alkenes

Figure 4-11a shows the profiles of 1-propene for Flames A, A*, B, C, and D. The baseline ethylene flames (Flames A and A*) produce similar propene mole fractions, but the doped flames produce noticeably different propene profiles. The propene mole fraction is significantly larger than other alkenes, except obviously for the fuel species ethylene, and the peak mole fraction appears slightly after the peak of larger alkenes. The propene mole fraction peak for all three doped flames occurs at z ≈5.2 mm with the highest magnitude for jet fuel (Flame B) and the lowest for the Aachen surrogate (Flame D). The difference between propene mole fraction profiles of jet fuel/surrogate-doped flames and baseline flames can be attributed to the beta-scission of large alkyl radicals all

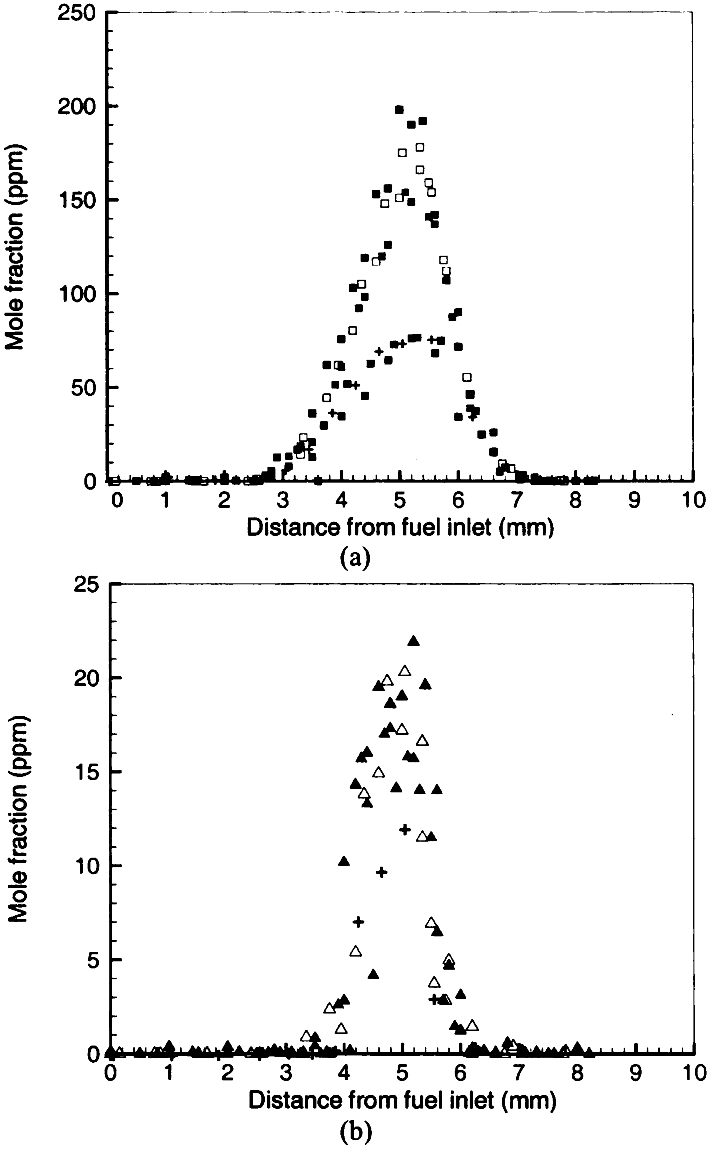

Figure 4-11. Comparison of profiles of a) 1-propene and b) propane: Flame B (full black symbols), Flame C (open symbols), Flame D (red symbols), Flame A (blue symbols) and Flame A* (+).

the way down to the smallest alkenes. We note that the ability of both surrogates to predict the jet fuel behavior with respect to the formation of alkenes gets better for smaller alkenes, probably because many more pathways can produce the smaller alkenes and so the specific details of the fuel alkane structure are less important. It is noteworthy to compare the ordinate of the profiles of C7-C8, C5-C6, and C3 alkenes. The ordinates show at least one order of magnitude difference.

Figure 4-11b shows profiles of propane; no butane, pentane, or hexane were detected. A comparison of the location of the propane peaks with the disappearance location of the larger alkanes in Figure 4-4 indicates that this small alkane is a product of the decomposition of the larger ones. The contribution of ethylene in the production of propane is well pronounced in Figure 4-11b. The non-sooting methane flame doped with jet fuel and the Utah/Yale surrogate had almost 3 times as much propane as the sooting flames (Flames B and C here), which can be attributed to impurities in the methane source used in those experiments [36]. Also, in the non-sooting flames, small amounts of iso-butane, pentane and hexane were detected, which can be attributed to the fuel source impurities or their production in the flame.

4.5. C2 Hydrocarbons

Figure 4-12 compares the measured C2 species in Flames A to D and Flame A*. Ethylene is a major species in the fuel stream and its trend was presented in Figure 4-2. In the previous experiments on non-sooting methane flames doped with either jet fuel or the Utah/Yale surrogate, the latter overpredicted the ethylene concentrations, but accurately reproduced the ethane and acetylene concentrations [36]. Figure 4-12a shows a good agreement between ethane profiles in all the incipient sooting ethylene flames. Ethane is

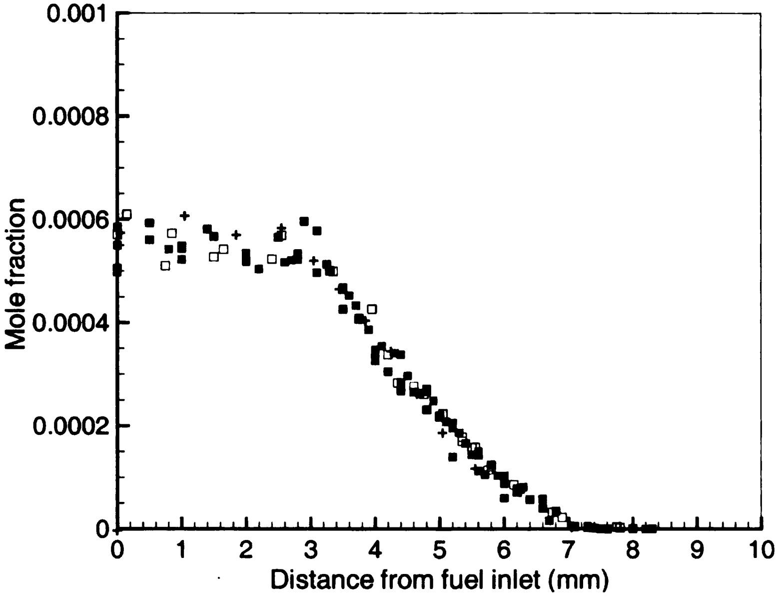

(a)

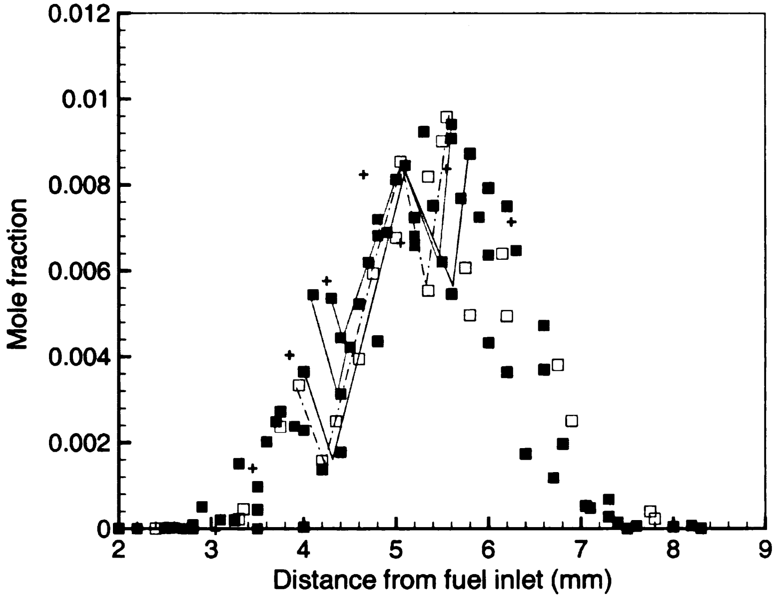

(b)

Figure 4-12. Profiles of molar fractions of a) ethane and b) acetylene: Flame B (full black symbols), Flame C (open symbols), Flame D (red symbols), Flame A (blue symbols) and Flame A* (+).

an impurity in the fuel source, and it shows trends similar to ethylene, that is, its maximum concentration occurs at the fuel boundary, its concentration decreases throughout the flame zone, and the dopants do not make a noticeable contribution to its concentrations in the baseline flame.

Acetylene, shown in Figure 4-12b, presents a unique behavior that differs in two main ways from the non-sooting methane flame. First, the peak of the acetylene profile in the sooting flames is nearly 19 times larger than the acetylene peak in the non-sooting flames, as expected in these sooting flames, since acetylene is a major surface growth species in soot formation. Second, the profiles show a multimodal behavior as evidenced by the continuous lines in the figure. At first glance this behavior may seem to be an experimental artifact. However, it is reproducible. For Flames A-D, at least two sets of experiments were conducted to confirm the reproducibility of data and this behavior was observed in all experiments. Also, if it were an artifact of the GC/MS performance or the experimental technique, we would detect multimodal behavior in other minor species such as methane or ethane with much lower absolute concentrations than acetylene, but we do not (see Figure 4-3 and Figure 4-12a). The results for ethane in Figure 4-12a at distances less than 3 mm from the fuel inlet indicate the approximate random uncertainty in the measurements, which is 4 %; the changes in the acetylene concentration due to the multimodal behavior are much larger, 20-50 %. Moreover, this multimodal behavior was not observed in the non-sooting experiments using the same instrument, leading us to conclude that the acetylene participation in soot growth pathways may cause this behavior. The first drop in acetylene profiles occurs at $z \approx 3.5$-4.5 mm. The peak of the acetylene mole fraction is at $z \approx 5.5$-5.8 mm for all flames and the bulk of the acetylene profile occurs where ethylene is still present (ethylene disappears roughly at $z \approx 7$ mm). It is difficult to discriminate between the peak concentrations of acetylene in Flames A-D. This suggests that acetylene, which is present at very high concentrations in these flames, is mainly produced by ethylene.

Some important reactions that form single ring aromatics involve acetylene [56]. Also, acetylene is a particle surface growth species, as further discussed in the next section. The first drop in the acetylene profiles (Figure 4-12b) can be attributed to the early stages of formation of benzene and other large pyrolysis products through reactions involving acetylene. Pyrolysis reactions of acetylene can form many products other than benzene. This drop is right before the benzene peak. The second drop may be a result of participation of acetylene in surface growth. Future studies with the use of Laser-Induced Incandescence (LII) to measure soot would confirm this hypothesis.

4.6. Aromatics

Flames A-D were deliberately selected to be at the onset of soot formation to assess the behavior of jet fuel and its surrogates with respect to the formation of critical precursors in soot formation, such as aromatics. The non-sooting methane flames doped with jet fuel and the Utah/Yale surrogate revealed significant discrepancies with respect to benzene and toluene [36], which was cause for concern in the soot context. The present study considers also the Aachen surrogate (Flame D) that was found to reproduce successfully soot volume fraction profiles of jet fuel flames [11].

Calibration data is available for the following aromatic species and, therefore, they can be quantified:

1) Tetralin (1,2,3,4-Tetrahydro naphthalene, $C_{10}H_{12}$)

2) *m*-xylene (1,3-dimethyl benzene, C_8H_{10})

3) *p*-xylene (1,4-dimethyl benzene, C_8H_{10})

4) 1,2,4-trimethyl benzene (TMB, C_9H_{12})

5) Benzene (C_6H_6)

6) Toluene (C_7H_8)

Some other aromatics and PAH's (Polycyclic aromatic hydrocarbons) are important as soot precursors. These may include styrene (ethenyl benzene) and some PAH's such as naphthalene, anthracene, phenanthrene, pyrene, chrysene, tetracene, and coronene. Some of these species can be identified by the MSD, but no calibration data is available for their quantification. For instance, calibration of naphthalene (a critical bottleneck to soot) poses significant difficulties. Identification of some larger PAH's needs different analytical approaches.

Figure 4-13 shows a comparison of three aromatics, namely, tetralin, m-xylene and 1,2,4-trimethylbenzene (TMB), among Flames B-D, with different ordinate scales in Figure 4-13a and in its magnified version, Figure 4-13b. None of these aromatic species were detected in the baseline ethylene flames (Flames A and A*). P-xylene can also be detected and quantified in the doped flames, but it has much lower concentrations and follows a profile similar to that of m-xylene in Flame D. The accuracy of the tetralin calibration is uncertain and its profile is qualitative. In Flame B, tetralin, m-xylene, and TMB were identified and quantified. These species are considered tracers of the

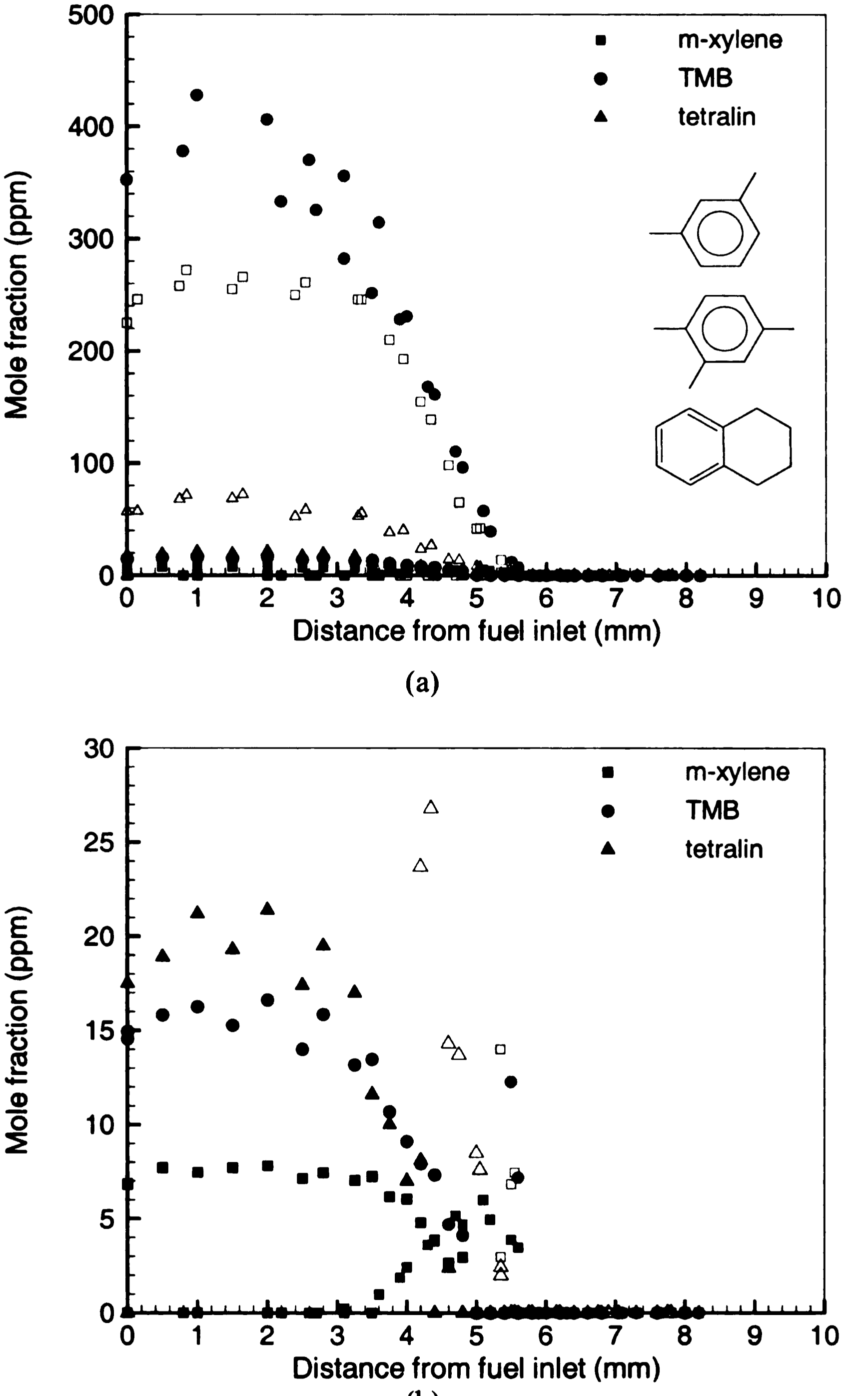

(a)

(b)

Figure 4-13. Comparison of profiles of m-xylene, tetralin, and 1,2,4-trimethylbenzene with compressed (a) and expanded (b) ordinate scales: Flame B (full black symbols), Flame C (open symbols) and Flame D (red symbols).

multitude of aromatics in the jet fuel. They decay roughly at $z \approx 5.1$ mm. In Flame C that was doped with the Utah/Yale surrogate, m-xylene and tetralin are the only aromatic components of the surrogate. Since these components represent a large group of aromatics in the jet fuel, the disagreement of the profiles near the fuel inlet, away from the reaction zone, is not surprising. The same consideration applies to the aromatic component of the Aachen surrogate.

In Flame D, which is doped with the Aachen surrogate, TMB is the sole aromatic compound, which decays at $z \approx 5.8$-6 mm, which is close to where the only aliphatic compound, n-decane, decays. A small peak of m-xylene (5-6 ppm) is observed in Flame D at $z \approx 5.1$ mm, which is close to the peaks of benzene and toluene. Xylene can be formed from TMB by chemical pathways that replace a methyl side-chain with an H atom. Very small quantities of styrene were detected within $z \approx 3.6$-5.1 mm, but no detectable tetralin and naphthalene were found in Flame D. Also, styrene and naphthalene (not shown here) were detected in Flame C, within the regions of $z \approx 3.3$-5 mm and $z \approx 1.6$-4 mm, respectively. Naphthalene could not be measured closer to the reaction zone because its GC/MS retention time is too close to that of dodecane. No naphthalene and styrene could be measured anywhere in the jet fuel flame (Flame B) because of the difficulty in species separation for jet fuel.

4.6.1. Benzene and toluene

The two aromatic compounds that could be measured cleanly in all of the doped flames, and therefore that could be used as tracers of aromatics and soot formation, are benzene and toluene. Figure 4-14 illustrates how these compounds are related to the formation of the two-ring aromatic naphthalene, which is a critical bottleneck to soot formation. Benzene is an intermediate in the growth of aliphatics (e.g. methylcylcohexane, iso-octane, and dodecane) to naphthalene, and toluene is a byproduct of the growth of n-alkylbenzenes (e.g., ethylbenzene, propylbenzene) to naphthalene via benzyl radical. We focus on toluene instead of benzyl radical because we cannot detect radicals.

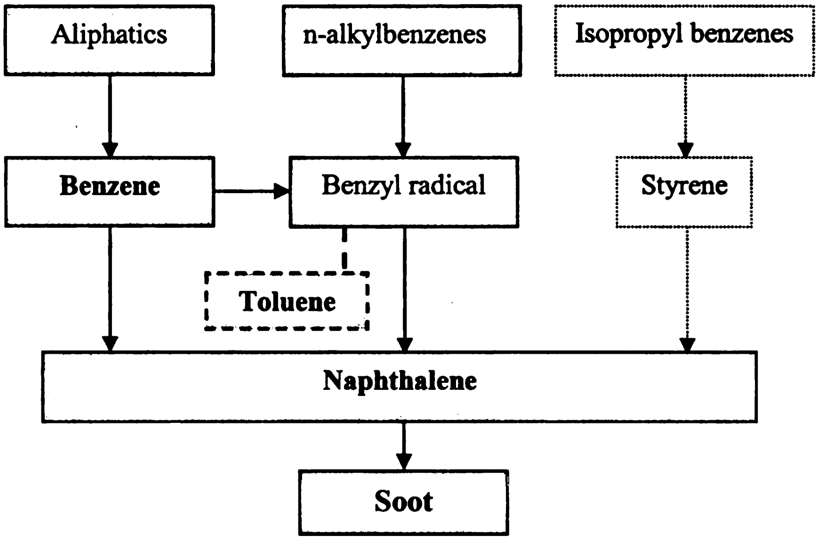

Figure 4-14. Global pathways of naphthalene formation. Isopropyl benzenes and species with similar structure are rare in the fuels under study.

A comparison for benzene and toluene among the various flames is shown in Figure 4-15 and Figure 4-16, respectively. Significantly, even in the case of the jet fuel (Flame B), whose chromatograms are the most difficult to analyze, benzene and toluene can be measured with small uncertainties, since they do not have multiple isomers and they appear early in the chromatogram, before the time when the "grassy" baseline arises (see Figure 4-6). In fact, the GC/MS has a better performance in separating the jet fuel intermediate species as z increases and the large fuel compounds and their isomers are pyrolyzed and partially oxidized. Indeed, the profiles of carbon count in Figure 4-7 suggest that beyond z ≈ 5.3 mm, the total carbon counts are consistent between Flames B, C and D and the comparison is quantitative. This region is in the vicinity of peaks of benzene and toluene mole fractions.

Figure 4-15 shows good agreement between the surrogates and jet fuel with respect to the location and magnitude of the benzene mole fraction peak. The doped flames produce much more benzene than the two baseline ethylene flames (A and A*), which means that maximum concentrations in the doped flames reflect aromatics formation from the dopants. The agreement is better for Flame C (Utah/Yale surrogate) than for

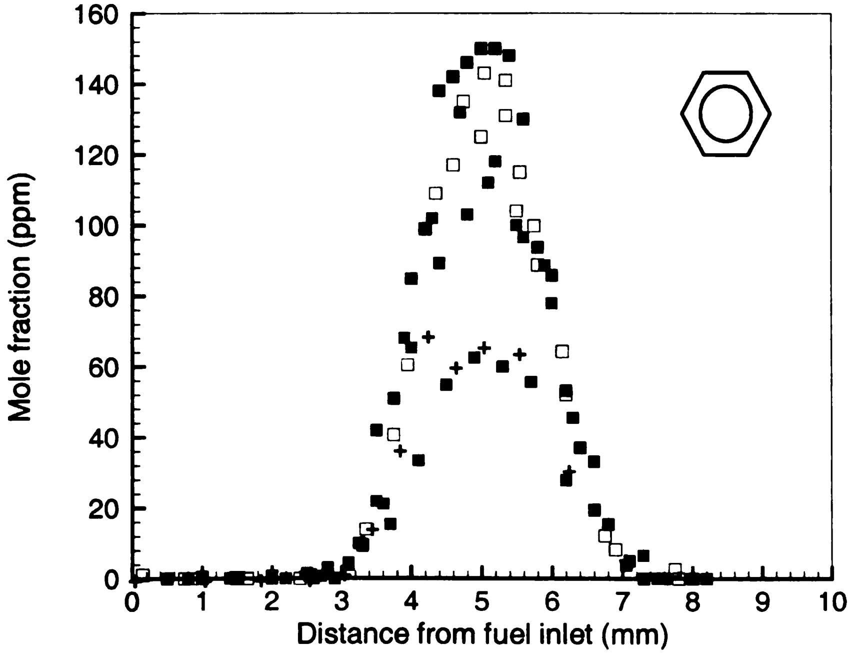

Figure 4-15. Comparison of profiles of benzene mole fractions: Flame B (full black symbols), Flame C (open symbols), Flame D (red symbols), Flame A (blue symbols) and Flame A* (+).

Flame D (Aachen surrogate). Although the benzene profiles in the Aachen surrogate flame (Flame D) and the jet fuel flame (Flame B) follow similar trends, the Aachen surrogate produces nearly 20 % less benzene than jet fuel. The sooting jet fuel doped Flame B produces nearly 2.5 times more benzene than the non-sooting jet fuel doped methane flame [36].

Comparison of toluene mole fractions in Figure 4-16 shows reasonably good agreement between Flame B and Flame C. Small amounts of toluene are present in the parent jet fuel causing the mole fractions to be nonzero for small values of z. Toluene was not detectable in Flames A and A*. The much larger toluene/benzene ratios in the doped flames versus the undoped flames indicate that the toluene in the doped flames is primarily formed from the aromatic components of the jet fuel and surrogates independently of benzene formation. The agreement between Flame B and Flame D is

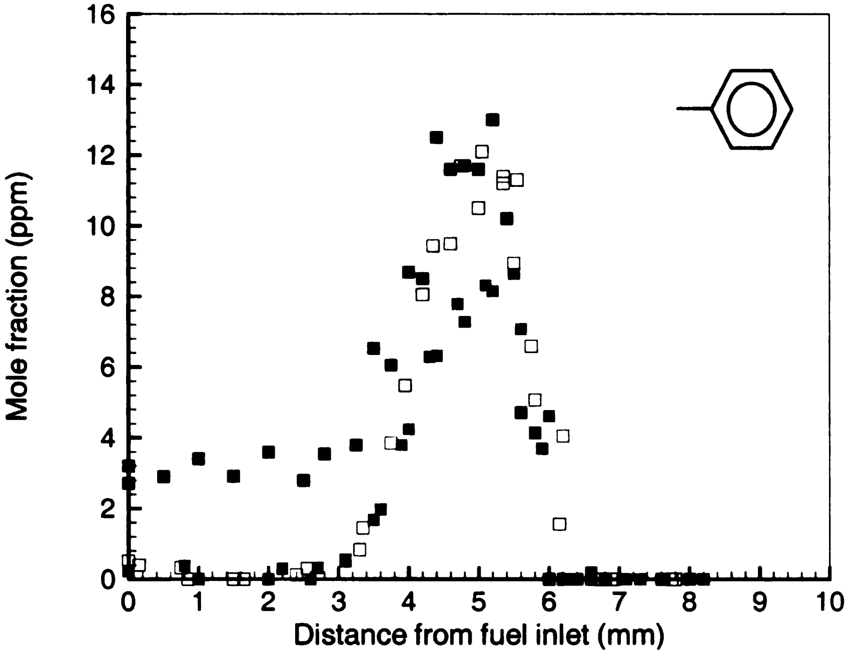

Figure 4-16. Comparison of profiles of toluene mole fractions: Flame B (full black symbols), Flame C (open symbols) and Flame D (red symbols).

also reasonable, with nearly similar peak location, but the peak magnitude is almost 30 % smaller in Flame D. These observations suggest that, despite its simplicity, the Aachen surrogate has an acceptable agreement with jet fuel in incipient sooting conditions with respect to aromatic formation.

In summary, it would appear that the discrepancies between jet fuel and surrogates that were observed under non-sooting conditions [36] are not present in the current, and more relevant, situation of incipient sooting.

4.6.2. Effects of component chemical class

Following the kinetic pathways from each surrogate component to benzene or toluene is difficult. However, it is quite informative to compare the relative contribution of each chemical class of components to the formation of benzene or other important soot precursors. This would guide researchers to modify the formulation of the surrogates in order to match the critical profiles of soot precursors and eventually the sooting behavior. Table 4-1 presents the concentrations of each chemical class in the jet fuel and two surrogates used. Each chemical class represents a molecular structure.

Two recent efforts on *premixed* flames by the Professor Sarofim's group at University of Utah are reported here. As mentioned before, *aliphatics* are virtually responsible in benzene formation. Studies of Zhang et al. [65] on *premixed* flames shed light to the relative significance of each class of paraffins in benzene formation suggesting a trend *cyclo*-paraffins > *iso*-paraffins > *normal*-paraffins. Specifically for the constituents of the Utah/Yale surrogate in a premixed flame scenario, the study shows that methylcyclohexane produces much higher benzene concentrations than *iso*-octane

Table 4-1. Concentrations of each chemical class in the jet fuel and two surrogates. Values are in vol%.

	"Average" jet fuel from Wright-Patterson Air Force Base (WPAFB), POSF No. 4658	Utah/Yale Surrogate	Aachen Surrogate
(n- and i-) paraffins	55.2	72.98	82.76
monocyclo-paraffins	17.2	13.6	
dicyclo-paraffins	7.8		
alkyl benzenes	12.7	9.78	17.24
indans and tetralin	4.9	3.64	
naphthalenes and trycylco-paraffins	2		
alkyl benzenes + indans + tetralin=	17.6	13.42	17.24

while *iso*-octane forms relatively more benzene as compared to dodecane. As a result, the adjustment of relative concentrations of these *cyclo*, *iso*, and *normal* paraffins may increase or decrease the total formation of benzene. Moreover, noteworthy is the recent study of Zhang et al. [66] on 22 *premixed* flames of C_1-C_{12} fuels, which corroborates the structure-dependency of benzene formation, for example, when a kerosene mixture, *n*-decane and *iso*-octane were compared.

Extension of data available for benzene formation in premixed flames to *non-premixed* flames (similar to Flames A-D) is not always accurate. One reason might be different levels of H and OH radical concentrations. For non-premixed flames, only general sooting tendencies, which have long been studied, are reported. It should be noted that overall (global) measures of sooting tendency such as smoke point are not representatives of the trends in benzene formation or early stages of soot formation.

Early studies on the effect of molecular structure of pure hydrocarbons on sooting tendency in laminar *diffusion* flames show that the general sooting tendency trend for hydrocarbons is [67]

n-paraffins < branched paraffins ≈ naphthenes < alkenes < alkynes < alkylbenzenes < naphthalenes.

This trend is not strictly followed because different hydrocarbon classes may behave differently as carbon number increases. The sooting trend for individual components in the Utah/Yale surrogate is

tetralin > m-xylene > *iso*-octane > tetradecane > dodecane > methylcyclohexane.

When these pure hydrocarbons are mixed the general sooting tendency should be assessed for the mixture.

The focus of this study was not on the final stages of soot formation. Instead, we considered the decomposition and oxidation of fuels leading to the formation of small aromatics that are important since they grow eventually to soot. Tentative trends for soot formation using a global scale of sooting tendency are briefly discussed in the next section.

4.6.3. Threshold sooting index (TSI)

To study the sooting tendency of surrogate fuels, Yang et al. [67] used the threshold sooting index (TSI) [68]. The TSI, which is an arbitrary scale for the sooting tendency of hydrocarbon fuels, for diffusion flames is defined by

$$\mathrm{TSI} = a\,(\mathrm{MW}/\mathrm{SP}) + b, \qquad (4\text{-}1)$$

where MW is the fuel molecular weight [g/mol], SP is the fuel smoke point [69], and a and b are constants dependent on the apparatus used for smoke point measurements (and scale the TSI from 0 to 100). Ethane and methylnaphthalene are assigned the TSI ratings of 0 and 100, respectively. Table 4-2 lists the TSI, aromatic content, H/C ratio, and cetane number for jet fuel and surrogate mixtures. The TSI of the JP-8 is somewhat uncertain since its composition varies, but values in the literature range from 15 to 26 [70]. We have calculated the TSI of the Utah/Yale and Aachen surrogates using the mixing rule [67],

$$TSI_{mix}=\Sigma x_i TSI_i, \tag{4-2}$$

where x_i is the mole fraction of the individual components. TSI values for pure hydrocarbons are obtained from the work of Olson et al. [71]. The TSI of the Utah/Yale surrogate, which contains 13.4 (liq. Vol) % aromatics, is 14.6, while that of the Aachen

Table 4-2. TSI, aromatic content, H/C ratio, and cetane number for jet fuel and surrogate mixtures.

	TSI_{mix}	Aromatics (vol %)	H/C Ratio	CN_{mix}
JP-8	15.72-25.66	17.86	1.909	31.8-56.8
Jet-A	19.71-22.17	17.58	Not reported	Not reported
Utah/Yale surrogate	14.63	13.4	1.99	61.57
Aachen surrogate	15.11	17.24	2.017	65.22

surrogate which contains 17.2 (liq. Vol) % aromatics, is 15.1. Aromatics account for roughly 18 vol % of jet fuel [61]. By consideration of this global measure of sooting tendency one would expect a tentative trend for soot formation: jet fuel > Aachen surrogate > Utah/Yale surrogate.

Some researchers [70] have utilized cetane numbers (CN) as representatives for autoignition when various surrogate mixtures were compared. The mixture cetane number (CN_{mix}) is calculated using

$$CN_{mix}=\Sigma v_i CN_i, \tag{4-3}$$

where v_i is the volumetric fraction of the individual components. CN values for pure hydrocarbons (CN_i) are taken from the work of Santana et al. [72]. Our study took advantage of the detailed probing of the diffusion flame as well as spatial temperature measurements. Indeed, this detailed flame structure study provided a wealth of information that would better illustrate the ignition behavior of complex fuels as opposed to the utilization of a global measure like the cetane number.

4.6.4. Possible role of the antistatic additive

A final issue to consider is the influence of trace amounts of sulfur compounds in jet fuel (about 490 ppm) on the formation of soot precursors. The sulfur trioxide reaction $H+SO_3 \rightarrow OH+SO_2$, in the late pyrolysis process of diffusion flames forms the hydroxyl radical that attacks soot precursors and suppresses soot formation [57]. The good agreement in aromatics behavior and the similarity of flame appearance under incipiently sooting conditions suggest that the presence of sulfur in the parent liquid plays a negligible role. However, the situation is more complex in the present experiments relying on the electrospray for fuel dispersion. The electrospray can operate successfully so long as the fluid has a finite electric conductivity, which is not the case for hydrocarbons. Consequently, we need to add 0.05% (by volume) of an antistatic additive, Octel Stadis 450, to elevate the liquid electrical conductivity. This additive is also present in some jet fuels (such as JP-8) as a static dissipater for in-flight refueling, at concentrations not exceeding 80 ppm. It contains up to 30% in sulfur compounds [61, 73], which corresponds to a maximum of 0.018 % (by weight) in a surrogate mixture. These sulfur compounds are present in an oil-soluble sulfonic acid, which is a constituent of the Stadis. According to Henry [61, 73], a suitable sulfonic acid is mono and di sulfonates of alky benzenes, and in one aspect is dinonylnaphthyl sulfonic acid or doecylbenzene sulfonic acid. The Octel Stadis 450 that was used in the lab contained the former. To ascertain if the additive played any role, we performed the following experiment: we selected a flame with boundary conditions similar to Flame B except for the dopant that was jet fuel at 3000 ppm, to ensure a more pronounced soot-laden zone. In a separate experiment, the liquid fuel was spiked with 4-dodecylbenzene sulfonic acid ($C_{18}H_{30}O_3S$, CAS Number: 121-65-3), yielding a five-fold increase in the sulfur contribution as compared to that in jet fuel and from the Stadis. No distinct changes in the soot zone luminosity (see Figure 3-4) and thickness were observed, which suggests that the observed trends in terms of soot and soot precursors are not an artifact associated with the antistatic additive.

Part II

Biogas Combustion and Chemical Kinetics

Chapter 5 Background and Introduction to Biogas Combustion Research

Increasing global energy demands along with limited resources and environmental concerns, has led to the exploration of environmentally-friendly new and diverse energy resources. Consequently, there is a challenge for combustors to use fuels with variable compositions from diverse energy resources. There is an anticipated increase in the use of renewable energy. In recent years, there has been a significant emphasis on the study of production, commercialization, and combustion characteristics of bio-derivative fuels. Biogas is a renewable and biodegradable energy source that can be used for the transportation sector, farm communities, small-scale power generation, and large gas turbines as a complementary fuel (e.g., to natural gas). Constraints like the cost of cleaning and upgrading to remove CO_2, limit the use of biogas. Most newly built stationary power-generating gas turbines use natural gas incorporating dry low NOx technologies based on lean-premixed combustion to meet emissions regulations. Therefore, the combustors operate under conditions near the lean limit of their stability domains where flame blowoff, noise, and instability can adversely influence engine performance and reliability [74].

There is an interest in using industrial fuel-flexible gas turbines near the alternative fuel production sites which can produce their own fuel, for example farm communities. The capability of new gas turbine technologies should be extended to a wider range of potentially commercial, low quality fuels such as biogas. An acute issue in the combustion of biogas as well as its integration with electricity generation that must be investigated is varying gas compositions and heating values. Biogas composition depends on many factors, particularly the management of the process and the nature of the feedstock material. Composition variability places considerable challenges on the gas turbine industry because low emission combustion systems are typically optimized to operate with a single specific fuel (such as natural gas) with tight specifications. Also, combustion instability problems become more serious in biogas-driven gas turbines as a result of fuel composition and fuel-air ratio variability.

In this chapter, composition, production and pre-processing of biogas are explained. The economic and environmental benefits of the utilization of biogas as a renewable energy resource, as well as its potentials to replace fossil fuels for power generation are discussed. The status of current gas turbines that use a wide range of fuels, specifically biogas of different sources, is reviewed. Some challenges of fuel flexible gas turbines utilizing biogas are addressed.

5.1. Biogas Production and Benefits

5.1.1. Biogas composition and upgrading

Biofuel is any fuel that is derived from biomass. It is a renewable and biodegradable energy source, unlike other natural resources such as petroleum, coal and nuclear fuels. One definition of biofuel is any fuel with an 80% minimum content by volume of materials derived from living organisms harvested within the ten years preceding its manufacture [75].

Biogas typically originates from the anaerobic digestion of biomass and diverse organic wastes by micro-organisms. Sources of organic waste include [76]: agricultural wastes and manure, animal by-products, industrial wastes, municipal solid wastes, sewage sludge and other biodegradable wastes. Different articles in the literature report diverse constituents for biogas because each considers a particular organic source of interest. The corresponding composition varies because of that specified source. Wellinger and Lindberg [77] report a very complete description: Biogas produced in anearobic digestion plants or landfill sites is primarily composed of methane (CH_4) and carbon dioxide (CO_2) with smaller amounts of hydrogen sulphide (H_2S) and ammonia (NH_3). Trace amounts of nitrogen (N_2), hydrogen (H_2), carbon monoxide (CO), oxygen (O_2), and dust particles are occasionally present in the biogas, which is usually saturated with water vapor. It may also contain siloxanes*. Biogas is sometimes called swamp gas, landfill gas or digester gas. It can be called renewable natural gas (RNG) when its composition is upgraded to a higher standard of purity.

Constituents in biogas are sometimes similar to those of a raw (non-conventional) natural gas. Raw natural gas leaving the well contains a series of other species [78]: (a) CO_2 up to 25 vol. % (aged natural gas), (b) N_2 up to 70 vol. % (weak natural gas), (c) sulphur compounds: H_2S (sour natural gas), (d) ethane, liquefied petroleum gas, and condensates (rich natural gas). These constituents are usually removed before

---

* Siloxanes ($C_xH_ySi_zO_w$) are used in household and commercial products and find their way into wastewater and landfill solid waste, thus, volatilize into digester gas and landfill gas. During combustion SiO_2 is formed and found in the form of a white powder in gas turbine hot section components and as a light coating on post-combustion catalysts. Microturbine and catalyst failures have focused industry-wide attention on siloxanes.

liquefaction or compression. Some gas turbines can burn a raw natural gas fuel. Similar to a raw natural gas, biogas is a viable alternative candidate fuel for gas turbines.

In this work, the interest is in the study of biogas originating from anaerobic digestion from the following sources:

i- Biogas of methanization: Anaerobic micro-organisms in the absence of oxygen digest wet organic material (in a digester). Anaerobic digestion is also called fermentation or methanization. It needs a warm environment to typical temperatures of at least 30 °C.

ii- Landfill biogas: Landfills are a large source of biogas. Here, anaerobic digestion of wastes occurs naturally. Gas collection is practical for landfills that are at least 40 feet deep and contain at least one million tons of waste [79]. Anaerobic digestion of municipal solid waste in this oxygen free environment primarily produces CH_4 and CO_2. Despite the fact that producer gas or syngas, produced from slow pyrolysis or gasification of organic wastes or wood (with main constituents, H_2 and CO), is sometimes named biogas, our work is solely focusing on biogas from biomass anaerobic digestion or landfill gas.

Scott et al. [80] report an average composition for biogas produced in Dairy Anaerobic Digestion (AD) Plants, which is $CH_4 = 60.3\%$, $CO_2 = 38.2\%$, N_2 & $O_2 = 1.5\%$, $H_2S = 1984$ ppm. Figure 5-1 summarizes the methane content of landfill gas extracted from various types of landfills and current available energy recovery technologies.

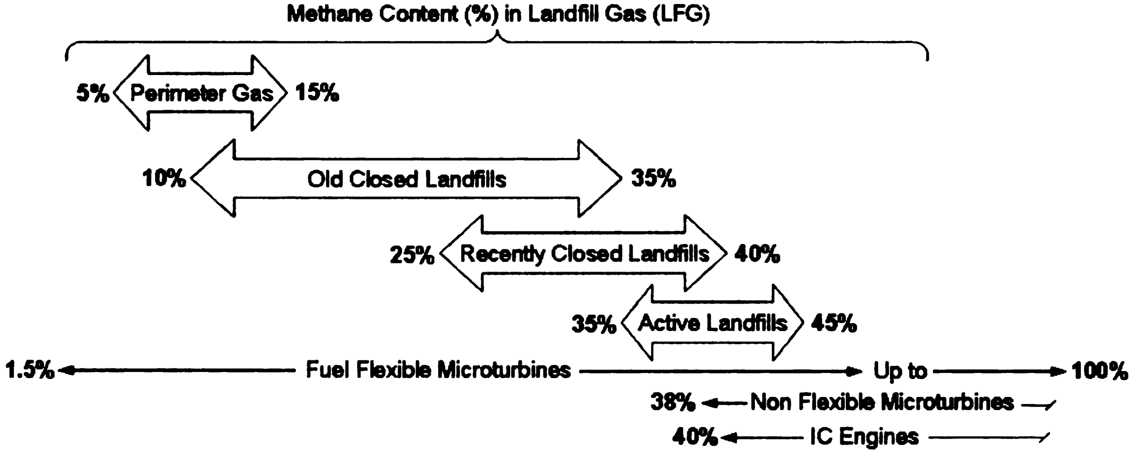

Figure 5-1. Landfill gas characterization by methane content (%) and technologies gas operating ranges.

Biogas composition strongly affects the thermo-chemical properties of the fuel/air mixtures (as will be discussed in the following chapters of this thesis). For instance, inert[*] gases like N_2, CO_2 and steam reduce the lower heating value (LHV) of the fuel. Biogas in general has a small to medium LHV. Figure 5-2 adapted from [81], shows LHVs of some alternative gas turbine fuels. The LHV of the waste methanization biogas (averaging at about 20,000 kJ/m^3) is less than natural gas and slow pyrolysis biogas (producer gas) [81].

Corrosive impurities and small LHVs, compared to natural gas, make biogas unsuitable to be compressed or injected into a pipeline system without prior cleaning and upgrading. As a result, for many biogas applications, cleaning and upgrading are required; **Cleaning** foremost implies the separation of water, hydrogen sulphide, and particles. **Upgrading** means removal of CO_2 to raise the LHV of the fuel [82]. After a

---

[*] It will be discussed later that these so called inert gases participate in the reactions to some extent.

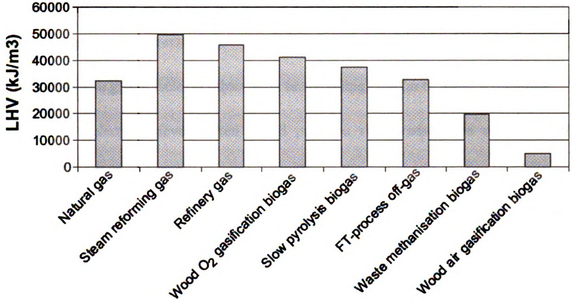

Figure 5-2. LHV's of alternative gaseous fuels compared to natural gas adopted from [81].

considerable amount of cleaning/upgrading, biogas (sometimes called biomethane) can be used in any application that consumes methane as a fuel [82].

It is of great interest to utilize biogas-driven gas turbines close to biogas production plants, which produce their own biogas fuel. Constraints on gas turbine efficiency, operability, and emissions should be met with as minimal biogas cleaning/upgrading as possible. This objective has been limited by some technical and economic obstacles. According to Sannaa [83], the construction of digesters and the transportation of biomass (especially for large-scale biogas plants) are costly. The upgrading is associated with high compression powers (in most upgrading methods). According to Wellinger and Lindberg [77], at present four different methods are used commercially for removal of carbon dioxide from biogas (upgrading) either to reach vehicle fuel standard or to reach natural gas quality for injection to the natural gas grid. These methods are:

1) Water absorption or scrubbing (with associated compression to about 10 bar and pumping),
2) Polyethylene glycol (selexol) absorption or scrubbing (similar to water scrubbing),
3) Carbon molecular sieves (often called pressure swing adsorption or PSA with compression up to 6 bar),
4) Membrane separation (includes high pressure gas separation with compressions up to 36 bar). Gas-liquid absorption membranes [77] developed recently for biogas upgrading work at atmospheric pressures.

5.1.2. Biogas benefits

The biogas possesses three general benefits: i) fossil fuel displacement; ii) economic development; iii) environmental.

Renewable bio-based fuels such as biogas will reduce the society's dependence on non-renewable resources such as coal, petroleum, and fossil fuel-derived natural gas. Biogas has been used for applications including heating, lighting and power generation. Among biofuels the benefits of biogas are similar to those of natural gas: increased energy security and improved public health and environment through reduced emissions [76].

Treatment of organic waste is an "environmentally-friendly" way to produce biofuels. The stabilized solid residue can be used as a soil conditioner material (compost), a nutrient-rich liquid fertilizer, or as fodder. The growth of the dairy industry has been limited as a result of difficulties to manage the livestock manure. Biogas facilities provide more flexibility in manure disposal, lowering the need for commercial fertilizer, and lowering odor [83]. A study in Denmark [83] has shown that conversion of animal waste to biogas will provide added value to manure as an energy resource and reduce environmental problems associated with untreated animal wastes. Biogas production also creates jobs and benefits the rural economy.

Burning biogas is a means for reducing greenhouse gas (GHG) emissions. It will be elaborated in Chapter 7 that burning biogas reduces the net CO_2 release and prevents CH_4 release to the atmosphere (CH_4 is a much stronger greenhouse gas than CO_2). Thus, it is also a means to satisfy various national and international ecological constraints such as the Kyoto protocol. As an example, Gerin et al. [84] showed that there is a *net reduction* in CO_2 and a *net production* of renewable energy as compared to fossil fuels, when maize and grass are used as the energy crops to feed anaerobic digesters. Borjesson and Berglund [85] analyzed fuel-cycle emissions of CO_2, CO, nitrogen oxides (NO_x), sulphur dioxide (SO_2), hydrocarbons (HC), CH_4, and particles from a life-cycle perspective for different biogas systems based on different digestion technologies and six different raw materials. Borjesson and Berglund [85] suggest that the *overall* environmental impact of biogas systems depends largely on the status of uncontrolled losses of CH_4, the end-use technology that is used, the raw material digested, and the energy efficiency in the biogas production chain. Combustion of biogas can reduce the flame temperature, which will reduce NO_x emissions because the thermal NO mechanism (at combustion temperatures roughly above 1800 K) is the main pathway of NO_x formation [86]. Conversion of animal waste to biogas reduces water pollution by using feedstock that would end up in rivers and lakes and reduces pollution of ground water as well [83]. For landfills, it reduces the cost of complying with U.S. Environmental Protection Agency landfill gas combustion requirements and reduces the amount of material that must be landfilled [87].

5.2. Global utilization of biogas

A study group commissioned by the German government shows a potential of up to 35% of total energy consumption by Germany of biofuels by 2030 [88]. At the end of 2006 about 3500 biogas plants with a total capacity of 1100 MW have been operating in Germany. Energy crops are the main substrate: manure has less than approximately 50 % share. In 2006, cultivation of non-food crops in Germany was 13.2% of German arable land [89]. Denmark is also one of the most advanced countries in biogas technology. Biogas plants in Denmark were well developed until 1998, but their expansion was slowed down afterward [83].

Sweden is presently a leading nation in biogas research and uses it for both *transportation* (trains, garbage trucks, automobiles) and *power generation*. In the last five years, Sweden has focused on biogas and bio-ethanol development [88]. Biogas can be used as a fuel in vehicles specially adapted to methane gas. According to Persson, [82] biogas has been used in Sweden as a vehicle fuel in large scale systems for buses and other vehicles since 1996. Before using biogas as a vehicle fuel, cleaning and upgrading of the gas is needed to avoid corrosion and mechanical wear, and to meet quality requirements of gas applications. The requirement for CH_4 content is 97±2 vol. %. In 2007, there were over 30 upgrading plants in operation or in the construction phase in Sweden, and during 2006, 54 % of the gas delivered to vehicles was biogas [82]. Biogas as vehicle fuel is given more and more interest worldwide and last year both Germany and Austria set up national targets of 20 % biogas in the fuel sold to vehicles [82]. Most of the above technologies need to convert biogas to a quality suitable for either vehicles or pipeline distribution, which imposes tight standards of upgrading/cleaning at least to a conventional natural gas quality.

In some European countries, government incentives (subsidies) support the biogas industry, which may not be economically feasible for other countries. There is a lack of comprehensive datasets in the literature demonstrating how much cleaning and upgrading is required for power generation by gas turbines in an economically, environmentally viable manner. The following sections address the latest status of technology and research relevant to burning biogas as an alternative gas turbine fuel.

5.3. Biogas potential as an alternative gas turbine fuel

5.3.1. Fuel-flexible gas turbines utilizing biogas

Worldwide demands for low emission and fuel flexible gas turbines are increasing. Gokalp et al. [81] report the preliminary progress of the major European project AFTUR (Alternative fuels for industrial gas turbines), begun in February 2003, in the selection and characterization of potential liquid and gas, alternative fuels for industrial gas turbines. However, their report is limited to the LHVs and C/H ratios for gaseous alternative fuels including biogas. Moliere [90] provided comprehensive information as well as an essential technical description of alternative gas turbine fuels ranging from volatile fuels, weak gas fuels extracted from the coal/iron industry, ash-forming oils, hydrogen-rich byproducts from refineries or petrochemical plants, liquid biofuel (e.g., ethanol), and biogas.

Studies are needed to assist governmental and private agencies in determining the types and characteristics of combustors most suitable for biogas power generation. For example, for the California Energy Commission, using a computer code developed for simple-cycle gas turbines, Yomogida et al. [91, 92] estimated that the thermal efficiency of a 125 kW Solar gas turbine (Titan© series) for biogas power generation is about 14%. They conducted a sensitivity analysis of the operating conditions and design parameters with the greatest influence on thermal efficiency. Some studies have focused on performance analysis and technological assessment of industrial gas turbines utilizing small LHV fuels. Palmer and Erbes [93] suggested a modeling approach and simulated a GE PG6541B gas turbine for both natural gas and low-BTU biogas fuel. Hanagudu, [94] in a more general study, reviewed the advantages, technical considerations and applications of biogas-fired industrial gas turbines with focus on the improvement of the electricity cogeneration for Indian cane sugar distilleries with mandatory treatment units. The biogas obtained was traditionally fired in boilers to generate steam.

5.3.2. Biogas-driven micro-gas-turbines (MGT)

Some current Micro-CHP (Combined Heat and Power or Cogeneration) installations use micro-gas-turbines (MGT) technology, which can be powered with different fuels and will provide on-site power and thermal energy with low emissions and low maintenance requirements. Some studies have focused on the use of biogas-driven micro-gas-turbines (MGTs) because biogas fuel applications may represent the best market for microturbines. At some facilities such as large dairy, sewage or wastewater treatment plants, the use of anaerobic digesters and microturbine cogeneration systems provides opportunities for reduction of both waste/manure treatment and energy usage.

In the U.S., the first microturbine tested on a biogas was a Capstone 30 kW unit at the Palmdale wastewater treatment in Los Angles County [95]. MGTs require the biogas to be compressed to about 6 atm and require the compressed gas to be dried (i.e., no moisture) [95]. Krautkremer et al. [96] state that MGTs are able to cope with up to 70 ppm H2S, a value never attained in biogas. Waste heat available in the exhaust can be used, for example, in absorption chillers. Goldstein [97] mentions that Capstone Turbine Corporation's latest offering is the 65 kW microturbine that uses waste flare gases from landfills (landfill gas) or wastewater treatment plants to create renewable energy. At multiple sites, Capstone experienced siloxane induced turbine failures. As a result, Capstone has established a fuel specification that requires less than ~ 0.03 mgr/m^3 of siloxane [98]. Ingersoll Rand (IR) markets two microturbine units referred to as the MT70 series with a capacity of 70 kW of continuous on-site electrical power and the MT250 series with capacity of 250 kW. Ingersoll-Rand commissioned the construction of a fuel mixing facility to test these commercial MGTs while operating on diluted alternative fuels such as biogas. Dolak and Armstrong [99] provide an overview of this fuel mixing facility, its capabilities, and a discussion of diluted fuel compositions typically found in field applications. They demonstrate that pollutant emissions are closely tied to both the magnitude and the composition of diluents. Biogas production is high in the hot season, whereas the thermal energy demand is highest in the cold season. Naing et al. [100] investigated the performance of a MGT cogeneration system in cold regions and the applicability of such a system to a sewage treatment plant which produces biogas from anaerobic digestion. They examined biogas hydrate formation as a cost-effective biogas storage solution to adapt to the delay between peak energy supply and peak energy demand with simulations of integration into an existing cogeneration system. Bohn and Lepers [101] overviewed low-BTU fuels suitable for utilization in gas turbines and investigated biogas utilization for a model integrated microturbine plant. Using a combustion model based on a systematically reduced 6-step reaction mechanism, they analyzed the change of emissions of NOx and CO. They also investigated the effects of low-BTU fuels (as compared to natural gas) on gas turbine materials and gas turbine efficiency.

5.3.3. Premixed turbulent biogas combustion

Experimental and theoretical studies dealing with flame structure of turbulent lean premixed flames are mostly limited to specific fuel compositions and they cannot be transferred to gas turbine combustion with variable composition gases such as biogas.

Ultra-low emissions targets have been set for gas turbines with NOx emissions <5 ppm (@ 15% O_2). A recent technology that can be used for low-emissions biogas-driven gas turbines is the Low-Swirl Injector (LSI). Johnson et al. [102] investigated a new approach for low emissions gas turbines by modifying a typical production high swirl injector [103] for gas turbine combustors to operate in a novel low-swirl stabilization mode. This LSI was investigated using PIV at elevated combustion inlet temperatures ($230 < T_0 < 430$ °C) and pressures ($6 < P_0 < 15$ atm). It was reported that the LSI emits NOx levels about 60% lower than from the HSI with no effect on CO. According to Johnson et al. [102], the lack of a large dominant strong recirculation zone and the shorter residence time within the LSI may provide an explanation for the NOx reduction. Recently, Littlejohn and Cheng [104] continued the earlier work of Johnson et al. [102] to investigate the fuel effects for seven diluted and undiluted fuels including a 50%CH_4-50%CO_2 fuel (representing biogas). The LSI was shown to be capable of supporting stable hydrocarbon flames that emit <5 ppm NOx (@ 15% O_2) with CO well below acceptable limits. The LSI did not need to undergo significant alterations to operate with the different hydrocarbon fuels used in their study. It was demonstrated that NOx emissions of biogas are lower, and CO emissions are higher than methane and propane flames of the LSI with increasing φ.

Few fundamental studies (experimental and numerical) provide data for lean premixed turbulent biogas combustion in gas turbine combustors at typical conditions, e.g. temperature and equivalence ratio (φ) of inlet flow, and combustor pressure. Lafay et al. [86] , under the AFTUR [81] project, compared the stability combustion domains, flame structures and dynamics between CH_4/air flames and biogas/air flames in lean premixed combustion conditions of gas turbines. Their experiments were conducted with five gas compositions: CH_4, a biogas (issued from waste methanization) with $CH_4 = 61$, $CO_2 = 34$ and $N_2 = 5$ (vol. %), three CO_2 diluted-methane-air flames with 12, 20, and 30 % by volume of CO_2. For the same φ, the addition of CO_2 implied strong modification of the reaction zone location and the reaction intensity. In addition, the CO_2 showed a stabilizing effect on pressure fluctuations. It was found that the main parameter to predict the flame structure is the laminar flame speed which depends on both φ and biogas

composition [86]. For this reason, laminar flame speeds of some biogas mixtures are calculated in this thesis (see Chapter 6).

Plasma Assisted Combustion (PAC) and/or H_2 enrichment could allow burning in ultra lean conditions[105]. Leung et al. [106] showed that the stability of a biogas non-premixed jet flame is enhanced significantly by introducing 10 (vol. %) H_2 into the fuel stream. More investigations, especially on premixed flames, are needed to understand the PAC and H_2 enrichment effects.

Further experiments in large-scale gas turbines with real biogas fuels (extracted from various biogas plants) can provide quantitative suggestions to modify the biogas composition and the combustor design. Moreover, combustion instabilities should be investigated for a wider range of compositions for biogas.

5.4. Discussion: Biogas research objectives

Gaseous alternative fuels can be produced by a variety of techniques, but attention here has been focused on biogas originating from anaerobic digestion. The desirability of utilizing the biogas near its production site was discussed, including the alignment of such physically proximate uses with the favorable attributes of gas turbines. It is desirable to expand the flexibility of gas turbines to handle a fuel with impurities (e.g., H_2S, particles and siloxanes) and diluents (e.g., CO_2 and N_2). Biogas has been demonstrated as a viable, practical alternative fuel that is relatively commonly used in Germany and the Nordic/Scandinavian countries for transportation and also for stationary power generation. Cleaning and upgrading of biogas fuel is necessary for using it as a vehicle-grade fuel: despite this requirement, numerous plants are in operation and a significant fraction of North-European heavy-duty vehicles use biogas for vital transportation needs. Gas turbines, which are widely (and ideally, or optimally) used for stationary power generation, would seem to be a good candidate for the use of replacement (biogas) fuel. However, gas turbines can be fuel-sensitive and variations of relative percentages of constituent combustibles can alter performance characteristics negatively. For this reason, basic research is needed. One specific application occurs in what are called micro gas turbines (MGTs), for which some preliminary research has been conducted. Much of this research is empirical and non-systematic (i.e. trial-and-error): not many systematic studies of biogas fuel in MGTs have appeared. Applied research (consisting mainly of modifications to existing equipment) has been carried out but studies are few, possibly because modification of existing systems is expensive.

Technical research issues of practical concern include the production of soot, NOx, and green house gases and the possible influences of biogas CO_2 content on emissions and engine operation. These issues warrant the attentions of applied research (i.e., modify turbines and then test with various fuels). They also warrant the focus of basic research on fundamental combustion processes occurring in the combustors of such turbines. This study presently turns toward addressing the fundamental question of biogas combustion characteristics and chemical kinetics. The objective will be to compare and contrast various basic metrics of biogas combustion with those of established, commonly used fuels (e.g., natural gas). Both premixed and non-premixed configurations will be utilized for this study in the subsequent chapters. Non-premixed scenarios, although not common in the current stationary gas turbines, are of significance in some other devices burning blends of diluted hydrocarbons (e.g., biogas). Laminar counterflow flames are commonly used to study chemical kinetics and reaction sets when both chemistry and transport are important (as used in Part I).

Chapter 6 Chemical Kinetics Study of Simulated Biogas in Premixed Combustion

The goal in this chapter is to study chemical kinetics of diluted hydrocarbon blends with focus on fuel blends that represent a biogas. Diluted hydrocarbon blends may be found in biogas combustion diluted mostly by CO_2, exhaust gas recirculation (EGR) diluted by combustion products, [107] and SOFCs (solid oxide fuel cells) operating on biogas or diluted methane [108-110]. Other applications of the research on CO_2 dilution include CO_2 recovery in semi-closed gas turbines with recirculating CO_2 and topping combustors [111]. Some studies [112-114] show that CO_2 diluted oxy-fuel combustion for pulverized fuels facilitates CO_2 separation and eventual sequestration. Therefore, oxy-fuel combustion involves high proportions of CO_2. Also, the addition of CO_2 and H_2O through flue gas recirculation (FGR) reduces oxides of nitrogen [115].

6.1. Biogas as a diluted hydrocarbon blend

Biogas can be simulated as a diluted hydrocarbon blend assuming that H_2S and particles have been separated and it does not contain NH_3, H_2, O_2, and CO. For the understanding of the impact of fuel blends on combustor operability, traditional engineering design parameters such as heating value, the Wobbe Index*, and autoignition are ultimately insufficient [116]. The cumulative thermal, transport and chemical effects

---

* The Wobbe Index (*WI*) is the main indicator of the interchangeability of gaseous fuels such as natural gas. It is frequently defined in the specifications of gas supply and transport utilities. If *HHV* is the higher heating value, and *SG* is the specific gravity, the Wobbe Index, *WI*, is defined as $WI = HHV / \sqrt{SG}$. For example, the *WI* value for methane is 12,735 (kcal/m^3).

of the constituents combine to produce a completely different behavior in blends compared to individual constituents. Properties like ignition delay times may behave in a highly nonlinear manner as fuel mixtures change. It is important to gain more understanding of the relationship between fuel mixture composition and properties such as flame speed and ignition and chemical delay times.

In this chapter, fuel blends include diluted methane mixtures whose main constituents may include CH_4, CO_2, N_2, and H_2O (constituents similar to water saturated biogas from digestion without drying). The consequences of CO_2 addition to hydrocarbon fuels have been studied in both premixed and non-premixed configurations. Several studies have demonstrated that CO_2 is not inert and participates in reactions [117-125]. Studies in non-premixed configurations will be reported in the next chapter.

Liu et al. [120] have numerically investigated the chemical effects of CO_2 replacement of N_2 in air on the burning velocity of lean to stoichiometric CH_4/ $CO_2/O_2/N_2$ and $H_2/CO_2/O_2/N_2$ mixtures at 1 atm. They focused mostly on the chemical effects of the addition of CO_2 to CH_4 indicating that the addition of CO_2 to air or replacement of N_2 in air by CO_2 may affect the burning velocity through three mechanisms: 1) The variation of the transport and thermal properties of the mixture, 2) The possible direct chemical effect of CO_2, and 3) The enhanced radiation transfer by CO_2. The reaction $CO_2+H \leftrightarrow CO+OH$ was shown to be the most important reaction associated with the direct chemical participation of CO_2 in these premixed flames. Hermann et al. [126] investigated the effect of four diluents (H_2O, CO_2, N_2 or Ar) on the

NOx formation rate in premixed laminar natural gas and hydrogen flames. They addressed that, in certain conditions, the rate of formation of NO is reduced by the addition of any diluents at constant combustion temperature.

In this chapter, some detailed and reduced mechanisms are explained, compared, and evaluated (e.g., GRI-Mech 3.0 and San Diego detailed mechanisms as well as GRI-Mech 1.2 reduced mechanism) in regard to their applicability for a biogas chemical kinetics study. For the evaluation of reaction mechanisms before their utilization in 2-D or 3-D CFD modeling or to find laminar flame speeds and ignition delays, a counterflow diffusion flame configuration, which is a fluid-dynamically simple and tractable 1-D configuration, is chosen. Gas phase equilibrium calculations are then performed to find adiabatic flame temperatures of biogas flames with variable compositions. Ignition delay times and laminar flame speeds are also calculated. Moreover, this study provides correlations to predict the behavior of individual diluents in biogas.

6.2. Gas phase chemical kinetics mechanisms

6.2.1. Standard-state thermodynamic properties in CHEMKIN

The molar heat capacity at constant pressure for species k is defined using arbitrary-order polynomial fits,

$$\frac{C_{pk}^{\circ}}{R} = \sum_{m=1}^{M} a_{mk} T_k^{(m-1)} \tag{6-1}$$

The superscript ^{o} refers to the standard-state, which is an ideal gas at 1 atmosphere for gas-phase species. The standard state molar enthalpy and entropy can be obtained from following equations:

$$H_k^{\circ} = \int_0^{T_K} C_{pk}^{\circ} dT + H_k^{\circ}(0) \quad S_k^{\circ} = \int_{298}^{T_K} \frac{C_{pk}^{\circ}}{T} dT + S_k^{\circ}(0) \qquad \text{6-2)}$$

The CHEMKIN Gas-Phase Kinetics package is designed by default to work with thermodynamic data in the form used in the NASA chemical equilibrium code [127]. In this case, seven coefficients, $a_{1\text{-}7}$, are needed for each of two temperature ranges. These fits take the form in equations (6-3) to (6-5), where the temperatures are in Kelvin.

$$\frac{C_{pk}^{\circ}}{R} = a_{1k} + a_{2k}T_k + a_{3k}T_k^{\ 2} + a_{4k}T_k^{\ 3} + a_{5k}T_k^{\ 4} \qquad (6\text{-}3)$$

$$\frac{H_k^{\circ}}{RT_k} = a_{1k} + \frac{a_{2k}}{2}T_k + \frac{a_{3k}}{3}T_k^{\ 2} + \frac{a_{4k}}{4}T_k^{\ 3} + \frac{a_{5k}}{5}T_k^{\ 4} + \frac{a_{6k}}{T_k} \qquad (6\text{-}4)$$

$$\frac{S_k^{\circ}}{R} = a_{1k} \ln T_k + a_{2k}T_k + \frac{a_{3k}}{2}T_k^{\ 2} + \frac{a_{4k}}{3}T_k^{\ 3} + \frac{a_{5k}}{4}T_k^{\ 4} + a_{7k} \qquad (6\text{-}5)$$

Accounting for the appropriate pressure and entropy-of-mixing terms, the entropy is

$$S_k = S_k^{\circ} - R\ln X_k - R\ln(P/P_{atm}) \qquad (6\text{-}6)$$

Thus, mixture-averaged entropy, Gibb's and Helmholtz free energies are found. The mixture-averaged entropy is

$$\bar{S} = \sum_{k=1}^{K} (S_k^{\circ} - R \ln X_k - R \ln(P/P_{atm})) X_k \qquad (6\text{-}7)$$

The therm.dat file provided with CHEMKIN version 4.1 includes seven coefficients for each of two temperature ranges and has 778 species.

6.2.2. Detailed, reduced and skeletal reaction mechanisms

Some well-examined methane (or natural gas) reaction mechanisms that can be utilized for biogas flames are introduced in this Section.

1- GRI-Mech 3.0 mechanism

GRI-Mech 3.0* (which replaced versions 1.1, 1.2 and 2.11) from the Gas Research Institute (GRI) is a compilation of 325 elementary chemical reactions and associated rate coefficient expressions and thermochemical parameters for the 53 species involved. It differs from the previous release in that kinetics and target data have been updated, improved, and expanded. Propane† and C2 oxidation products have been added and new formaldehyde and NO formation and reburn targets included [128]. It has nitrogen chemistry with 106 reactions belong to the nitrogen chemistry part.

---

[*] The Gas Research Institute discontinued its support of the GRI-Mech project in February 2000 after which no further development continued.

[†] 4 species have been added to 49 species of GRI-Mech 2.11. Acetaldehyde (CH_3CHO) and vinoxy (CH_2CHO) chemistry are included to better describe ethylene oxidation, and this path is included among the $O_x + C_2H_y$ reaction products. C_3H_7 and C_3H_8 also added as well as a minimal set of propane kinetics to model propane, as a minor constituent only.

GRI-Mech 3.0 has been optimized for methane and natural gas as fuel and includes NO formation and reburn chemistry. Reactions that are involved in the combustion of other hydrocarbon constituents of natural gas (e.g., ethane and propane) are also included. However, since the optimization did not include targets relevant to other fuels, GRI-Mech should not be used to model combustion of pure methanol, propane, ethylene, and acetylene, even though these compounds are on the GRI-Mech species list [128].

The conditions for which GRI-Mech 3.0 has been optimized, limited primarily by the availability of reliable optimization targets, are roughly 1000 to 2500 K, 10 Torr to 10 atm, and equivalence ratio from 0.1 to 5 for premixed systems [128]. In this work, GRI-Mech 3.0 is used inside its optimization and validation ranges. The soot formation for natural gas is not described by GRI-Mech 3.0 as so the chemistry involved in selective non-catalytic reduction of NO, which may be important in natural gas reburning at lower temperatures. Thermodynamic data is provided from GRI-Mech 3.0 Thermodynamics released 7/30/99 based on NASA Polynomial format for CHEMKIN-II.

2- San Diego (SD) detailed mechanism

The San Diego mechanism [129] (Release 2005/12/01)* provides a detailed chemistry to focus on conditions relevant to flames, high temperature ignition and in the case of supersonic combustion, detonations. It is composed of 6 elements including N, H, O, C, Ar and He, 46 species, and 235 reactions. Helium is an addition to the GRI-Mech 3.0 mechanism, which includes only the first 5 elements. Pressure dependent reactions

---

* In the latest version of the San Diego Mechanism (released 2005/12/01), reactions related to combustion of ethanol were added to the existing San Diego Mechanism. Most of those reactions were adopted from the Ph.D. thesis of Juan Li [130]. Thermodynamic and transport data for the additional species associated with ethanol have also been added.

are described by the TROE formulation [131]. All reactions except one ($CH_3O+O_2 \rightarrow CH_2O+HO_2$) are reversible and their backward rates can be calculated from the forward rate and the thermodynamic data.

The San Diego mechanism does not include nitrogen chemistry and NOx formation. However, the group offers a NOx mechanism (Release 2004/12/09) to enable researchers to model NOx in flames. This nitrogen chemistry is based on the previous work by Hewson and Bollig [132]; however, this mechanism has not yet been evaluated thoroughly. One reaction ($HCCO+NO \leftrightarrow HNCO+CO$) has been added based on the GRI 2.11 rates [133]. In the revision of March 2005, the pre-exponential in this reaction has been revised based on the evaluation by the San Diego Group. This value has been modified from 2.35E+13 to 2.00E+13 [(mol/cm^3)-1/s].

Uncertainties in rate parameters of many steps can increase the uncertainties in the predictions when large numbers of steps are included. Also, it has been understood from experience that the rate parameters of a relatively small number of elementary steps are of crucial importance to the predictions. Figure 6-1 shows a distribution of scaled reaction rates for the 235 reactions of the San Diego mechanism at stoichiometric methane/air adiabatic flame temperature (T_{ad}=2224 K). To scale values at T, each reaction rate is divided by the maximum reaction rate at T (RRmax) and then multiplied by *e*. An investigation of this figure renders that only 7 reactions are in the range of (5% RR_{max} - RR_{max}) and only 23 reactions are in the range of (2% RR_{max} - RR_{max}). In a sense, these reactions represent the global thermo-chemical behavior of the flame. Cumulative effects of small contributions from a large number of steps are seldom of much significance (also seen in Figure 6-1). Therefore, if the numbers of species and reactions are kept as much as possible to the minimum needed to describe the systems, uncertainties in the rate parameters employed are minimized. This statement characterizes the philosophy underlying the San Diego mechanism. It differs from a number of other data bases, many of which seek completeness, attempting to include all potentially relevant elementary steps [129].

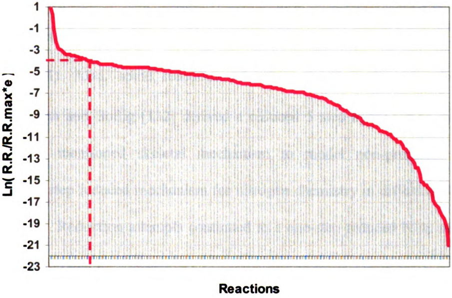

Figure 6-1. Distribution of the scaled reaction rates for San Diego mechanism reactions at T_{ad} of stoichiometric methane/air mixture (T_{ad}= 2224 K).

3- Reduced GRI-Mech methane mechanism

A reduced mechanism [134] which includes 19 species (+N_2 and Ar) and 84 reactions (released 1994) is also used*. This mechanism has been reduced from GRI-

---

* This mechanism can also be considered a skeletal mechanism with respect to very smaller reduced mechanisms.

Mech 1.2 by the group who developed GRI-Mech mechanism. This mechanism, however, does not include nitrogen chemistry (the detailed GRI-Mech 1.2 mechanism did not include a nitrogen chemistry).

4- San Diego skeletal and reduced mechanisms including NOx Chemistry

San Diego group offers a skeletal mechanism describing hydrocarbon and nitrogen chemistry, which includes 65 steps for the C1 and C2 hydrocarbon chemistry plus 55 steps for the nitrogen chemistry. This mechanism has been derived for *non-premixed* combustion. Some reactions relevant to premixed burning have been left out (i.e. $CH_4+O=CH_3+OH$). Also, some reactions related to ignition chemistry have been neglected. Hewson and Bollig [132] derived a reduced 5 step hydrocarbon mechanism from the above mentioned skeletal mechanism to model non-premixed methane combustion. A 6 step reduced mechanism for nitrogen chemistry in diffusion flames has also been offered. Reduction attempts continued to a one-step reduced NOx mechanism which is $N_2 + O_2 \rightarrow 2\,NO$.

6.3. Evaluation of reaction mechanisms

In this section, a counterflow diffusion flame with methane as fuel is modeled and compared to a benchmark to evaluate and compare the reaction sets. The flame structure study of Sung et al. [135] at Princeton is the benchmark for comparison. In the next step, after validation of both the computational model and the reaction set, this flame system will be employed to study simulated biogas mixtures.

The CHEMKIN based numerical code OPPDIF [136], originally developed by Kee et al. [137] for premixed opposed-flow flames, is employed. The governing equations are found in Kee et al. [137]. Radiative heat loss is not considered. The transport and thermochemical properties are obtained from the CHEMKIN database [125].

Fuel enters from the origin of the coordinate system. Calculations are performed with one atmosphere pressure and 300 K upstream temperatures. The burner separation, L, is 13 mm. A plug flow boundary condition is selected for this study (Sung et al. [135] demonstrate that despite the differences in the plug flow or potential flow boundary conditions, velocity and temperature fields are identical within the thermal mixing layer). Two computational cases of interest have velocities of $V_F=V_O=45$ cm/s and $V_F=V_O=25.5$ cm/s, which correspond to strain rates of $a=56\ s^{-1}$ and $a=42\ s^{-1}$, respectively. The stoichiometric mixture fraction, z_f, for these flames is 0.3. The fuel and oxidizer streams

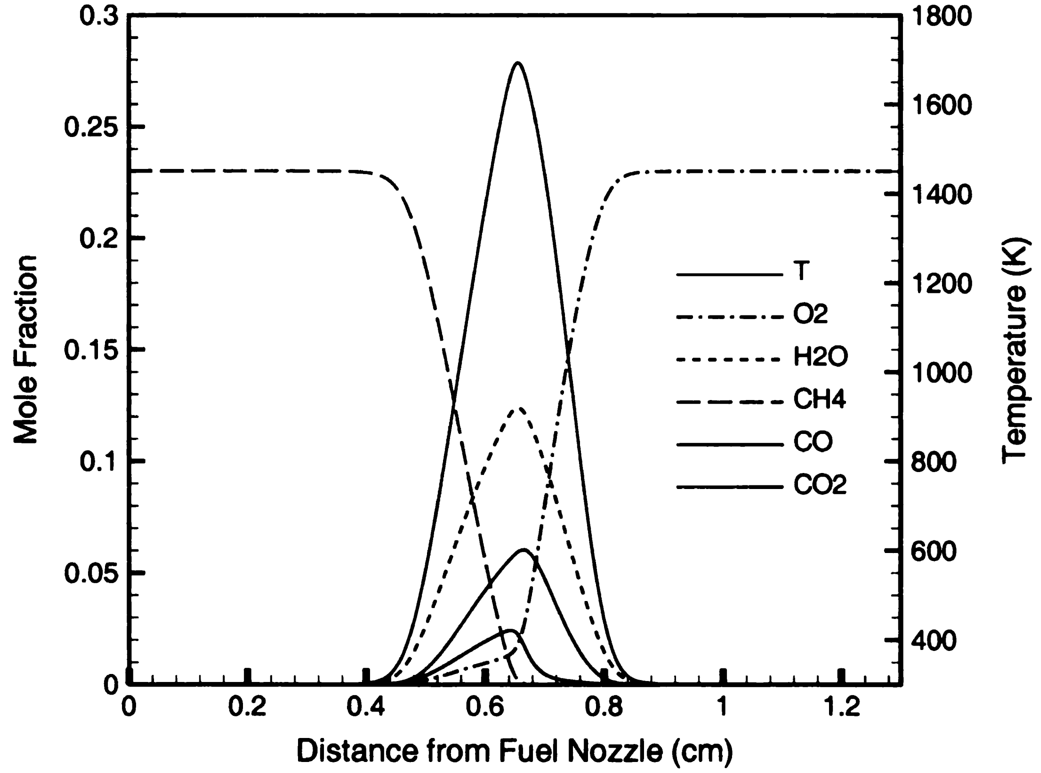

Figure 6-2. Temperature and major species profiles for $(23\%CH_4-77\%N_2)$/Air flame at 1 atm, $a=56\ s^{-1}$ (GRI-Mech 3.0 mechanism).

consisted of 23% methane in nitrogen and 23% oxygen in nitrogen, respectively, both by volume. Figure 6-2 plots the temperature and major species profiles when the GRI-Mech 3.0 mechanism is used.

Figure 6-3 presents a comparison of two computed temperature profiles corresponding to two strain rates case a) a=56 s^{-1} and case b) a=42 s^{-1} (two inlet velocities) and the experimental data for a=56 s^{-1} [135]. The full width at half maximum (FWHM) criterion is used for the flame thickness, δ. The flame thickness is approximately 0.21 cm for case a (higher strain rate) and 0.29 cm for case b. Temperature profiles become narrower when the strain rate is increased.

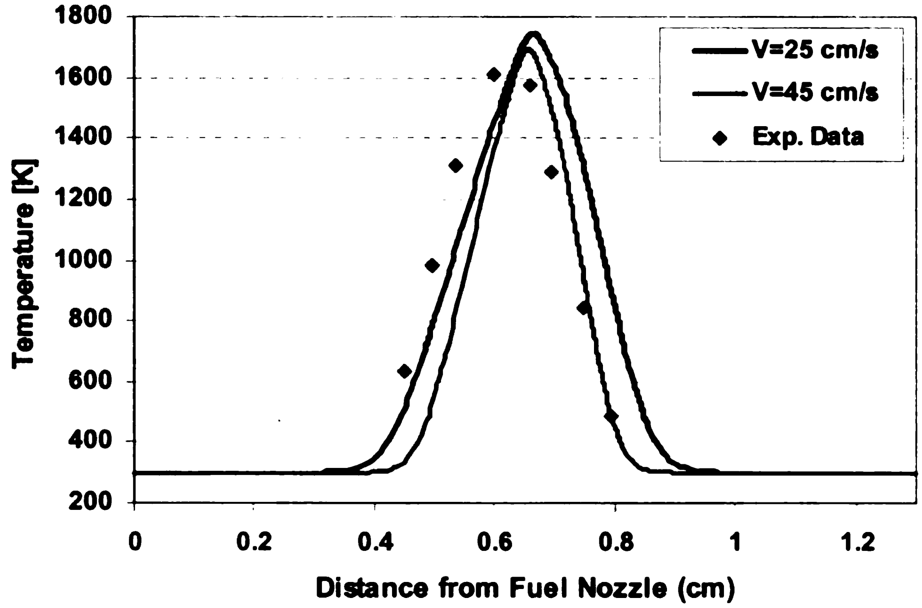

Figure 6-3. Computed temperature profiles for ($23\%CH_4$-$77\%N_2$)/Air flame at 1 atm, with GRI-Mech 3.0 mechanism: a) V_F=V_O=45 cm/s (line, computed), b) V_F=V_O=25.5 cm/s (line, computed) and c) V_F=V_O=45 cm/s (solid squares, experiments of Sung et al. [135])

Comparison of the temperature and major species profiles with those of experimental and computational study of Sung et al. [135] shows a good agreement in the oxidizer side and very good agreement in peak points. A slight offset from the experimental data points is observed in the fuel side. According to Sung et al. [135], the characteristic flame thickness should scale with $\sqrt{a}$, that is $\delta \times \sqrt{a} = Const$. An order of 15% deviation is found for this correlation based on the calculated values from Figure 6-3. These slight deviations may have two reasons:

1) Uncertainty of the velocities in the experiments leading to slight mismatching of strain rates between the benchmark and computations.

2) The effect of the underlying chemistry and reaction mechanism.

The Princeton group used a C_2 scheme consisting of 29 species and 152 elementary reactions [135]. The effect of reaction mechanism selection on the offset in the fuel side is investigated by using the detailed San Diego as well as the reduced GRI-Mech 1.2 mechanisms. The San Diego mechanism produces similar profiles as the GRI-Mech 3.0 mechanism with negligible difference in major species, a slight shift in the temperature profile, and a small difference in temperature peak (ΔT_{max}~7 K, 0.4 %). As seen in Figure 6-4, the reduced mechanism shows the same behavior for the temperature (close values for T_{max}). A similar behavior is also observed for the major species (not shown here). However, Figure 6-5 (profiles of H radicals) shows that the reduced mechanism overpredicts the mole fraction of some important radicals. H radicals are chain branching radicals which affect flame speeds, which we intend to predict. Our goal in this chapter is lean premixed flame modeling. Thus, the San Diego skeletal mechanism, which includes

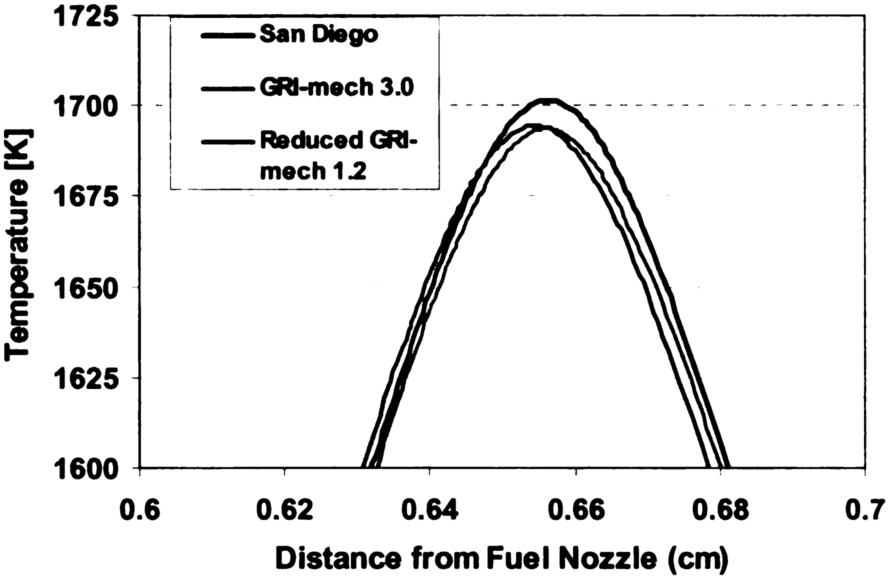

Figure 6-4. Comparison of computed profiles of temperature near the peak point for ($23\%CH_4$-$77\%N_2$)/Air flame at 1 atm (*a* =56 s^{-1}) with GRI-Mech 3.0, reduced GRI-Mech 1.2, and San Diego mechanisms.

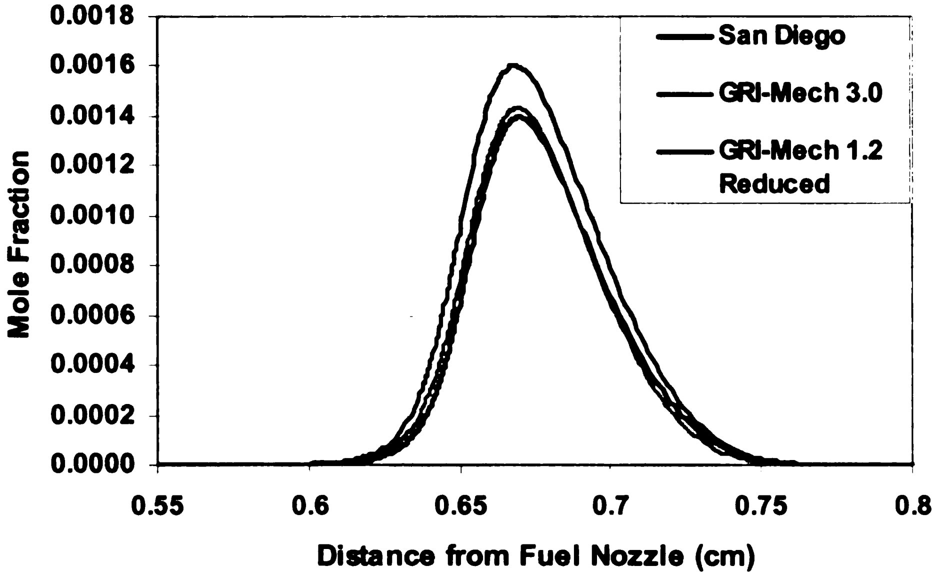

Figure 6-5. Comparison of computed profiles of H radicals near the peak point for ($23\%CH_4$-$77\%N_2$)/Air flame at 1 atm (*a* =56 s^{-1}) with GRI-Mech 3.0, reduced GRI-Mech 1.2, and San Diego mechanisms.

65 steps for the C_1 and C_2 chemistry plus 55 steps for the nitrogen chemistry, is not employed here because it has been derived for non-premixed combustion.

6.4. Carbone dioxide diluted methane/air counterflow flames

A configuration similar to the configuration in Section 6.3 is selected to study methane diluted counterflow flames. Only a case similar to case (a) above with V_F=V_O=45 cm/s at 1 atm pressure is considered, but, unlike the previous problem, fuel stream is not diluted with nitrogen and air containing 21% O_2 enters from the oxidizer side. Computations are performed for four fuel mixture compositions, mixtures 1 to 4 summarized in Table 6-1. GRI-Mech 3.0 kinetic mechanism is employed. Figure 6-6 illustrates profiles of temperature and major species for four compositions of simulated biogas flames (mixtures 1-4).

Figure 6-7 and Figure 6-8 show, respectively, profiles of H radical and CH_4 mole fractions for four compositions (mixtures 1-4) in the thermal mixing layer. Since the breakdown of CH_4 is mainly due to its attack by OH and H radicals [138], the peak values of OH and H occur on the oxidizer side of the flame. When the CO_2 proportion in the fuel stream increases, the peak of H reduces and the peak locations move toward the oxidizer side. This suggests that the mechanism with which CO_2 influences the flame structure is as follows: When CO_2 concentration rises respect to CH_4 concentration (from 20% to 50%, respectively), the competition of reactions like $CO_2+H \rightarrow CO+OH$ with the chain branching reactions like $H+O_2 \rightarrow H+OH$ reduces the concentrations of important radicals i.e. H, O, and OH present in the thermal mixing layer. When the total amount of these radicals is less, CH_4 is attacked less and can penetrate more towards the oxidizer side while consuming radicals and moving their peak locations. This shift in radical peaks is not significant as compared to the shift due to flame stoichiometry changes resulting from CO_2 dilution of the fuel stream.

Table 6-1. Selected compositions for simulated biogas used in the computational study.

Biogas mixture No.	Simulated biogas blend composition (Vol. %)
1	50% CH_4-50% CO_2
2*	60% CH_4-40% CO_2
3†	70% CH_4-30% CO_2
4	80% CH_4-20% CO_2
5	50% CH_4 + 16.6% CO_2 + 16.6% N_2 + 16.6%H_2O
6‡	61% CH_4 + 34% CO_2 +5 % N_2

It is of interest to conduct a scaling analysis for the diluted hydrocarbons, here methane. Due to the highly nonlinear behavior of species, this is a hurdle in the current study. Attempts are focused on CO_2 profiles based on the results of counterflow flame study. $[CO_2]$ is scaled by the $[CO_2]_F$, which is the molar concentration of the CO_2 in the

---

[*] This composition will be used in Chapter 6 as a typical for biogas from anaerobic digestion (AD) plants used in dairy industry without upgrading.

[†] Compositions in mixtures 3 and 4 represent biogas from AD plants or landfills with "partial" upgrading.

[‡] A typical biogas issued from waste methanization reported by Gokalp and Lebas [81] used also in the experiments of Lafay et al. on lean premixed turbulent biogas combustion at CNRS-LCSR, France [86]. This composition will be used in this chapter to examine equilibrium state, ignition delays, and laminar flame speeds.

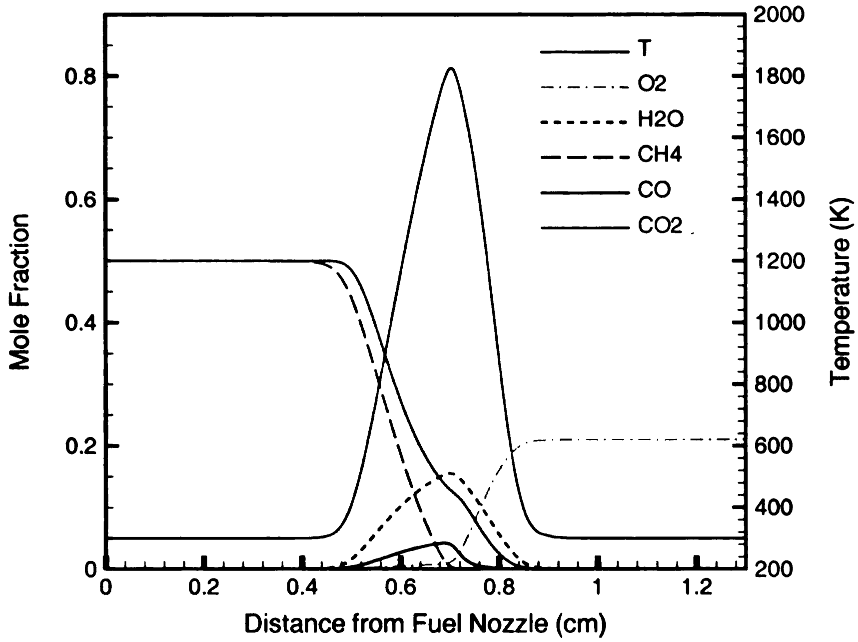

a) Fuel mixture #1: 50% CH_4-50% CO_2

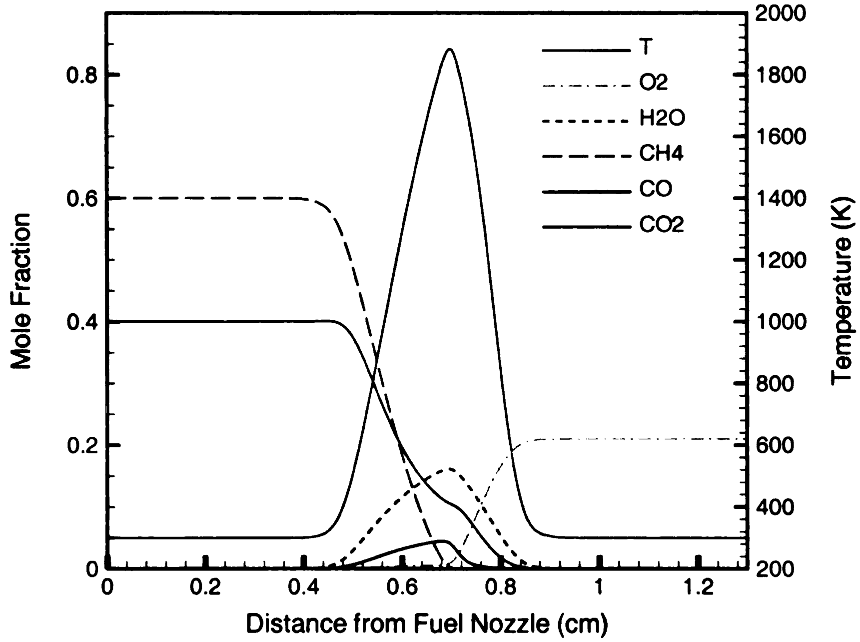

b) Fuel mixture #2: 60% CH_4-40% CO_2

Figure 6-6. Temperature and major species profiles for four compositions of CO_2 diluted methane flames (P=1 atm, V_F=V_O=45 cm/s, GRI-Mech 3.0 mechanism).

Figure 6-6 Cont'd

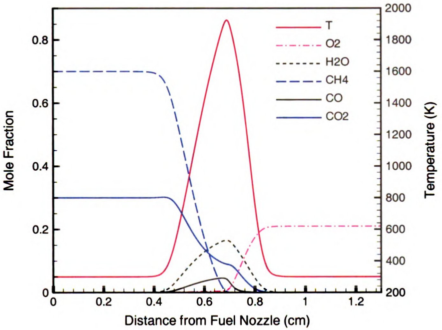

c) Fuel mixture #3: 70% CH_4-30% CO_2

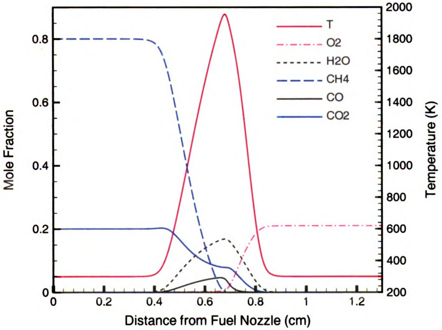

d) Fuel mixture #4: 80% CH_4-20% CO_2

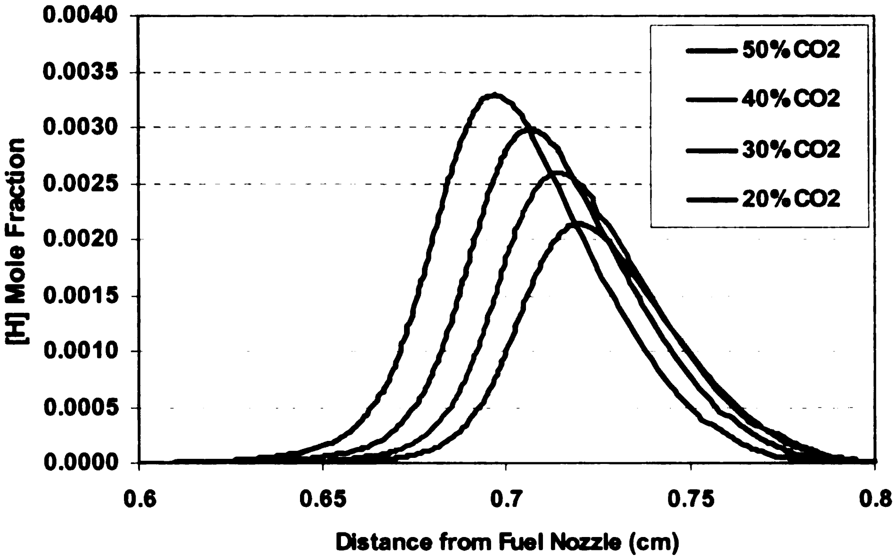

Figure 6-7. Profiles of H radical mole fractions for four compositions of CO_2 diluted methane flames in thermal mixing layer (P=1 atm, V_F=V_O=45 cm/s, GRI-Mech 3.0 mechanism).

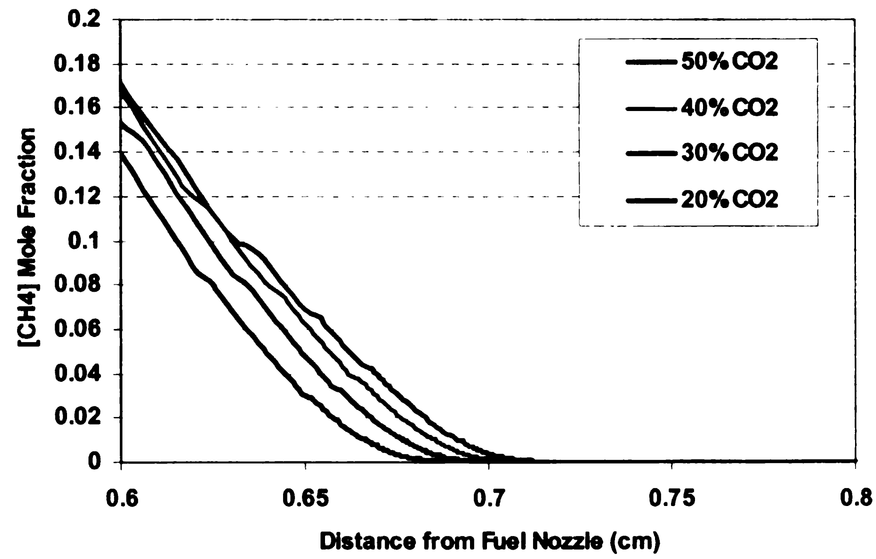

Figure 6-8. Profiles of CH_4 mole fraction for four compositions of CO_2 diluted methane flames in thermal mixing layer (P=1 atm, V_F=V_O=45 cm/s, GRI-Mech 3.0 mechanism).

fuel mixture (e.g. for the mixture of 60% CH_4-40% CO_2, $[CO_2]_F$=0.4). Figure 6-9 shows the profiles of scaled CO_2 for four compositions selected. Variations have a similar trend upstream of the thermal mixing layer, but trends are different within the mixing layer (x=0.6-0.75 cm).

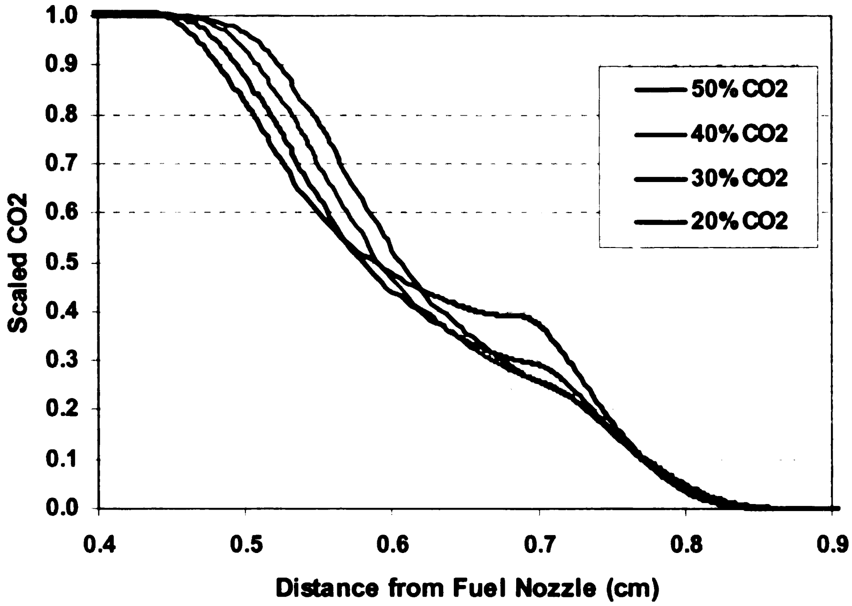

Figure 6-9. Profiles of scaled CO_2 for four compositions of CO_2 diluted methane flames in a counterflow configuration (P=1 atm, $V_F=V_O$=45 cm/s, GRI-Mech 3.0 mechanism).

6.5. Water vapor and nitrogen influences in biogas combustion

It is informative to investigate the relative contribution of diluents that can be present in a biogas i.e. CO_2, H_2O and N_2, on the flame temperature, NO emissions and important radicals. This investigation can guide to understand the alteration of biogas flame characteristics due to the presence of water vapor (or occasional N_2 content). For this study, the configuration in Section 6.4 is utilized with $V_F=V_O$=45 cm/s at 1 atm. The oxid

CH

N

(5

pre

con

F

oxidizer is air containing 21% O_2. Two biogas mixtures are compared: 1) A $CH_4/CO_2/N_2/H_2O$ mixture consisting of 50% CH_4 and equal proportions (16.6%) of CO_2, N_2, and H_2O (Vol. %) designated as biogas mixture 5 in Table 6-1; 2) biogas mixture 1 (50% CH_4-50% CO_2) that was modeled before. Both mixtures have the same CH_4 proportions. GRI-Mech 3.0 kinetic mechanism is employed. Figure 6-10 presents the computed temperature, major and minor species profiles for fuel mixture 5.

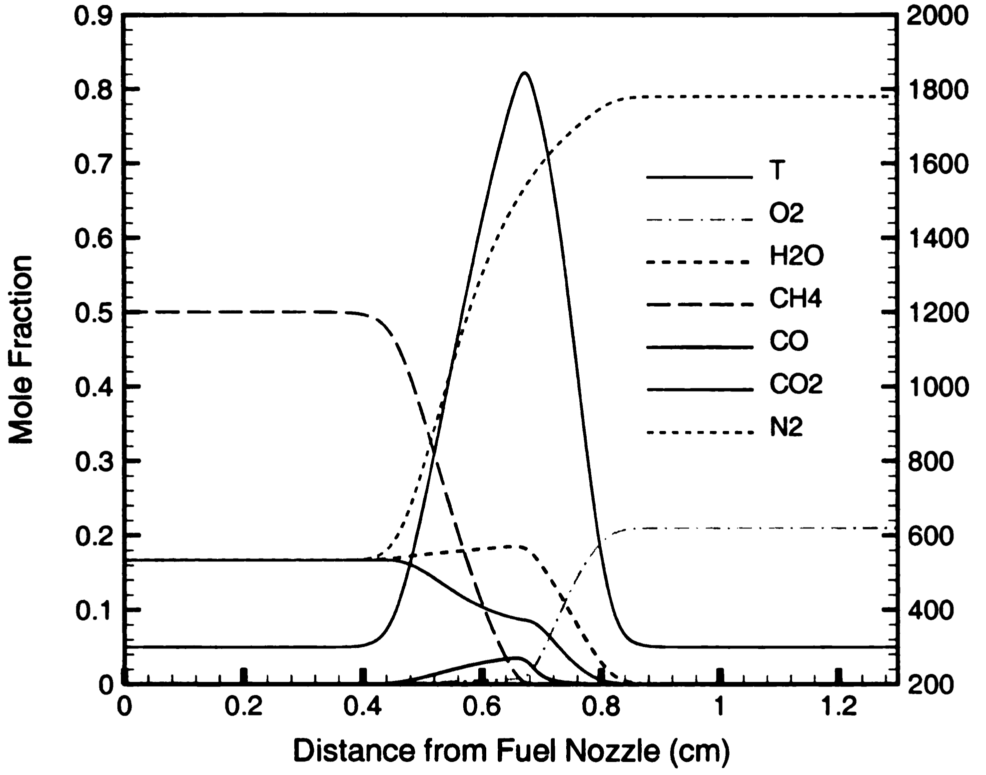

(a)

Figure 6-10. Temperature, major species profiles (a) and minor species profiles (b) for biogas mixture 5 (P=1 atm, $V_F=V_O=45$ cm/s, GRI-Mech 3.0 mechanism).

Figure 6-10 Cont'd

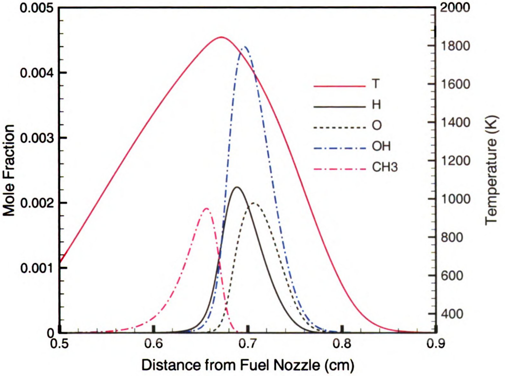

(b)

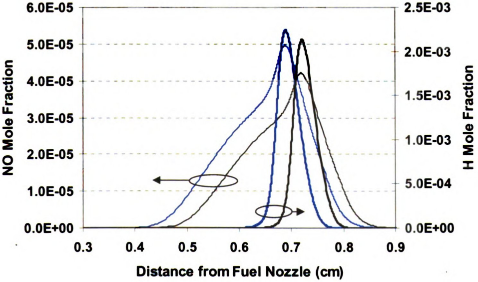

Figure 6-11. Comparison of NO and H radical mole fractions: biogas mixture 1 (black lines); biogas mixture 5 (blue lines).

Figure 6-11 shows a comparison of NO and H mole fractions between two biogas mixtures. For fuel mixture 1, T_{max}=1825 K and for fuel mixture 5, T_{max}=1844 K. The comparison in Figure 6-11 indicates that for a fixed hydrocarbon content (CH_4=50%), replacement of CO_2 by N_2 and H_2O increases the NO emissions and H radical concentrations. This suggests that, among these diluents, CO_2 is relatively stronger in the reduction of temperature, NO and H. The reduction of H leads to lower flame speeds in premixed scenarios. Thus, it is anticipated that the burning velocity of fuel mixture 5 is bigger.

6.6. Biogas premixed flames: Results and discussion

6.6.1. Equilibrium calculations for biogas/air combustion

Gas phase equilibrium calculations are conducted to find the adiabatic flame temperature and equilibrium species. GRI-Mech 3.0 reaction mechanism is employed. Initial conditions for the mixtures are T=298 K and P=1 atm similar to those usually reported in combustion literature. Two gaseous mixtures are compared: a) pure methane: CH_4=100%, and b) A typical biogas issued from waste methanization [81] with a composition CH_4=61%, CO_2=34%, N_2=5 % (Vol. %) which has been used in the work of Lafay et al. [86]. The later mixture was designated as biogas mixture #6 in Table 6-1. As illustrated in Figure 6-12, the adiabatic flame temperature of this typical biogas mixture is lower than methane in the whole lean to rich range of φ. This corroborates the statement made in the introduction of Part II.

Figure 6-13 presents profiles of H and OH radicals as well as emissions of NO and CO. For the lean conditions in methane and biogas combustion, CO is negligible while it rises significantly at rich conditions with more CO emissions from biogas. Methane produces more NO emissions than biogas (mixture 6) because the flame temperature that affects thermal-NO formation is higher in the methane flame. H and OH radicals, which are important in chain branching reactions, have also been compared. The abundance of both radicals is greater for pure methane. However, the difference is more pronounced for H radicals; i.e. the effects of diluents addition to methane can be relatively better understood via the tracking of H radicals as opposed to OH radicals.

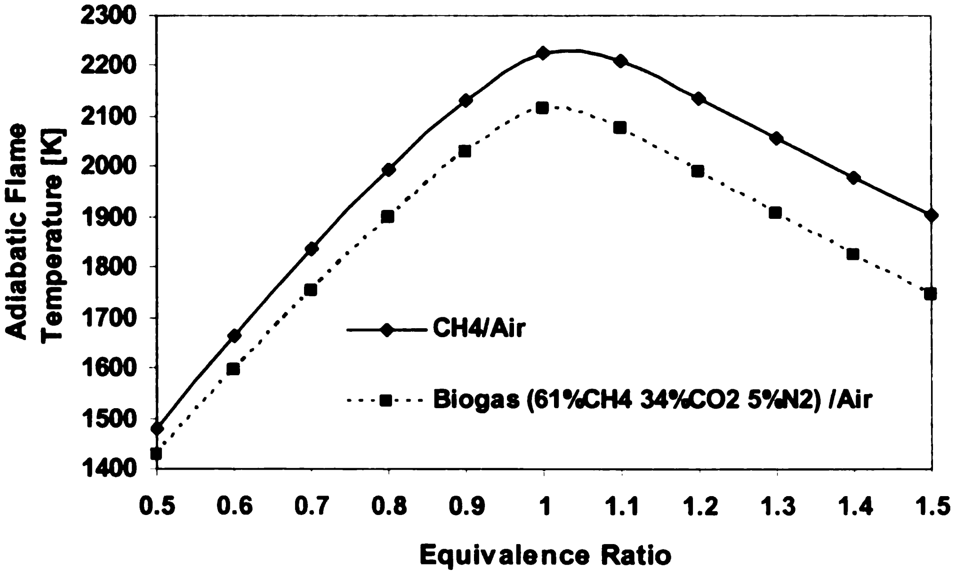

Figure 6-12. Adiabatic flame temperature of CH_4 and a typical biogas (mixture 6) in lean to rich equivalence ratios.

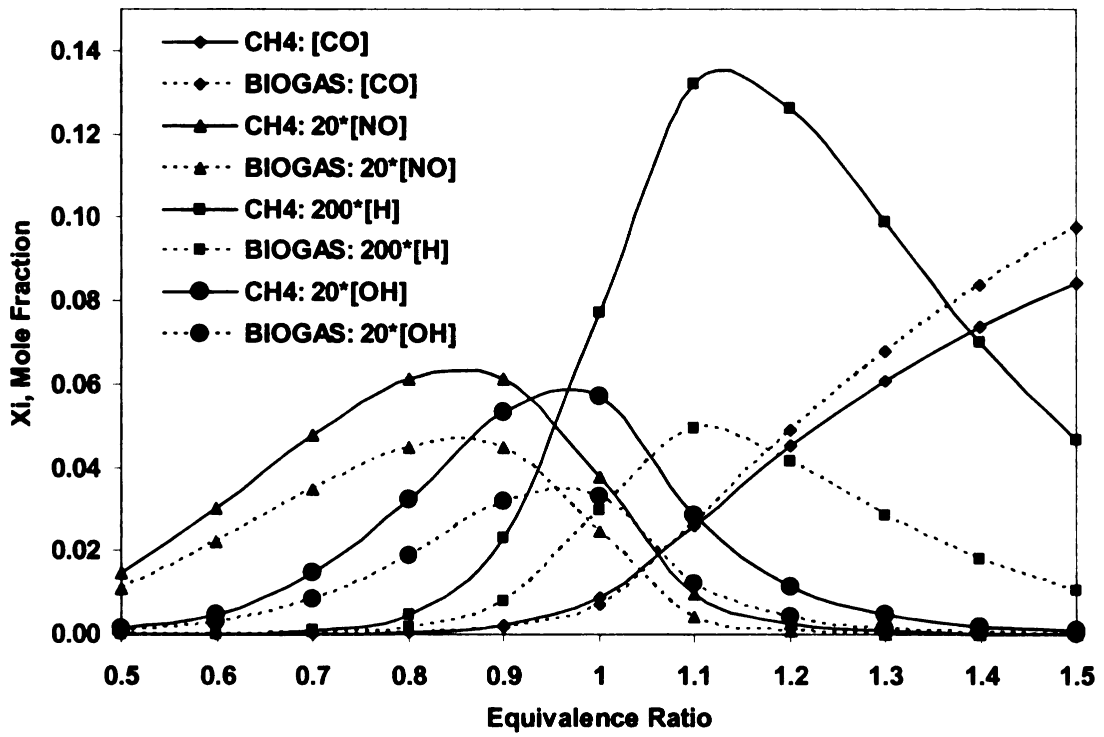

Figure 6-13. Equilibrium mole fractions of H, OH, NO and CO for CH_4 and a typical biogas (mixture 6) in lean to rich equivalence ratios.

6.6.2. Chemical kinetic modeling of biogas ignition

Gas turbine industry has been widely utilizing premixed combustion technology. Understanding the ignition process for gas turbines is vital because autoignition of fuel and oxidizer mixtures prior to reaching the main burner may enhance pollutant emissions and damage combustor components. Experimental techniques including constant-volume bombs, continuous flow devices, and shock tubes have been utilized to measure ignition delay times (t_{ig}). Comparison of computational predictions of ignition delay times to shock tube experiments (usually by using reflected shocks) is often used in the validation and testing procedure of detailed chemical kinetics mechanisms and provides an understanding of the underlying chemistry. For instance, Petrova and Williams [139] systematically applied the technique for propane, propene, allene, and propyne to test a small detailed chemical kinetics mechanism for hydrocarbon combustion.

Ignition delay characteristics of methane fuels have been comprehensively reviewed by Spadaccini and Colket [140]. In a fuel blend, variation of combustible constituents and diluents will change the ignition process. This is elucidated in an empirical correlation proposed for the ignition delay times of natural gas [140, 141]

$$t_{ig} = 1.77 \times 10^{-14} \exp(18693/T) \times [O_2]^{-1.05} [CH_4]^{0.66} [HC]^{-0.39}, \tag{6-8}$$

in which concentrations are expressed in mole/cm^3. [HC] represents the total molar concentration of all non-methane hydrocarbons (contaminants or additives including ethane, propane and n-butane) present in small levels in a natural gas blend. This correlation is valid for temperatures between 1300 and 2000 K, pressures from 3 atm to 15 atm and φ=0.43-1.25. The overall pressure dependence is $P^{-0.78}$.

To our knowledge, there is no empirical correlation for the ignition delay times of typical biogas blends extracted from landfills or digestion plants, which include high concentrations of diluents (e.g., 40-60% CO_2). Here, we examine a chemical kinetic model for ignition delay times of a simulated biogas blend: A typical biogas with a composition CH_4=61%, CO_2=34%, N_2=5 % (Vol. %) which was designated as biogas mixture #6 in Table 6-1. GRI-Mech 3.0 kinetics mechanism that has performed well in the prediction of the counterflow diffusion flame structure in this chapter and in the CH_4 oxidation modeling is employed.

The prediction of ignition delay times is performed using CHEMKIN based on one of these criteria: 1) A time based on the maximum of certain species concentrations (e.g., the peak of the OH or CH profile); 2) A specified rate of increase of temperature (e.g., the maximum of dT/dt). Ignition times are calculated for a closed homogeneous chamber (a 0-D problem free from transport effects) with uniform pressure. The energy equation is solved for specified initial pressures and temperatures. Here, two criteria are used for the ignition delay times

1) The inflection point in the temperature profile (max. dT/dt),

2) The maximum mole fraction of the OH radicals.

Therefore, for each initial condition two values are obtained. The temperature and OH profiles must be carefully investigated to realize the correct ignition times in case more than two values are obtained.

Although it is known that t_{ig} decreases for both increasing temperature and increasing pressure [140], the ignition behavior of biogas mixtures for varying pressures and temperatures should be carefully examined. The ignition delay times of biogas mixture 6 using the maximum OH radical criterion are delineated in Figure 6-14 when the mixture temperature is increased from 1000 K to 2000 K. Pressure is maintained at 1 atm and the fuel-to-air equivalence ratio is constant and equal to 1. Biogas ignition delay times are higher than methane (not shown here) i.e. biogas ignition is slower.

Table 6-2 (plotted also in Figure 6-15) summarizes peak gas temperatures and the ignition delay times (using both criteria introduced before) of biogas mixture 6 at different fuel-to-air equivalence ratios, φ, fixed atmospheric pressure and fixed initial

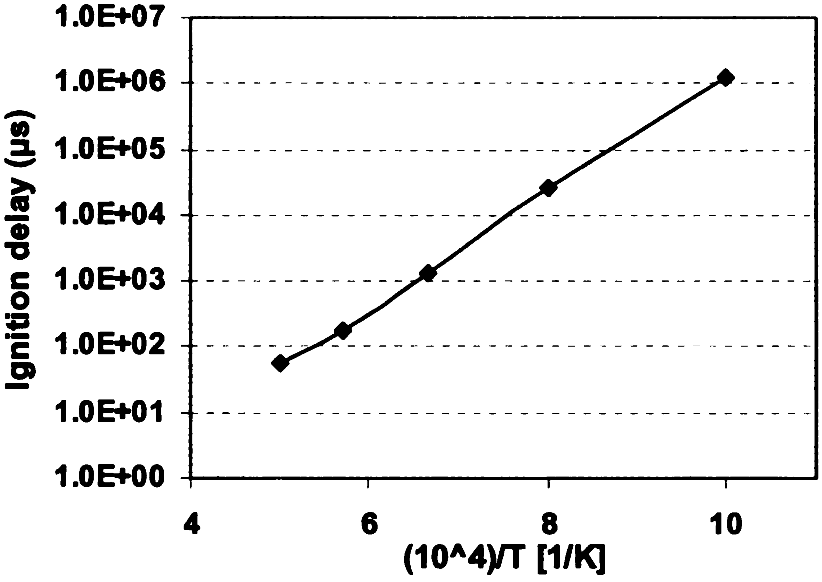

Figure 6-14. Ignition delay times of biogas mixture 6 at 1 atm and φ=1 (The peak of the OH profile criterion was employed).

Table 6-2. Ignition delay times of biogas mixture 6 for different equivalence ratios at 1 atm and 1000 K.

P=1 atm, $T_{initial}$=1000 K	Thermal ignition time [sec]		
φ	Temperature inflection point (max. dT/dt) criterion	Peak of the OH profile criterion	Peak gas temperature [K]
0.6	0.8863	0.8864	2153
0.7	0.9646	0.9647	2271
0.8	1.040	1.040	2362
0.9	1.114	1.114	2425
1	1.185	1.185	2462
1.1	1.256	1.256	2472
1.2	1.325	1.325	2453

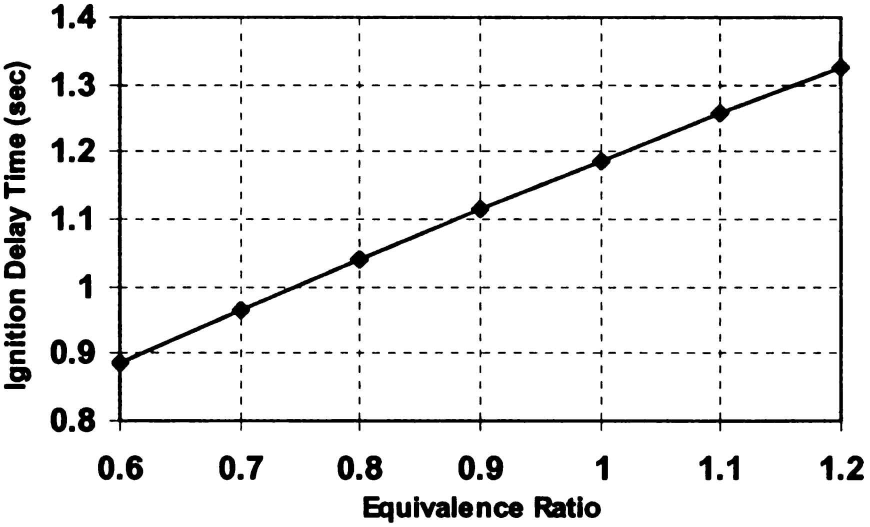

Figure 6-15. Ignition delay times of biogas mixture 6 at various equivalence ratios with P=1 atm, and $T_{initial}$=1000 K.

Table 6-3. Ignition delay times of biogas mixture 6 at various pressures and fixed equivalence ratio and initial temperature.

φ=1, $T_{initial}$ =1000 K	Thermal ignition time [sec]		
Pressure [atm]	Temperature inflection point (max. dT/dt) criterion	Peak of the OH profile criterion	Peak gas temperature [K]
1	1.097	1.097	2462
2	0.5494	0.5494	2493
3	0.3437	0.3437	2510.
4	0.2457	0.2457	2522
5	0.1896	0.1896	2531
6	0.1538	0.1538	2538
7	0.1291	0.1291	2544
8	0.1111	0.1111	2549

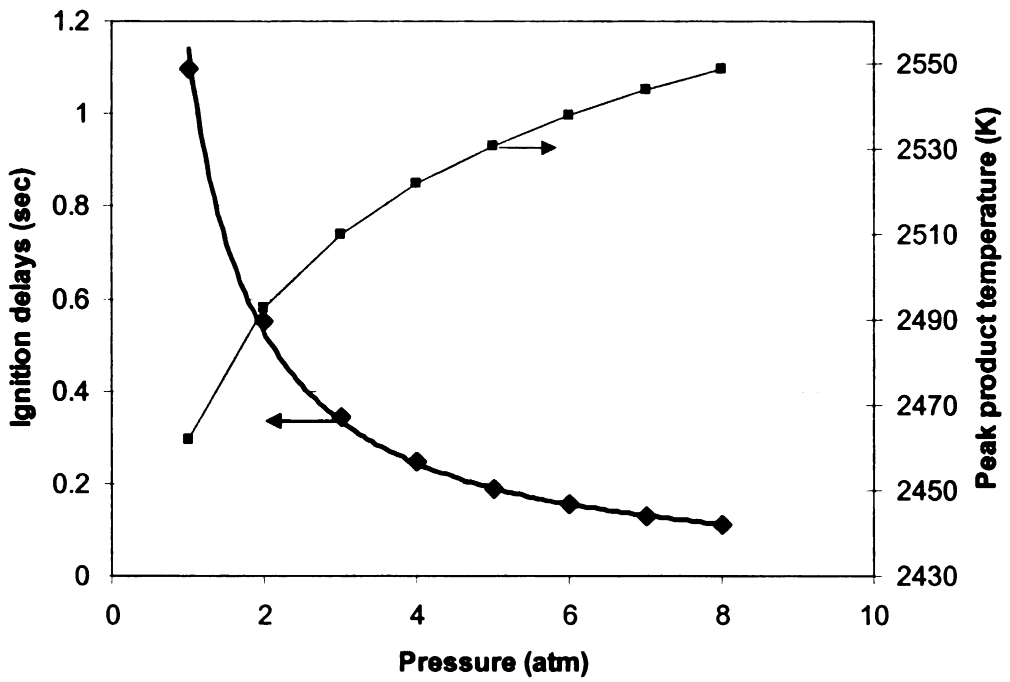

Figure 6-16. Ignition delay times and peak gas temperatures of biogas mixture 6 at various pressures, φ=1, T=1000 K.

temperature of 1000 K. A nearly linear increase is seen for the ignition delay times of biogas with respect to the increase of φ.

The effects of raising chamber pressure on ignition delays of biogas are seen in Table 6-3. The initial temperature is 1000 K and the mixture is stoichiometric. Values are also plotted in Figure 6-16. An overall pressure dependence $P^{-1.11}$ is found from this figure for biogas mixture 6. Future work will model ignition of biogas at high temperatures. The same modeling procedure is applied for various biogas mixtures, but results are not reported in this thesis.

6.6.3. Laminar flame speed of biogas/air mixtures

In this section, laminar flame speeds, S_L, of simulated biogas mixtures are calculated. A comparison of our computed laminar flame speed for methane using CHEMKIN and GRI-Mech 3.0 mechanism (for adiabatic conditions) with the most referred experimental and computational data in the literature is presented in Table 6-4. In this computation, the initial temperature and pressure are 298 K and 1 atm with $\varphi=1$. Our computed value lies well in the range of data from experiments and computations using other kinetic schemes.

Table 6-4. Comparison of calculated laminar flame speed for methane with the data in the literature.

No.	$\varphi=1$, P=1 atm, adiabatic conditions (q"=0)	S_L [cm/sec]
1	CH_4/Air: our computed value = V_{CH4}	39.61
2	CH_4/Air: Egolfopoulos et al. 1990, 1991 Experimental data [142]	40.2
3	CH_4/Air: computed by Egolfopoulos et al. 1992 [142]	39.3
4	CH_4/Air: Egolfopoulos et al. 1990 computed with a complete C_3 scheme [143]	39.2
5	CH_4/Air: Egolfopoulos et al. 1990 computed with a complete C_2 scheme [143]	39.5
6	Biogas mixture 6 [61% CH_4 +34% CO_2 + 5% N_2]/Air, our computed value	26.26= $\approx 0.66\times V_{CH4}$

A comparison of the computed results for biogas mixture 6 with calculations of Lafay et al. [86] using a different code (CANTERA) and the GRI-Mech 3.0 mechanism shows negligible difference (not reported here). The calculated downstream (products) temperatures from the solution of the governing equations for the CH_4/Air and biogas mixture 6/Air blends are 2230 K and 2113 K, respectively, which are very close to the adiabatic flame temperatures (T_{ad}=2224 K and T_{ad}=2114.4 K, respectively), confirming the assumption of adiabaticity in calculations. The discrepancies of S_L values are negligible suggesting that the computational technique as well as the reaction mechanism can be employed for an extensive investigation of biogas laminar flame speeds at various compositions.

Figure 6-17 depicts the calculated laminar flame speeds for CH_4/CO_2 mixtures with CO_2 proportions (in Vol. %) varying from 0 to 50. S_L decreases as the CO_2 percentage is increased; a quadratic fit is found (although it seems at a first look that the graph is linear)

$$S_L=-24.0233x\,[CO_2]^2-27.2011x\,[CO_2]+39.5432. \tag{6-9}$$

As illustrated in Figure 6-18, the concentration of H radicals also decreases as well as the downstream (product) temperature. Liu et al. [120] found that the competition of CO_2 for H radicals through the reaction $CO+OH \leftrightarrow CO_2+H$ with the most important chain branching reaction $H+O_2 \leftrightarrow O+OH$ plays a significant role that reduces the overall rate of combustion. As a result, laminar flame speeds or flame thicknesses are affected by CO_2 dilution.

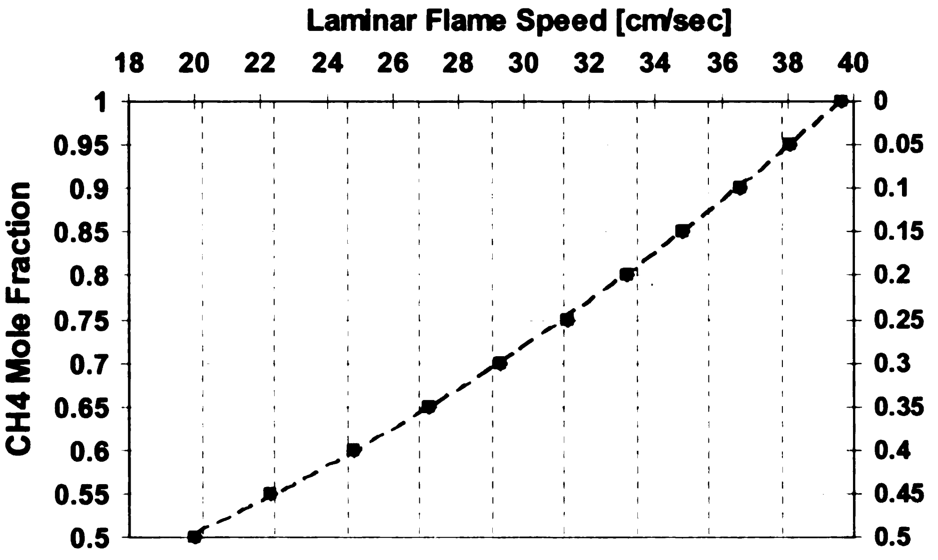

Figure 6-17. Effect of CO_2 concentration on the laminar flame speed of CH_4/CO_2 mixtures simulating biogas.

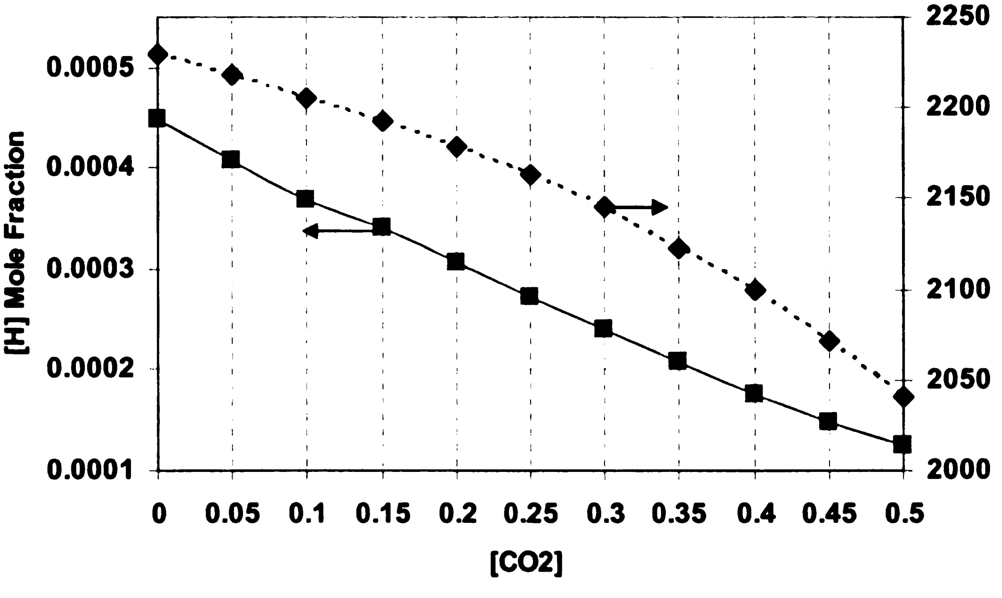

Figure 6-18. Effect of CO_2 concentration on the concentration of H radicals and downstream temperature for CH_4/CO_2 mixtures simulating biogas.

It is also of interest to investigate the effect of nitrogen content when the biogas methane content remains constant. Figure 6-19 demonstrates that with a fixed CH_4 mole fraction, when the N_2 mole fraction increases with respect to CO_2, the laminar flame speed increases; a quadratic curve fits well, which has the equation

$$S_L=9.2424x\,[N_2]^2+16.3597x\,[N_2]+24.8265. \qquad (6\text{-}10)$$

The replacement of CO_2 by N_2 will increase the downstream temperature (not shown here).

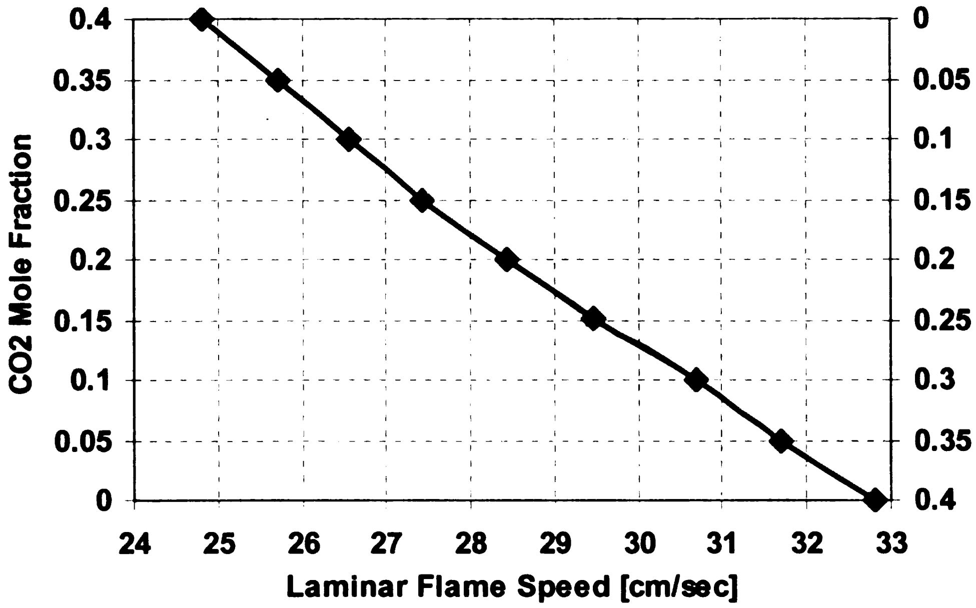

Figure 6-19. Relative effect of N_2 and CO_2 concentration on the laminar flame speeds of $CH_4/CO_2/N_2$ mixtures with constant CH_4 concentration, $[CH_4]=0.6$.

In the calculations presented so far, the initial temperature was 298 K and the pressure was 1 atm. Some correlations have been reported in the literature, which relate the laminar flame speed with the temperature and pressure. For methane/air mixtures, Kobayashi and co-workers [144] report one such correlation from [145],

$$S_L = S_{L0}(T/T_0)^m (P/P_0)^n \tag{6-11}$$

where P and T are the pressure and temperature of the mixture, and T_0, P_0, and S_{L0} are, respectively, 300 K, 0.1 MPa, and laminar flame speed at these conditions as reference values (very close to our calculated values at 298 K, 1 atm). Kobayashi and co-workers report that the temperature exponent, m, and pressure exponent, n, used are 1.9 and -0.5, respectively, based on the experimental data [144] and numerical analysis. The accuracy of such correlations to predict the S_L for blends of diluted hydrocarbons is not certain and needs more investigation.

Chapter 7 Thermal and Chemical Structure of Biogas Counterflow Diffusion Flames

In this chapter, the thermal and chemical structure of biogas counterflow diffusion flames is studied [146]. CO_2 diluted methane blends, which are typical biogas blends, are of interest to this study. The chemical and thermal influences of the addition of CO_2 as a diluent are investigated in a counterflow diffusion flame configuration. The computational investigation uses a CHEMKIN [125] based numerical code. Two detailed reaction mechanisms and a reduced mechanism are evaluated and compared to experiments [36]. Four non-sooting biogas diffusion flames are compared to quantitatively examine thermal and chemical effects of CO_2 content of biogas on flame temperature, major species, minor species, and emissions of NOx, soot and green house gases.

Most studies on the effects of diluents in non-premixed flames include either counterflow or coflow configurations with diluents added to either the fuel or oxidizer streams. Rortveit et al. [147] studied a H_2 counterflow diffusion flame diluted in the fuel stream with N_2, CO_2, or He. All three diluents reduced the flame temperature. CO_2, the most efficient diluent, reduced the temperature largely through dissociation. The heat capacity of a diluent also plays a significant role in altering the temperature. Recently, Berry Yelverton and Roberts [148] measured the soot surface temperature in He, Ar, N_2, and CO_2 diluted ethylene jet diffusion flames. Among these diluents, the effects of heat capacity as well as small contributions from radiative heat loss made the CO_2 diluted flame the coolest. It is known that CO_2 directly participates in chemical reactions primarily through the elementary reaction $CO_2+H \rightarrow CO+OH$ [117, 118, 149] and to a lesser extent $CO_2+CH \rightarrow CO+HCO$ [119]. Earlier studies have shown that CO_2 dilution of fuel in a diffusion flame can suppress soot and NOx [150, 151]. The reaction $H+NO \rightarrow HNO$ was important in the destruction and formation of prompt NO [123].

In diffusion flames, addition of a diluent to a fuel may produce four categories of effects: [120, 151] (1) transport (or dilution) effects by reduction in concentration of reactive species and thus their collision frequencies; (2) thermal effects by changing the flame temperature; (3) radiative effects by changing the radiation transfer from the hot products; and (4) direct chemical effects by participation of diluents in chemical reactions. For CO_2, attempts have made to isolate transport, thermal, radiative, and chemical influences. Two methodologies have been proposed in the literature: (1) The technique used in the experiments of Du et al. [151] to isolate dilution, thermal and chemical effects by comparing results of a pure ethylene flame and three diluted ethylene flames: a CO_2 diluted flame, a CO_2 diluted flame with the same temperature as pure fuel, and an N_2 diluted flame with the same temperature as pure fuel. Controlling the flame temperature was achieved by the adjustment of Ar and N_2 concentrations in the oxidizer stream; (2) The methodology proposed by Liu et al. [119] to numerically identify chemical effects of CO_2 addition to ethylene. They identify a normal CO_2 that participates in reactions and a fictitious CO_2 that has exactly the same thermochemical and transport properties as the normal CO_2, but is chemically inert. The radiative properties of the normal and fictitious CO_2 were added for similar studies by Park et al. [121] who implemented this method.

Biogas may have variable compositions and low qualities. A drawback with biogas combustion, in general, is its small LHVs and diminished flame temperatures. Upgrading costs and heat release reduction are sometimes masked since the environmental advantages are well highlighted; the reduction of NOx emissions, for instance, has been related to lower flame temperatures. Biogas upgrading to remove CO_2 should be optimized in such a manner that ensures: (1) Minimum possible upgrading to reduce cost and (at the same time) yielding the benefit from the influences of CO_2 on NOx emissions reduction and soot suppression; (2) Operability and stability of the combustor in as wide a range as possible, obtaining target heat release regions, and (for premixed flames) proper ignition delay times and flame speeds for efficient operation.

The focus of this study is on examining the thermo-chemical structure of biogas diffusion flames by considering carefully selected boundary conditions. Criteria used to select these conditions are explained in Section 7.1.1. Any change in CO_2 concentrations and boundary conditions in the inlet fuel stream (reactant gases) of a biogas diffusion flame results in a change in biogas composition and mass flow rate. In gas turbines, the mass flow rate is related directly to the compression work. Although various effects of CO_2 addition to fuels such as CH_4, C_2H_4 and C_3H_8 have been studied for various aforementioned applications, there remains a lack of detailed understanding of the mechanisms through which biogas utilization can reduce emissions of soot, NOx, and green house gases (GHG). In the case of the green house gases (CO_2, CH_4 and N_2O) it is vital to indicate whether or not their *net* release is reduced.

This study examines the chemical kinetics of blends of diluted hydrocarbons that simulate biogas. A biogas fuel can be simulated as a blend of CH_4, CO_2, N_2, and H_2O (constituents similar to biogas from digestion saturated with water vapor). Here we examine CO_2 diluted CH_4 blends, which describe a typical dry biogas. In order to investigate the chemical and thermal influences of the addition of CO_2 as a diluent, a counterflow diffusion flame is selected for analysis. Four non-sooting biogas diffusion flames are compared to quantitatively examine the thermal and chemical effects of CO_2 content of biogas on flame temperature, major species, minor species, and emissions of NOx, soot and green house gases. Major and certain C_2 species for one of the flames are compared with available experimental data [36].

7.1. Numerical Approach

In our previous study [152], we employed a laminar counterflow diffusion flame with CO_2 proportions varying from 20 to 50 (vol. %) in a fuel stream comprising only CH_4 and CO_2. Here, we use a fuel stream mixture of CH_4 and CO_2 highly diluted by N_2 in order to study the detailed chemical kinetics of biogas. A schematic of our laminar counterflow diffusion flame configuration is shown in Figure 1. A planar, steady, non-sooting flame is generated by impinging a uniform oxidizer jet against a uniform biogas/N_2 jet. The stoichiometric mixture fraction, z_f, and the density corrected strain rate, a, for our counterflow flame are employed as defined by Eq. ((3-4) and Eq. ((3-3), respectively. The CHEMKIN based numerical code OPPDIF [136], is utilized. Radiative heat loss is not considered.

The method of isolating chemical and thermal effects of biogas CO_2 content follows that of Du et al. [151] However, when we systematically add CO_2, unlike Du et al. [151] and our previous study [152], the reactive species mole fraction (here CH_4) is kept constant or is changed very slightly to minimize the alteration of the peak flame temperature, the flame shape, and its location. This allows us to capture the chemical and thermal influences of CO_2 addition to the fuel stream while ensuring minimal changes to

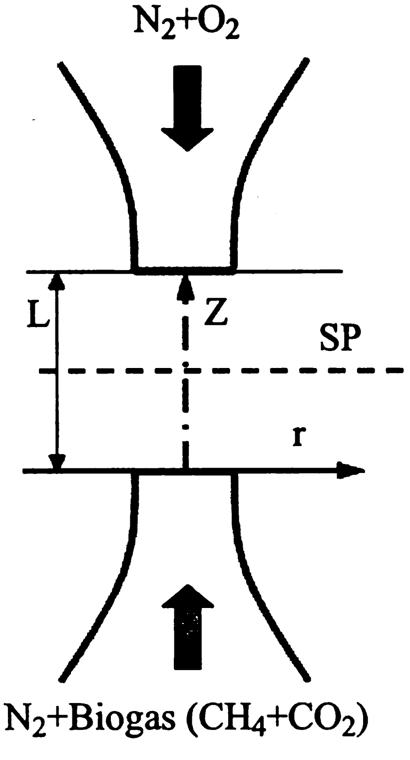

Figure 7-1. Schematic of the counterflow burner setup for the chemical kinetics study (L=14.1 mm; SP: stagnation plain). A nitrogen shroud is usually used in experiments.

the flame stoichiometry and the entire temperature field. When CO_2 is added the adjustment of the flame temperature is achieved not by changing the oxidizer composition [151] (which may change the transport properties) or by preheating the fuel, but by a slight increase in the CH_4 mole fraction.

7.1.1. Criterion for biogas flame comparison

Four flames are numerically investigated and compared, called Flames 1 to 4. For all four flames, L=14.1 mm and the fuel steam enters at the origin of the coordinate system. Boundary conditions are listed in Table 1. Boundary conditions for Flame 1 are selected similar to those of a baseline methane counterflow diffusion flame in the experiments of Bufferand et al. [36] (See Flame A in Table 3-1). This flame has been experimentally established (by adjusting z_f, a, and feed stream compositions) in such a way as to generate non-sooting, laminar, steady, stable conditions. The chemical structure of this methane counterflow diffusion flame has been analyzed by gas sampling via quartz microprobes (O.D. ≈ 340 μm) and subsequent GC/MS analysis. A gas chromatograph equipped with thermal conductivity (TCD), flame ionization (FID) and mass spectrometry detectors (MSD) have been utilized for the chemical analysis. Details of the experimental methodology as well as a schematic of the setup can be found in Chapter 3 and in [36, 37]. For Flame 1, $z_f = 0.76$ and $a = 134.4\ s^{-1}$. The oxidizer composition is unaltered between Flames 1-4. These flames are very lean with a global equivalence ratio, φ, of about 0.27. As seen in Table 1, strain rates of the four flames are very close with a maximum 2% deviation. This suggests that we should expect very close flame thicknesses since the flame thickness, δ, varies inversely with a [135]. The values

Table 7-1. Boundary conditions of Flames 1-4

	Biogas composition (% CH_4+ % CO_2), Vol. %	**Flame 1** (100% CH_4)	**Flame 2** (40% CO_2+ 60% CH_4)†	**Flame 3*** (39% CO_2+ 61% CH_4)†	**Flame 4** (60% CO_2+ 40% CH_4)§
Fuel Side	Molar Composition				
	CH_4	0.1029	0.1029	0.1080	0.1029
	CO_2	0	0.0686	0.0686	0.1543
	N_2	0.8971	0.8285	0.8234	0.7427
	Biogas (CH_4+CO_2) Mass Flux (g/(cm^2.min))	0.17	0.48	0.49	0.87
	Total Mass Flux (g/(cm^2.min))	2.77	2.89	2.88	3.03
	Temperature (K)	380	380	380	380
Oxidizer side	Molar Composition				
	N_2	0.2271	0.2271	0.2271	0.2271
	O_2	0.7729	0.7729	0.7729	0.7729
	Mass Flux (g/(cm^2.min))	3.19	3.19	3.25	3.19
	Temperature (K)	340	340	340	340
	Strain Rate (s^{-1})	134.4	135.8	137.0	137.4
	z_f	0.76	0.77	0.76	0.78

* Note that the temperatures of Flame 1 and Flame 3 are identical.

† Typical compositions for biogas from anaerobic digestion (AD) plants.

§ Typical compositions for biogas from active or recently closed landfills.

of z_f increase very slightly for Flame 2 and Flame 4, yielding nearly fixed flame locations.

Flame 1, Flame 2, and Flame 4 have the same oxidizer and fuel flow velocities. In Flames 2 and 4 the CO_2 mole fraction is 6.86 % and 15.43 %, respectively, which corresponds to a 60%CH_4-40%CO_2 (vol. %) biogas and a 40%CH_4-60%CO_2 (vol. %)

biogas in the fuel stream. On the one hand the 60%CH_4-40%CO_2 composition is typical for biogas extracted from digesters in anaerobic digestion (AD) plants. On the other hand, the 40%CH_4-60%CO_2 composition is typical for biogas from active or recently closed landfills. In Flames 1, 2 and 4, the CH_4 mole fraction is deliberately kept constant (to ensure as small stoichiomtry changes as possible), however, substitution of N_2 by CO_2 reduces the peak flame temperature by 41 K and 85 K in Flames 2 and 4, respectively. To properly compare Arrhenius kinetics and in order to fix the flame location, temperature profiles and mixture fractions should be unaltered [36]. Flame 3 is obtained by an adjustment of the Flame 2 boundary conditions that ensures nearly identical temperature profiles (temperature fields) and z_f values with Flame 1. We increased the CH_4 mole fraction by 5% to raise the temperature. To move the flame, we increased the oxidizer velocity by 2%. Similar adjustment strategies to fix the flame temperature and location have been employed by previous investigators [36, 37]. The CO_2 mole fraction is identical for Flames 2 and 3.

7.2. Comparison of reaction mechanisms for Flame 1

For Flame 1, three reaction mechanisms are evaluated and compared: (1) the GRI-Mech 3.0 detailed mechanism [79], which includes 325 chemical reactions and associated rate coefficients and thermochemical parameters for the 53 included species. It consists of 106 reactions including nitrogen chemistry; (2) the San Diego (SD) detailed mechanism [129], which is composed of 46 species and 235 reactions; (3) the GRI-Mech 1.2 reduced mechanism (released 1994) [134] which includes 22 species (+N_2 and Ar) and 104 reactions. Mechanisms (2) and (3) do not include NOx chemistry.

A comparison of the calculated major species profiles (using three reaction mechanisms) for CH_4, CO_2, CO, and O_2 with the experimental data of Bufferand et al. [36] in Figure 7-2 shows good agreement. All mechanisms show negligible differences for these major species (see Figure 7-2). The calculated CO mole fraction peak is nearly 1.7× greater than that of the experiments. It is an established fact that the CO oxidation can be catalyzed by moisture [49]. It is very sensitive to small deviations in relative humidity and

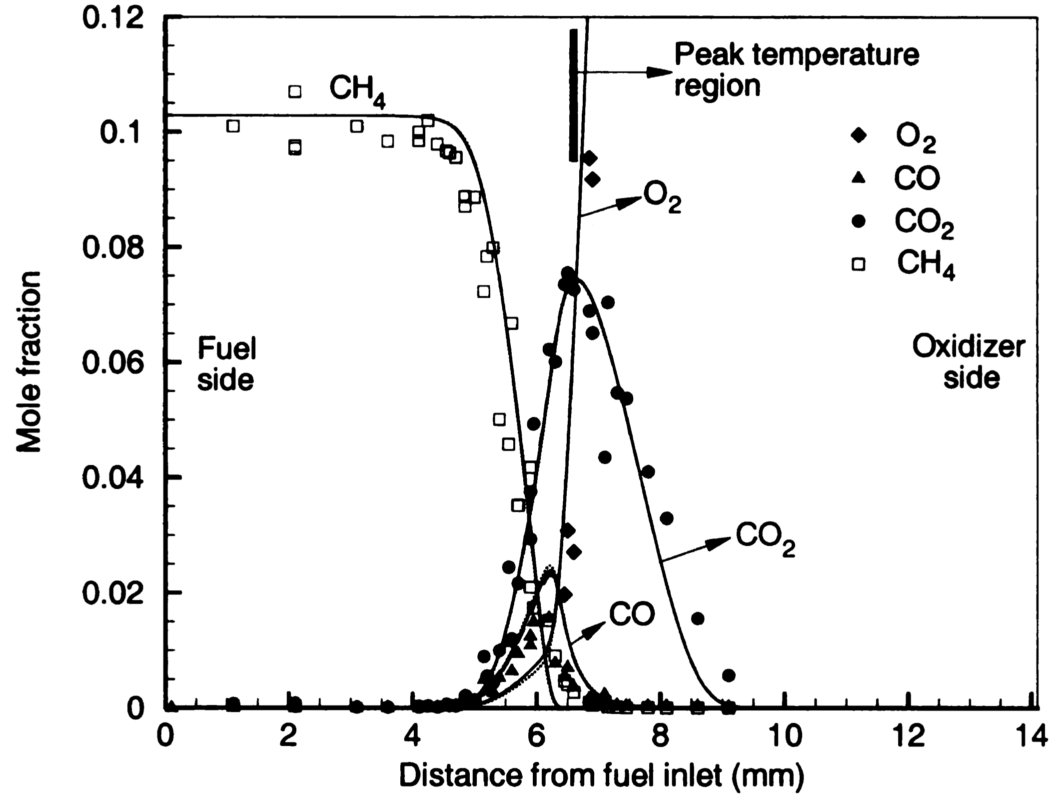

Figure 7-2. Profiles of major species (O_2, CH_4, CO_2, and CO) for Flame 1. Comparison between a) solid lines: GRI 3.0 mechanism; b) dashed lines: SD mechanism; c) dotted lines: reduced GRI 1.2 mechanism; d) symbols: experiments of Bufferand et al. [36].

other factors that are not yet incorporated in the standard reaction codes. Temperature peak locations are almost identical between both detailed mechanisms (GRI-Mech 3.0 and SD). The flame sheet (the peak flame temperature region) locates at z~6.6 mm.

Small differences in the peak magnitude ($\Delta T_{max} \sim 8$ K) are revealed (the temperature profile for the GRI-Mech 3.0 mechanism is shown in Figure 7-5). However, the peak temperature for the reduced mechanism is almost 15 K and 23 K lower than the GRI-Mech 3.0 and SD mechanisms, respectively. The flame sheet is slightly shifted toward the fuel side.

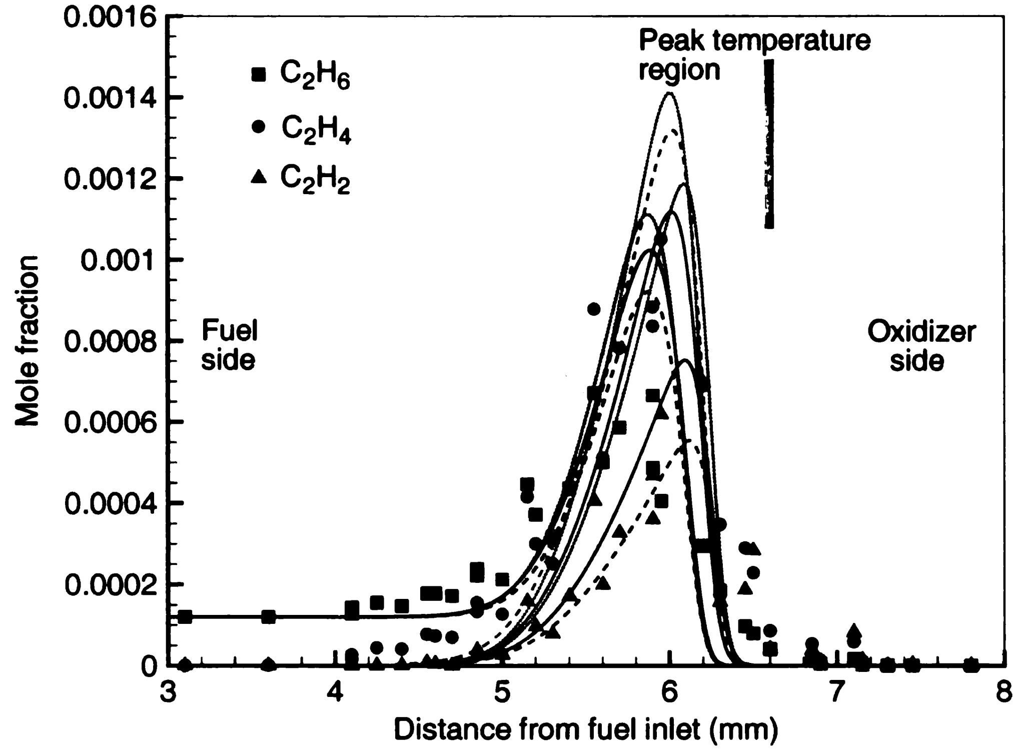

Figure 7-3. Profiles of C_2 species (blue: C_2H_2, red: C_2H_4, black: C_2H_6) for Flame 1. Comparison between a) solid lines: GRI 3.0 mechanism; b) dashed lines: SD mechanism; c) dotted lines: reduced GRI 1.2 mechanism; d) symbols: experiments of Bufferand et al. [36] The fuel supply in experiments contained about 120 ppm of ethane.

Figure 7-3 illustrates profiles of three major "C_2 species" formed in methane flames, C_2H_2, C_2H_4 and C_2H_6. The fuel source in the experiments [36] contained about 120 ppm ethane impurities. Profiles of C_2 species in experiments and computational results with the GRI-Mech 3.0 mechanism agree satisfactorily. The acetylene mole fraction is overpredicted by the reduced mechanism and underpredicted by the SD mechanism; however, the latter performs relatively better. Both the reduced GRI-Mech and SD mechanisms overpredict the ethylene mole fraction. All three mechanisms perform fairly in predicting the ethane distribution, possibly due to the ethane impurities of the fuel supply (in the experiments).

Profiles of H, OH and CH_3 radicals are presented in Figure 7-4. Slight discrepancies between both detailed mechanisms (GRI-Mech 3.0 and SD) are observed in the profiles of OH, H, and CH_3. With respect to the detailed GRI-Mech mechanism, the reduced GRI-Mech mechanism always overpredicts these radicals. Thus, the reduced

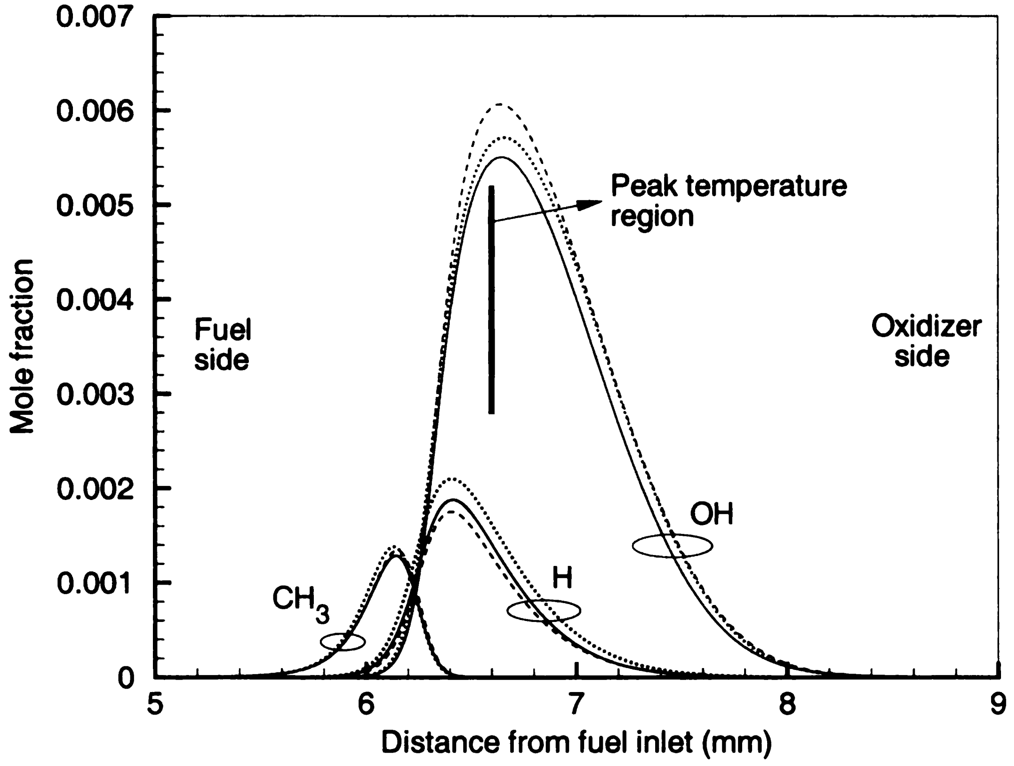

Figure 7-4. Profiles of H, OH, and CH_3 radicals for Flame 1. Comparison between a) solid lines: GRI 3.0 mechanism; b) dashed lines: SD mechanism; c) dotted lines: reduced GRI 1.2 mechanism.

mechanism fails to perform adequately for the purpose of study, which aims at tracking the behavior of every major and minor species, and all important radicals.

Contrasting computational results with experiments in the preceding profiles suggests that the GRI-Mech 3.0 mechanism performs slightly better than the SD mechanism for this study. Also, GRI-Mech 3.0 has an advantage over the SD mechanism: it includes NOx chemistry. GRI-Mech 3.0 is therefore employed for the remainder of our computations.

7.3. Influences of CO_2 content of biogas; Comparison of Flames 1-4

7.3.1. Temperature and velocity

Figure 7-5a presents profiles of temperature and axial velocity for Flames 1-4. The stagnation plane for Flame 1 is at z ~ 7.3 mm. All flames lie on the fuel side of the stagnation plane. Except for the oxidizer velocity in Flame 3, which was adjusted to be 2% more than that of other three flames, all other oxidizer boundary conditions are identical for Flames 1-4. As a result, no distinction is seen between profiles of temperature on the oxidizer side of the flame. The volume flow rate of the fuel stream is constant for all flames. The full width at half maximum (FWHM) criterion for temperature profile is used to define the flame thickness, δ. Here, δ ranges between 2.5-2.6 mm for Flames 1-4. As seen in this figure and in its magnified version, Figure 7-5b, the entire temperature fields of Flames 1 and 3 are indistinguishable, which ensures that the strategy we used to match these profiles is successful. Comparison of temperature profiles in Figure 7-5b shows a maximum offset of 0.14 mm in peak locations between

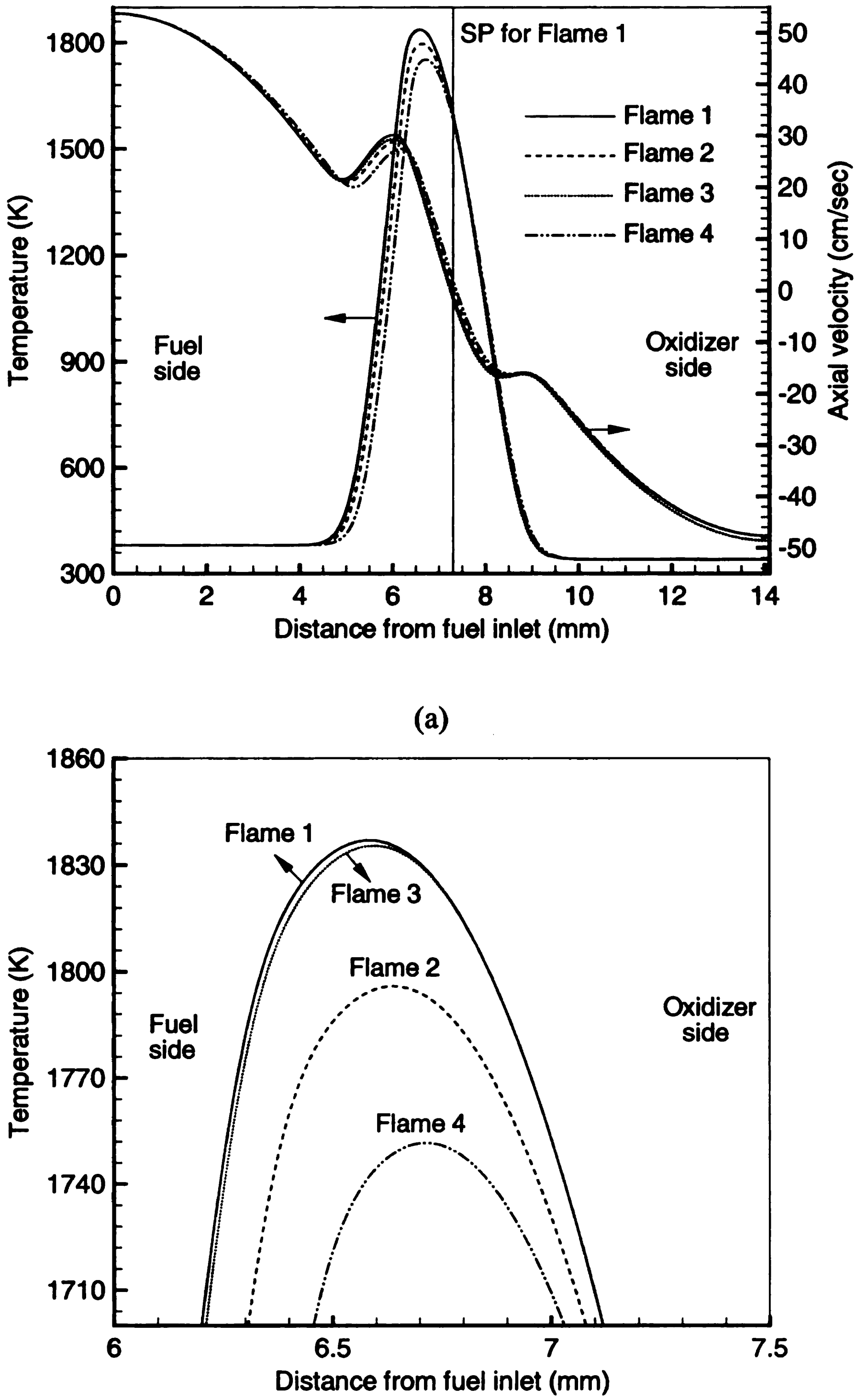

(a)

(b)

Figure 7-5. a) Comparison of temperature and axial velocity profiles for Flames 1-4; b) Magnified version of temperature profiles near the peaks. The stagnation plane for Flame 1 is at z ~ 7.3 mm. All flames are on the fuel side of the SP.

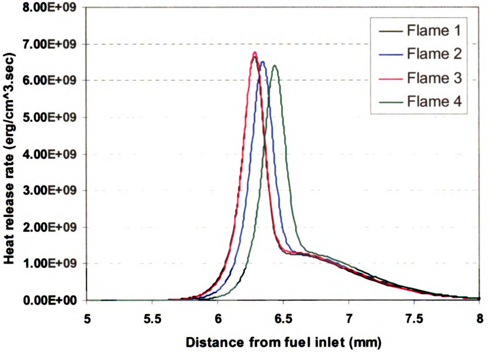

Figure 7-6. Comparison of heat release profiles (signatures) for Flames 1-4 in the reaction zone.

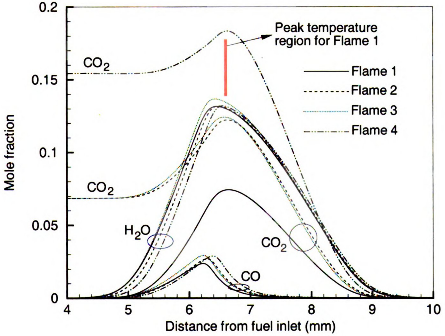

Figure 7-7. Comparison of the mole fractions of CO_2, H_2O and CO for Flames 1-4. Solid lines for CO and CO_2 profiles in this Figure and Figure 7-2 are the same.

these four flames. This is the direct consequence of fixing the CH_4 mole fraction for Flames 1, 2, and 4. The offset in the temperature peaks as well as the reduction in peak magnitude is attributable to the increase in the CO_2 content. Figure 7-6 delineates heat release signatures (profiles) for Flames 1-4 in the reaction zone. In addition to the temperature fields, heat release signatures of Flames 1 and 3 are nearly identical.

7.3.2. Major species, radicals and intermediate species

Figure 7-7 illustrates profiles of CO_2, CO and H_2O for Flames 1-4. As expected, the CO_2 mole fraction has the maximum value in Flame 4. Flame 3 has a nearly 21 % greater CO mole fraction than Flame 1. This difference is mainly due to the conversion of CO_2 in the fuel stream of Flame 3 and its chemical participation through reactions such as

R1: $CO_2+X \rightarrow XO+CO$

R2: $CO_2+CH \rightarrow HCO+CO$

R3: $CO_2+CH_2^* \rightarrow CO+CH_2O$

where X may be one of these radicals: H, OH or O. Figure 7-8a presents a comparison between mole fractions of the important chain branching radicals; H, O and OH for Flames 1-4. Comparison between Flames 1, 2, and 4 with different temperatures reveals that CO_2 dilution reduces the mole fraction of these radicals. The maximum reduction between Flames 1-4 is 20 %, 21%, and 34% for O, OH, and H radicals, respectively. Comparison of H profiles in Figure 7-8b, which is a magnified version of Figure 7a, shows that, in general, CO_2 dilution has a greater effect on H radicals than on OH and O radicals.

As demonstrated in Figure 7-8b, the difference between the H profiles for Flame 1 and Flame 3 (with identical temperature profiles as in Figure 7-5b) indicates the *chemical effects* of the CO_2 addition (dilution). The difference between the H profiles for Flame 2 and Flame 3 (with identical inlet CO_2 mole fractions as in Figure 7-7) indicates the *thermal effects* of the CO_2 addition. This interpretation is used in the discussion of this and all subsequent figures. With respect to O and OH, the chemical influences of CO_2 addition are the most effective for H. This is exhibited in the comparison of Flames 1 and 3. When Flame 1 is diluted by CO_2 to form Flame 3, the peak of the H profile is reduced by approximately 7.6% whereas the reduction in the peak of O radicals (Figure 7-8a) is much smaller, and the OH profiles can hardly be discriminated. The thermal effects of CO_2 dilution on H, O, and OH radicals are nearly of the same order.

Figure 7-9a presents profiles of methyl radicals (CH_3) and formaldehyde (CH_2O) for Flames 1-4. The peak CH_3 for Flame 1 is at $z \sim 6.15$ mm. CO_2 addition shifts the CH_3 profile toward the oxidizer side. The peak magnitude is also reduced; the reduction is modest for Flame 3 (there was a 5% difference between Flames 1 and 3 in the mole fractions of CH_4, the primary source of CH_3). This amplifies the notion that the direct chemical effect of CO_2 on the concentration of CH_3 radicals is modest by contrast with its thermal effects (compare Flames 2, 3). This is consistent with Figure 7-8 and highlights the influence of H, O and OH radicals on CH_3 concentration through important chain branching reactions such as CH_4+H→CH_3+H_2, CH_4+O→CH_3+OH, and CH_4+OH→CH_3+H_2O.

In an interesting trend, the addition of CO_2 increases the CH_2O peaks as seen in Figure 7-9a. CH_2O is an important intermediate in the CH_4 reaction pathways. Both Flames 2 and 3 with the same CO_2 content in the fuel stream produce very close CH_2O peaks. This result undermines the thermal effects of CO_2 dilution on the formation of CH_2O (i.e., CO_2 produces a weakly temperature-dependent effect on CH_2O). Chemical influences of CO_2 on CH_2O formation are more pronounced and favor its formation e.g., through the reaction (R3).

Profiles of CH radicals are shown in Figure 7-9b. Both Flames 1 and 3 peak at almost the same location (z ~ 6.3 mm). With respect to Flame 1, the peak magnitude for Flames 2, 3, and 4 reduces by 38%, 21% and 66%, respectively. The CH radical (methyne) is the dominant immediate precursor to prompt NOx [115]: its reduction is expected to reduce NOx. This will be elaborated in Section 3.2.4. 61%CH_4-39%CO_2 biogas (typical for AD plants) in Flame 3 significantly reduces the CH radical concentration. This reduction can be attributed to the direct chemical influence of CO_2 on CH through reactions such as CO_2+CH →HCO+CO or to its indirect influence to a lesser extent through the reduction of H and OH radicals.

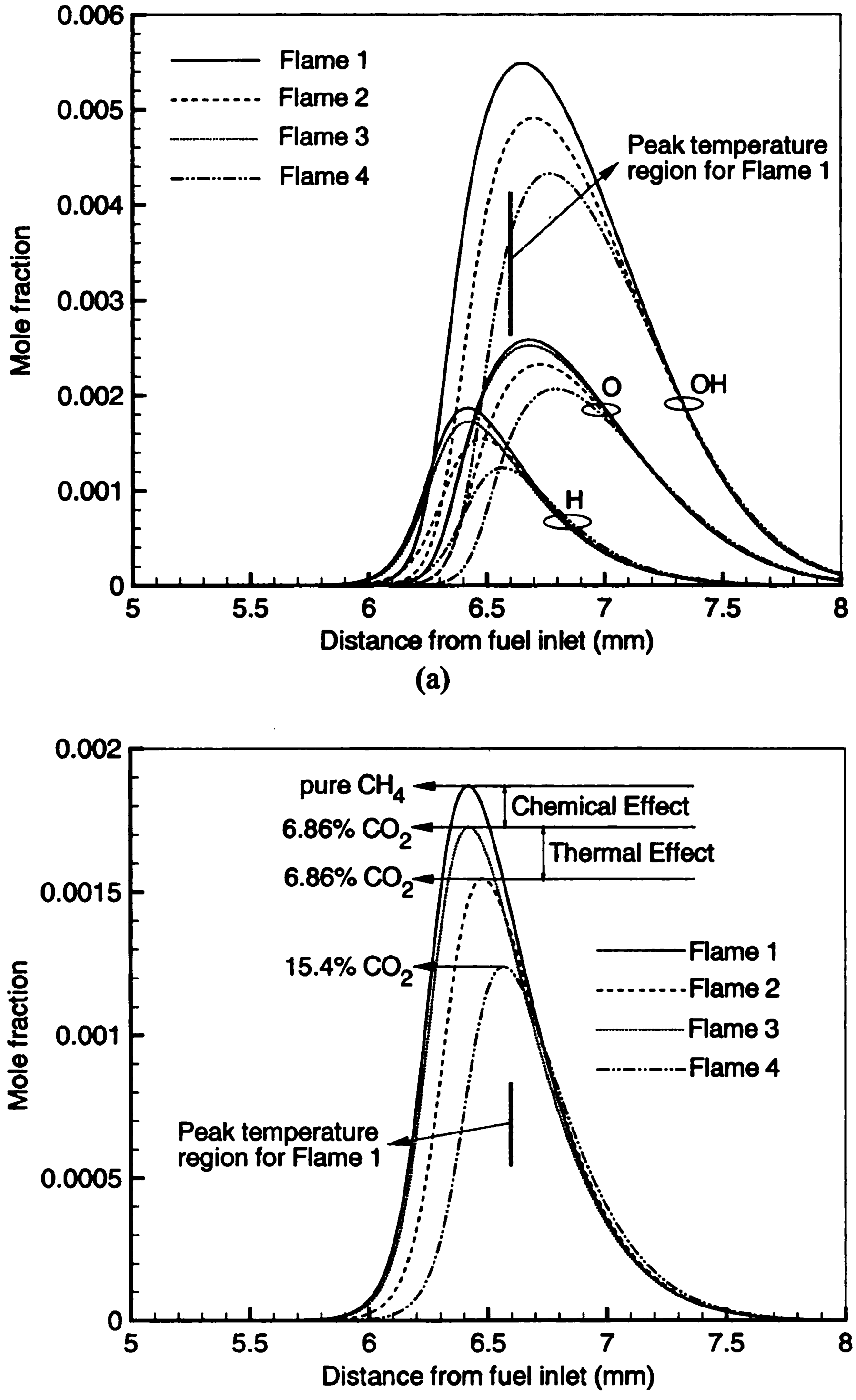

(a)

(b)

Figure 7-8. a) Comparison of the mole fractions of H, O and OH radicals for Flames 1-4; b) Magnified version of Figure (a) showing the mole fractions of H radicals. The percentages of CO_2 in the fuel stream have been written. Note the quantitative definitions of "chemical effect" and "thermal effect", which are employed (without explicit demarcation) in all subsequent figures.

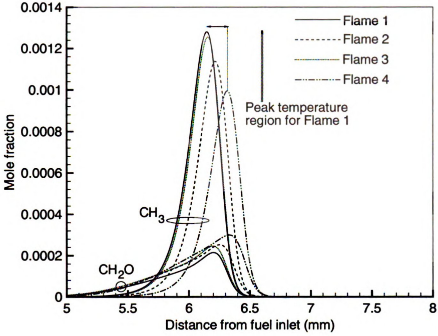

(a)

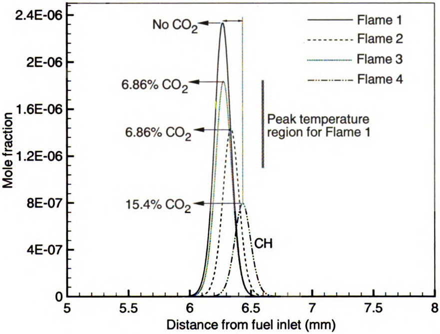

(b)

Figure 7-9. Comparison of the mole fractions of a) CH_3 radicals and CH_2O; b) CH radicals for Flames 1-4. The percentages of CO_2 in the fuel stream have been written.

7.3.3. Soot precursors

C_2 species, mainly C_2H_2, C_2H_4 and C_2H_6, are soot precursors and the main source of the CH and CH_2 radicals that are responsible for "prompt NO" production [115]. Figure 7-10 shows the mole fractions of acetylene as well as the decay of CH_4 for Flames 1-4. The reduction in the peak of acetylene, which is an important soot precursor and surface growth species, suggests that biogas may be beneficial for soot suppression. This statement is consistent with the recent study of Guo et al. [122] that showed the chemical effect of CO_2 addition to an ethylene/air diffusion flame suppresses soot inception and surface growth rate whereas it has only a negligible influence on soot oxidation. More studies on sooting or incipiently sooting biogas flames are needed to ascertain whether the CO_2 addition can also alter reburn of either acetylene (through reactions like $C_2H_2+O \rightarrow OH+C_2H$) or soot particulates.

The observed shift in the peak locations of radicals (see Figure 7-8 and Figure 7-9) is consistent with the shift in the decay of CH_4. Flames 1 and 3 show close peak locations for radicals (see Figure 7-8 and Figure 7-9) and for C_2H_2 (see Figure 7-10). This is consistent with the CH_4 trend in Flames 1 and 3. Flame 1 produces nearly 2.4× as much acetylene as Flame 4. Since the primary source of acetylene is methane, and the CH_4 mole fraction is fixed for Flames 1 and 4, the reduction must be caused by the presence of CO_2 in the fuel stream of Flame 4.

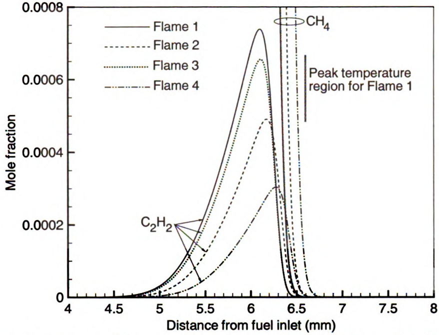

Figure 7-10. Comparison of the mole fractions of acetylene for Flames 1-4. The decay of CH_4 profiles is also demonstrated in this Figure.

The flame temperature has a profound influence on soot formation. Flames 1 and 3 have indistinguishable temperature-time histories. The acetylene peak for Flame 3, however, is 11% smaller than that of Flame 1. This reduction is therefore attributed to the *chemical effects* of CO_2 in biogas. The comparison of Flames 2 and 3 shows that the thermal effects, which reduce the flame temperature (Figure 7-5b), are comparatively greater.

Removal of C_2 precursors of prompt NOx from the diffusion flames may also be beneficial for NOx reduction [115]. It was suggested in the discussion of Figure 7-9 that NOx could be reduced when using biogas even when the temperature does not change. NOx reduction is discussed in the next section.

7.3.4. NOx emissions

Figure 7-11 shows a comparison of the N radical and NO mole fractions for Flames 1-4. The peak NO for Flame 1 locates at z~6.55 mm. The peak NO for Flames 1-4 is in close proximity to the temperature peak. We expect a decrease in the NO concentrations for Flame 2 and especially for Flame 4. The peak for the N radical in Flame 4 is approximately 15% of the N peak in Flame 1. The N radical plays an important role in "thermal NO" formation through the reaction $N+O_2 \rightarrow NO+O$. The chemical influences of CO_2 on the reduction of N radicals predominate: compare Flames 1, 3 whose thermal profiles are essentially identical. Flame 4 shows an NO peak approximately 1/4 of Flame 1. This substantial reduction does not appear to be a result of N_2 concentration changes in the fuel stream. Flames 2 and 3 with very close N_2 mole fractions in the fuel stream produce very different NO peaks. This reduction is due to both thermal and chemical effects of CO_2 dilution. Flame 4 uses a low-quality biogas (landfill biogas) with a mass flux almost 5× greater than Flame 1. Comparing the pure CH_4 flame (Flame 1) and the landfill biogas flame (Flame 4) shows that there exists a peak temperature reduction of $\Delta T=85$ K and a large difference in the mass flux. The reduction in the peak of NO (25% ratio) is feasible only if the associated loss in heat release and rise in mass flux are acceptable for a specific application. It is more economical to use: 1) lower mass fluxes; 2) less biogas upgrading, which means a higher CO_2 content and a lower quality. Contrasting Flames 2 and 4 shows that there is a tradeoff between these two factors; for the lower quality biogas the reduction of NO is larger, but the mass flux (and thus the required compression work) is higher.

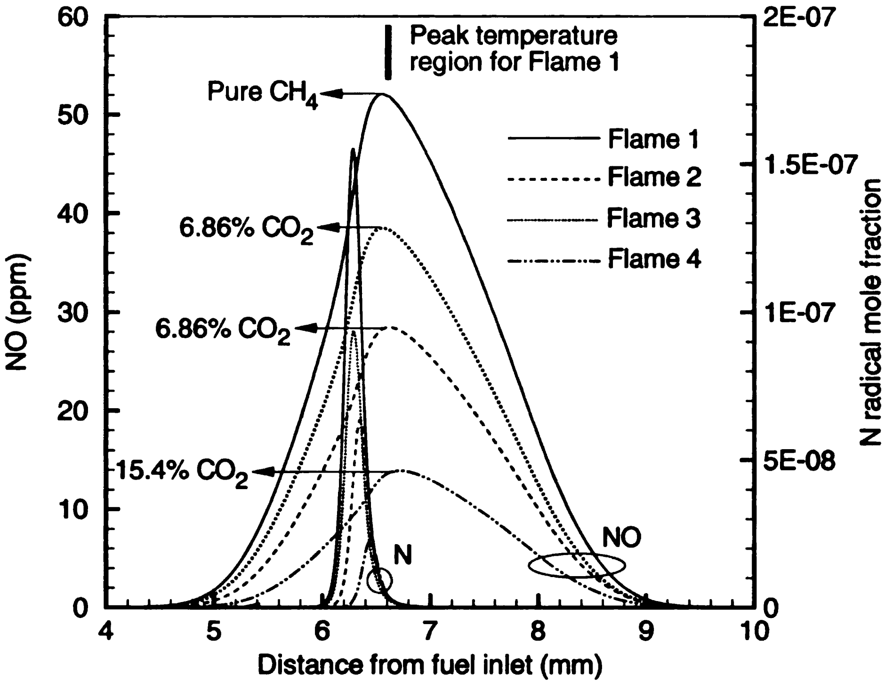

Figure 7-11. Comparison of the mole fractions of N radicals and NO (in ppm) for Flames 1-4. The percentages of CO_2 in the fuel stream have been written.

Comparison of Flames 2, 3 shows, as expected, that the flame temperature, which is directly altered by dilution, plays a significant role in NO reduction. Flames 2 and 3 use a biogas with compositions more similar to a typical biogas from the anaerobic digestion process. For these flames, which have very similar biogas compositions and only a 1.7% difference in the biogas mass flux in their fuel stream, ΔT is 40 K while the NO peak shows a 26% difference.

Flame 3 has a similar temperature profile to Flame 1 with a biogas mass flux nearly 2.9× larger than Flame 1, but its NO peak is less than Flame 1 by about 26%. Comparison of Flames 1 and 3, however, lends additional credence to the beneficial influence of biogas in NO reduction. In this case a temperature decrease cannot explain the NO reduction. It must be explained by the chemical influence of CO_2 on NO.

Reduced concentrations of CH radicals and C_2 species (Figure 7-9b, Figure 7-10) as well as N radicals suggests a possible reduction in both prompt and thermal NO formation.

Figure 7-12 presents profiles of nitrogen dioxide (NO_2) and nitrous oxide (N_2O) for Flames 1-4. In Flame 1, the peaks of NO_2 and N_2O are located at z~ 8.2 mm and z~ 7.2 mm, respectively. Both peaks are on the oxidizer side of the flame. NO_2 shows a small second peak at z~ 5.5 mm on the fuel side. NO_2 may be attacked by H and O radicals between these two peaks (where radicals are abundant) and converted to NO or other species. NO_2 shows a trend similar to NO with a decrease in peak values when CO_2

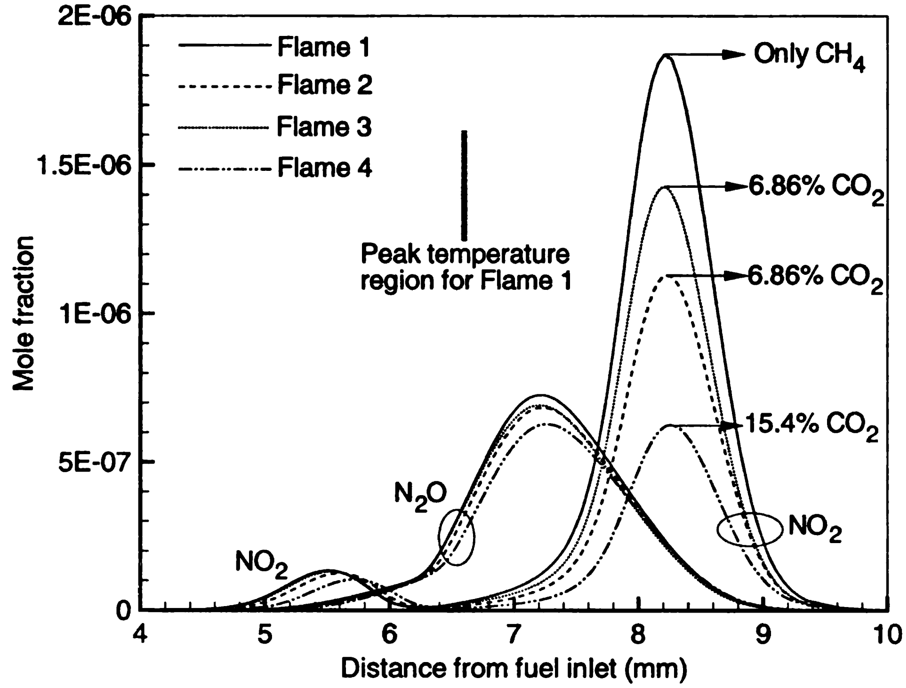

Figure 7-12. Comparison of the mole fractions of NO_2 and N_2O for Flames 1-4. The percentages of CO_2 in the fuel stream have been written.

increases (The NO_2 peak magnitude for Flame 4 is 33% of Flame 1). Chemical effects of CO_2 on NO_2 reduction are readily seen in the comparison of Flames 1 and 3. CO_2 dilution chemically influences the formation of nitrous oxide (N_2O); the peak of N_2O in Flame 1 is reduced by almost 5% when compared to Flame 3. As observed in Figure 7-12, the thermal effects of CO_2 addition on N_2O are less pronounced than they are for NO_2.

7.3.5. Greenhouse gas emissions

Three greenhouse gases are relevant to this study: carbon dioxide, methane, and nitrous oxide. According to EDGAR [153], CO_2, CH_4 and N_2O respectively account for 72%, 18% and 9% of the total Kyoto-Protocol greenhouse gas emissions. Landfill biogas contains methane, which has the potential to be produced naturally from biodegradable wastes (e.g. municipal solid wastes). The collection of biogas in landfills reduces the CH_4 release to the atmosphere.

Nitrous oxide (N_2O) is an important greenhouse gas. As seen in Figure 7-12, biogas use reduces N_2O emissions. Nitrous oxide is reduced by CO_2 dilution mainly due to its chemical effects (with only a weakly temperature-dependent influence).

Combustion-produced CO_2 is a source of environmental CO_2. We require a rational scale to identify whether burning a candidate fuel can potentially reduce the *net* CO_2 release to the atmosphere. Thus, we define a carbon dioxide emission index:

$$EICO_2 = \frac{m_{CO_2,emitted}}{m_{F,burned}}. \tag{7-1}$$

$EICO_2$ indicates the ratio of the *net* emitted mass of CO_2 leaving a combustor to the mass of fuel (here CH_4) burned. The *net* emitted mass of CO_2 can be found as $m_{CO_2,emitted} = (m_{CO_2})_{exhaust} - (m_{CO_2})_{inlet}$. For the counterflow configuration, the $EICO_2$ will be

$$EICO_2 = \frac{2\int_0^L \rho w_{CO_2} a_r dz - \dot{m}''_{CO_2,inlet}}{\dot{m}''_{CH_4,burned}} \tag{7-2}$$

where ρ is the gas mixture density, w_{CO_2} is the mass fraction of CO_2, a_r is the radial velocity gradient, and $\dot{m}''_{CO_2,inlet}$ and $\dot{m}''_{CH_4,burned}$ are the mass fluxes of CO_2 and CH_4 in the inlet fuel stream, respectively. For Flames 1-4, Table 2 lists $EICO_2$ and the calculated values of the inlet CO_2 mass flux ($\dot{m}''_{CO_2,inlet}$) as well as the exhaust CO_2 mass flux ($\dot{m}''_{CO_2,exhaust}$). As seen in Table 2, the exhaust CO_2 mass flux from Flame 1, which has no CO_2 addition, is 0.08 g/(cm^2-min). This amount is produced by the oxidation of CH_4 in Flame 1. With respect to Flame 3, adjustment of the boundary conditions of Flame 2 to increase its flame temperature changes the $EICO_2$ only very slightly from 0.415 to 0.411 (a 1% change). Flame 1, which contains pure CH_4, has the highest $EICO_2$ (0.469) whereas Flame 4, which utilizes landfill biogas (a low-quality biogas), shows the lowest value (0.352). Flames 2 and 3 (using a typical biogas from AD plants) lie in between.

Table 7-2. CO_2 exhaust and inlet mass fluxes, and $EICO_2$ for Flames 1-4*

	Flame 1	**Flame 2**†	**Flame 3**†	**Flame 4**§
Exhaust CO_2 mass flux ($g/(cm^2.min)$)	0.0801	0.3836	0.3862	0.7633
Inlet CO_2 mass flux ($g/(cm^2.min)$)	0	0.3127	0.3125	0.7032
$EICO_2$	0.469	0.415	0.411	0.352

*** Note that the temperatures of Flame 1 and Flame 3 are identical. Flames 2, 3, and 4 contain 6.9%, 6.9%, and 15.4% CO_2 in their fuel stream, respectively.**

† Typical compositions for biogas from anaerobic digestion (AD) plants.

§ Typical compositions for biogas from active or recently closed landfills.

$EICO_2$ can be used as an assessment tool to compare the *net* CO_2 release from the renewable fuel-based flames (Flames 2-4 burning biogas) versus the fossil fuel-based flame (Flame 1). Flame 1 utilizes pure CH_4 (similar to natural gas, considered as a fossil-based fuel) whereas all other flames burn biogas and produce a lower $EICO_2$. This suggests that burning the renewable fuel (biogas) by the combustion process reduces the *net* release of CO_2 as opposed to burning a fossil fuel (methane).

A final issue to mention is the *tradeoff* that exists between (1) biogas consumption rate and work associated with its compression; (2) flame temperature (heat release); (3) the reduction of greenhouse gases and NOx emissions. For example, a comparison of Flame 2 biogas from AD plants with Flame 4 landfill biogas reveals that a 2.5 % reduction in the flame temperature reduces $EICO_2$ by 15 %. However, Flame 4 has a 1.8× greater biogas mass flux than Flame 2. Figure 7-13 illustrates the tradeoff between three scaled quantities: peak flame temperatures, peak NO productions, and biogas mass flow rates. In a real-world application of biogas combustion, the reduction of GHG and NOx emissions, a possible increase of the compression work, and also a possible loss of heat release should be all taken into account. It should be noted that typical compositions for biogas from landfills and AD plants in this work are based on zero upgrading (i.e. a significant reduction of cost).

Similar kinetics studies on the flame structure of CO_2 diluted methane blends can be employed for biogas-fired fuel cells and CO_2 diluted oxy-fuel combustion as well as the EGR modeling for IC engines.

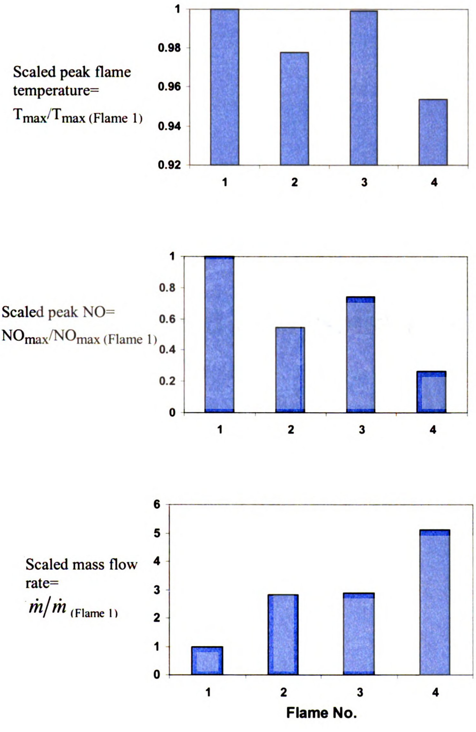

Figure 7-13. Tradeoff between scaled flame temperatures, scaled NO, and scaled mass flow rates for Flames 1-4.

Part III

Flame Spread over Solid Fuels in Microgravity

Chapter 8 Background and Introduction to Flame Spread in Microgravity Conditions

Flames that interact strongly with surfaces are by far the most prevalent both in nature and technology. They include attached burner flames in combustors, torches and heaters (industry), forest fires (nature), flames in rockets or missile combustion champers (space), and attached flames in fires and flame spread (safety) [154]. For several decades, the science of flame spread over solid materials has been of interest to researchers and professionals who have responsibility for fire safety including accident investigators, insurance companies, vehicle designers and building code authors. Flame spread is by nature complicated due to the coupled physical processes involved. In the flame spread literature, simplified theories and apparatuses for certain limiting cases and certain classifications (e.g., thermally thick vs. thin[*] materials) have been developed [155]. In a spreading flame, the flame and flow direction can assume any angle depending on the particular setup, but two flows are of dominant interest: (1) opposed flow, in which the direction of the oxygen flow is against the direction of flame spread; (2) concurrent flow, in which the flame advances in the direction of oxygen flow [156]. Concurrent flow is usually thought to be more hazardous since its gas phase forward heat transfer mechanism is convection (excluding radiation) with a much faster spread rate [157]. Much attention has been devoted to the study of both concurrent and opposed flow flame spread in the past decades [157]. The focus in this thesis is on *opposed flow* flame spread.

---

[*] In a thermally-thin surface the front and rear surface temperatures are nearly identical during heating.

A recent trend in this research is emphasis on the three dimensional structure of the spreading flames, although this limits many analyses to purely numerical work. Although models of flame spread have been developed for "generic" problems such as the "ideal vaporizing solid" (e.g., PMMA[*]) [158], it is well known that few materials burn in this way. Real materials regress, liquefy, and form spotty regions with various degrees of charring and liquefaction. Real materials are also heterogeneous mixtures (e.g., propellants) and their burning is extremely complicated as recent research demonstrates [159]. Real fires also spread over heterogeneous dissimilar materials.

For these reasons it is believed that before developing detailed 3-D solution codes, it is imperative to understand three things: (1) The "flame microstructure" which includes attachment characteristics, local reactivity, local temperature, enthalpy, species, reaction rate contours, and characteristic (time/length) scales. (2) The detailed heat and mass transfer responses of a surface during combustion. The detailed response includes the gas phase and it should produce an explanation of the basic structure of the flame attachment process and its requirements. (3) The reason why real flame spread at nearly all length scales is actually a 3-D (not 2-D) process. This requires performing actual 3-D analyses (which can be presently accomplished only numerically) and also examining the causes for the formation of 3-D flames (fires) from initial 2-D flames. The mathematical and numerical models examined in this Part attempt to address questions (1)-(3).

---

[*] Poly methyl methacrylate.

In the study of diffusion flames attached to surfaces, recent work by our research group at MSU, under the NASA project ATHINA* [160] has shown that complicated burning patterns can occur. Analyses of the phenomenon by our research group at MSU and NASA can be found in Refs. [155, 160]. A complicated "flamelet" form of flame spread has been reported, in which stable two-dimensional flame fronts break apart and form flamelet fronts, in which isolated individual and small 3-D "flame caps" spread over the surface, consuming the fuel as they generate a complicated burning pattern (See Figure 10-3). The reasons why the 2-D flame front eventually become unstable and fragment into irregular 3-D fronts will be addressed.

Many of these complications arise when the inflow rate of oxidizer is reduced [160]. However, it is clear that other influences, such as fuel thickness; fuel homogeneity and heterogeneity; fuel regression pattern; melt layer (or char layer) formation; volatile transport/reactivity in the gas; fluid-dynamical flow pattern near the surface; will all affect the flame structure. The reason is that flame spread over surfaces involves a complicated feedback process, in which the flame heats the surface, which decomposes to volatiles. These volatiles are transported by diffusion and convection into the gas leading to the formation of mixing layers and combustible gas mixtures, which facilitate reaction and transport of heat (thermal energy) to the solid fuel [158]. Flames over non-homogeneous fuels such as propellants can also show complicated surface burning behaviors, and these behaviors are only beginning to be studied [161].

---

* ATHINA stands for the NASA Microgravity Combustion project: "Analysis of Thermo-diffusive and Hydrodynamic Instabilities in Near-extinction Limit Atmospheres", started in January, 2003.

As elaborated before, the combustion of a solid fuel is an extremely complicated process. The goal of this research is to begin to understand this process in terms of simple descriptions that isolate key features and focus on their rigorous description, instead of trying to solve the entire problem at once. The approach taken here is to simplify the problem and to attempt to rigorously describe it.

In the flame spread model, the entire downstream surface is considered to gasify, as in all "classical" flame spread models [162, 163]. Long and co-workers at MSU [156, 164] examined a simplified 2-D mathematical model of classical flame spread over thin cellulosic fuels including both gas phase flow and solid phase degradation. The theoretical calculations were shown to be in excellent qualitative agreement with the numerical computations, suggesting that the physical features of such models are adequately characterized. All quantities important for the macroscopic and microscopic structure were found and analyzed. The diagnostic parameters can be used to examine flame structure for more complicated flame geometries.

We perform a numerical and theoretical study, in Chapter 9, for another kind of flame model in which the surface pyrolyzes over only a finite segment (or several segments) of fuel. This model describes (characterizes) flamelet formation and spread, flame burnout lengths [165] and heterogeneous materials [166], none of which support large and uniform flaming. Our theoretical and numerical study of flame spread over single and multiple fuel segments include an open environment. Simulations are conducted for zero gravity ($g = 0$) to mimic microgravity conditions although the flow in open environments on earth is strongly driven by buoyancy. Convective flows transporting volatiles and oxidizer are assumed to be weak in the theoretical models.

This research finally turns toward the study of flames forced to spread in a confined space, which has important implications for fire safety in normal gravity. In Chapter 10, we will examine the flame spread in narrow gaps, or rectangular channels. The fuel and flame are close to other surfaces resulting in large heat losses to the nearby walls. As a result, in narrow gaps, the flame becomes "near-limit". The designation "near-limit" in Part III indicates limiting conditions that weaken the flame including large heat loss or poor oxygen delivery (produced by a reduction of the oxygen inflow to levels low enough to starve the flame of oxygen). A motivation for our research is that "near-limit" conditions are achieved in the most deadly fires. One of these fires caused the crash of the 1998 Swissair Flight 111 into the Atlantic Ocean while attempting an emergency landing at Halifax International Airport. The crash killed all 229 passengers aboard [167]. A small, weak flame originated due to a wire arcing event in the cockpit slowly spread, driven by ventilation flows between the walls. This near-limit flame received a much greater airflow in the narrow gap after breaching a silicon vent cap, leading to a rapidly growing and spreading flame [155]. Other examples include flames in small gaps (in the presence of wire bundles or electronic equipments) or in regions where materials are in close proximity, such as inside a wall.

A new experimental apparatus, a Narrow Channel Apparatus, or NCA, has been built and tested at MSU and at NASA. The NCA allows well-controlled experiments to be conducted [155, 168]. The research at MSU using the NCA along with parallel efforts of our colleagues, Drs. Olson and Miller, at NASA [155] using drop tower experiments (actual microgravity conditions) and a NCA they constructed after MSU's original version [168] was designed to investigate whether the NCA is well suited to study flame spread in simulated microgravity. A scaling analysis is performed to determine the characteristic magnitudes of the various velocities that occur in the NCA. It will be shown that a NCA operating in normal gravity on earth can be used to test microgravity flame spread, which is an acknowledged space-fire hazard [169].

Chapter 9 Numerical and Analytical Study of Diffusion Flames Spreading near Solid Fuel Surfaces in Microgravity

Flame attachment to surfaces in problems such as spreading flames, fires, and surface-burning propellants is a complicated process. The flame heats the surface, which decomposes into volatiles, which leave the surface as the gaseous fuel that mixes with incoming oxidizer, feeding further combustion. Although classical flame spread models usually consider gasification over the entire downstream surface, in certain applications the burning of finite segments (one or more) of solid fuel is of practical significance. Much attention has been devoted to examining near surface diffusion flames analytically using simplified non-dimensional governing equations [170-172].

Heterogeneous combustion processes will produce interacting distributed flames, although little work has been done on this problem. Flame-flame interaction between single flames on parallel solid surfaces has been studied, but these works examine vertical surfaces in 1g conditions [173]. Rouvreau et al. [174] numerically simulated a microgravity diffusion flame of ethylene over a flat plate with the flow of oxidizer parallel to its surface using the Fire Dynamics Simulator (FDS) code. Their work, which has been compared to a detailed experimental study [175], examined in detail the influence of flow perturbations and the validity of the boundary-layer assumption based on the fuel injection velocity.

In this chapter, diffusion flames near solid fuel surfaces are investigated numerically and analytically in a 2-D planer domain. An attempt is made to describe 2-D flames, in which oxidizer is swept past a finite-size fuel-delivery segment (or segments) embedded in a non-combustible "binder" material. The goal is to determine whether such flames can resemble separate flamelets, one behind the other, or whether the combination of downstream combustion product gases and air vitiation produce conditions unsuitable for successive flamelets to survive. The "flamelet", as mentioned before, is an interesting flame shape appearing in narrow-channel combustion, microgravity combustion, and combustion over heterogeneous fuels.

The sensitivity of the 2-D model to the downstream conditions suggests that the actual localized flames and flamelets are likely to be 3-D. Nevertheless, the 2-D model may be used to achieve insight to the flame structure near the attachment region for single and multiple fuel segments.

To construct an analytical model of surface-attached solid fuel flames, a segment of fuel adjacent to an insulated, non-reactive binder material, and located in an infinite gas-phase environment, is examined. An exact analytical solution is derived for the mixture fraction equation when convective terms are discarded. In the next step, and to take into account the role of weak convective terms, the mathematical model is solved analytically and compared to numerical solutions. Numerical solutions of the Z (mixture fraction) equation are obtained for a finite-height channel with an Oseen flow (uniform streamwise velocity), with or without a constant transverse velocity. In the more complex case of multiple fuel segments, exact solutions for the Z equation are unattainable, whereas the numerical modeling is still applicable.

Comparisons are also made with the results of numerical modeling of a qualitatively similar problem using FLUENT, which includes a surface segment (or segments) of a gaseous hydrocarbon (not generated volatiles of a solid fuel at the pyrolyzation temperature) in a cross flow of air. The equations for conservation of mass, momentum, energy and species are solved. Since the gas phase is of principal interest, various inlet fuel and air velocities are considered. Results of analytical and numerical models are compared near the flame upstream leading edge (attachment region) and near the trailing edge, where the flame can reattach to the surface. The ultimate purpose of this study is to establish an analytical model to examine heat transfer, flame structure and reaction rate in flames attached to solid fuel surfaces, particularly surfaces with complex structure and flames that consist of many flame fragments, or flamelets.

9.1. Model Problem

In the model problem considered here the solid and gas interact through boundary conditions that render the gas phase non-isenthalpic. In other words, the gas loses enthalpy to the solid. Viewed simplistically, the energy lost from the burning gas phase flame is used to produce volatiles from the condensed fuel. Within this class of approximations there are simple models that have not yet been examined for flamelet spread. One of these models will be formulated here.

When the cold fuel is heated to the pyrolysis temperature as a result of heat transfer from the flame, the heated surface generates fuel vapor. The focus will be on the gas phase. Consider, therefore, a uniform source of fuel vapor that feeds the flame from an isolated surface segment. To produce a combustible mixture, the fuel vapors mix with the oxidizer, which exists either as: (1) a stationary-infinite source, or (2) enters the domain as a forced flow in a finite region. Our model problem examines the former case. In this model, the convective inflow velocities are negligible, thus the species equations can be simplified and analytical solutions can be derived. However, this is rare. When exact solutions cannot be derived, either simplified versions of the models can be solved approximately or numerical methods can be employed to develop solutions for such attached flames.

Two regions in particular are investigated: (1) The upstream flame leading edge near the front of the fuel segment; (2) The flame trailing edge where it can reattach to the surface downstream of the fuel inflow (blowing) segment. Theoretical and numerical investigations are conducted to examine various quantities in these and other regions.

9.2. 2-D theoretical model

To construct a theoretical model, a one-step, irreversible chemical reaction in the form $F + \nu O \rightarrow (1+\nu)P$ (mass basis) is considered for the gas phase. Here, P denotes the combustion products. The governing equations for the continuity of species are written with the assumption $\rho D = const.$ and Fick's law for mass diffusion [176]. The equations for the conservation of species are:

$$\frac{\partial Y_i}{\partial t} + u\frac{\partial Y_i}{\partial x} + v\frac{\partial Y_i}{\partial y} = D\nabla^2 Y_i - \nu_i r \quad , i=F, O \tag{9-1}$$

Here, $\nu_F = 1$ and $\nu_O = \nu$, and r is a source term pertaining to the reaction stoichiometry. Equations (9-1) can be combined to produce a single homogeneous equation for the mixture fraction, Z, which is defined as

$$Z = \frac{\nu Y_F + Y_{O\infty} - Y_O}{\nu Y_{FF} + Y_{O\infty}} \tag{9-2}$$

In this equation, Y_{FF} is the fuel mass fraction at the fuel inlet (the "pyrolyzing" surface segment) and $Y_{O\infty}$ is the oxygen mass fraction in the far field, which is the oxidizer source. The equation for Z is simply Eq. (9-1) without *r*, viz.

$$\frac{\partial Z}{\partial t}+u\frac{\partial Z}{\partial x}+v\frac{\partial Z}{\partial y}=D\nabla^2 Z. \tag{9-3}$$

At the flame the Z-value is given by (Y_F=Y_O=0)

$$Z_f=\frac{Y_{O\infty}}{\nu Y_{FF}+Y_{O\infty}}=\frac{1}{1+\nu Y_{FF}/Y_{O\infty}}, \tag{9-4}$$

where the subscript "*f*" denotes the values of Z at the flame sheet. The ratio $\tilde{\phi}=\nu Y_{FF}/Y_{O\infty}$ is defined as the stoichiometric index. The condition $Z_f=(1+\tilde{\phi})^{-1}$ locates the flame sheet, since Z=Z(x,y) and Z(x,y)=Z_f defines the mathematical relationship between the coordinates x,y when Z=Z_f.

The numerical method is a second order central difference scheme for the *x* and *y* directions. For Neuman boundary conditions near the wall ($\partial Z/\partial y$ = 0), a second order forward difference scheme is applied. The Alternate Direction Implicit (ADI) method with successive over-relaxation (SOR) is employed here as the iterative method. The numerical domain in non-dimensional space is 10x10 including 100x100 uniform grids.

9.2.1. Analytical solution of $\nabla^2 Z=0$

In the steady state, with zero bulk flow streamwise and transverse velocities (negligible convective terms), Eq. (9-3) reduces to the Laplace equation, $\nabla^2 Z=0$.

Figure 9-1 shows the boundary conditions for this problem. In the analytical solution, the length and width of the domain boundaries extend to infinity. The analytical solution is

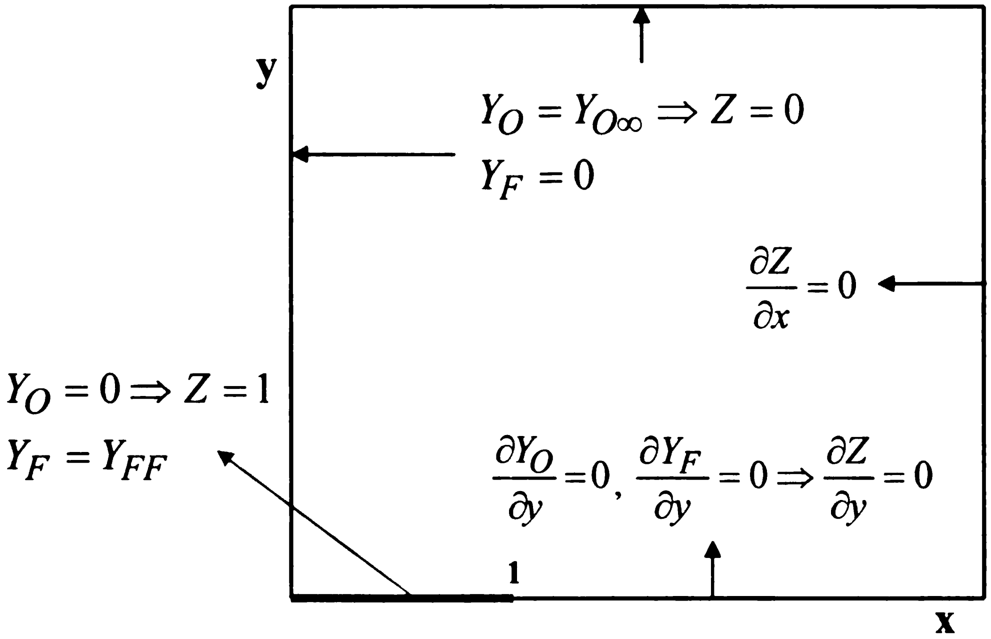

Figure 9-1. Boundary conditions for a single fuel segment to solve mixture fraction equation $\nabla^2 Z = 0$. The "fuel inflow segment" is shown in red. The rightmost boundary is for downstream (x→∞) and the topmost boundary is for transverse (y→∞).

$$Z_0 = \frac{2}{\pi} \tan^{-1}(\mu(x,y)), \tag{9-5}$$

where the subscript '0' denotes *zero convection.* μ is defined implicitly in the next equation. Lines with constant Z_0 values have μ=*constant.* At the flame sheet μ = $\tan(\pi Z_{0f}/2)$. The functional relation between coordinates x and y at the flame sheet is obtained by an algebraic calculation in which μ is an input parameter:

$$y^2 = \sqrt{(x^2 + \frac{1+\mu^2}{2})^2 + x^2(\frac{1+\mu^2}{\mu^2} - x^2)} - (x^2 + \frac{1+\mu^2}{2}) \tag{9-6}$$

The equation $\nabla^2 Z = 0$ can also be solved *numerically* subject to the boundary conditions shown in Figure 9-1. In the numerical solution, finite values must be assigned to the domain length and width, i.e., the topmost and the rightmost boundaries are now located a finite distance from the origin $x = y = 0$.

9.2.2. Numerical and analytical solution of $e(\partial Z / \partial x) + d(\partial Z / \partial y) = \nabla^2 Z$

Here, we assume that the convective terms in both streamwise (x) and transverse (y) directions are weak. Assuming steady state conditions and constant velocities in the x and y directions, the mixture fraction governing equation is

$$e(\partial Z / \partial x) + d(\partial Z / \partial y) = \nabla^2 Z \,, \tag{9-7}$$

where e denotes a uniform streamwise velocity (in the x-direction) and d indicates a constant transverse velocity (in the y direction). In the physical problem corresponding to actual flamelets, the fuel inflow (blowing) only occurs in the region $0 < x < 1$ (identical to the red region in Figure 9-1) and the transverse velocity v is identically zero in the region $x > 1$. Thus, the assumption of uniform v for all values of x in this simplified model is not in accordance with reality for flamelets. However, this model is employed in order to provide some physical insight to the study of flame shape. Let

$$Z = e^{Kx+Jy}\phi(x,y) \tag{9-8}$$

For the case $e \to 0$, $d \to 0$ and ϕ is an arbitrary function. It can be shown that the lowest order *approximate* analytical solution for Z is given by

$$Z = e^{(\frac{e}{2}x+\frac{d}{2}y)} Z_0 \tag{9-9}$$

The function Z_0 is the solution for the zero convection case (Eq. (9-5)). At the flame sheet, where $Z = Z_f$, the flame location is found by solving the equation

$$\mu = \tan\left[(\pi Z_f/2)\exp(-ex/2-dy/2)\right] \tag{9-10}$$

To find the flame sheet curves (lines of constant Z_f) Eq. (9-6) is used while the values of μ are deduced from Eq. (9-10).

9.3. Discussion: 2-D Theoretical model

A comparison of the numerical solution with the exact analytical solution of $\nabla^2 Z = 0$ in Figure 9-2 validates the numerical scheme used to solve the governing equation $\nabla^2 Z = 0$, especially for points close to the flame leading edge. This figure is the leading edge part of the 10x10 domain. Flame sheets for nine values of Z_f are shown in this figure. This figure demonstrates, however, that applying the far field boundary conditions at a finite distance from the origin produces the largest deviations between analytical and numerical results in the far field. This is to be expected.

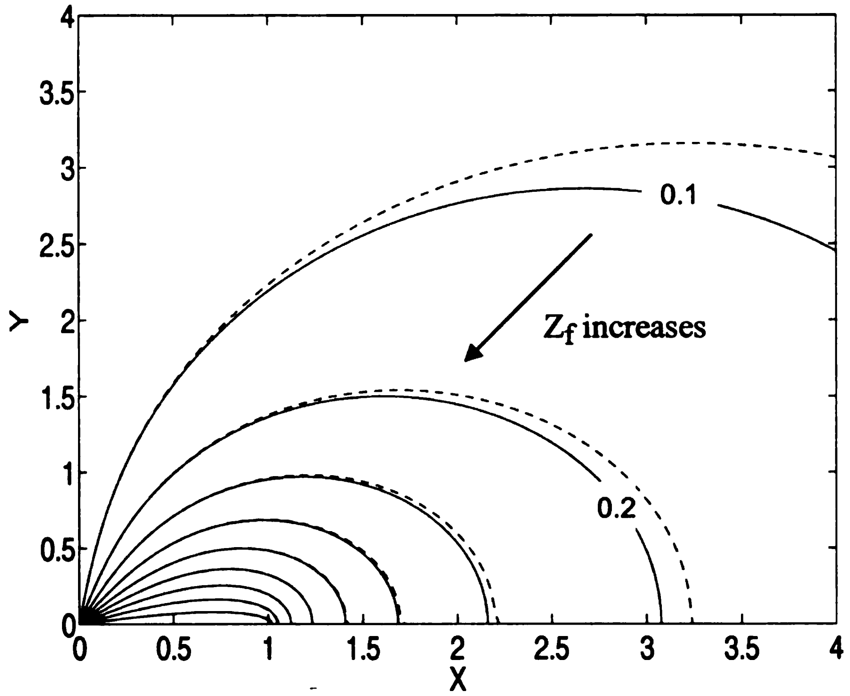

Figure 9-2. Comparison of numerical and exact analytical solutions of the equation $\nabla^2 Z = 0$ for $Z_f = 0.1$-0.9. (Solid line: numerical solution, Dashed line: exact analytical solution).

Figure 9-3 shows a comparison of the approximate analytical solution of Eq. (9-7) and its numerical solution for a zero transverse velocity (*d* = *0*). This figure implies that for values of Z_f near unity (which characterize flame sheets near the surface); the agreement of results is better. Moreover, near the upstream leading edge where x is small (the flame attachment region), the numerical and (approximate) analytical solutions show good agreement. Near the trailing edge, where the flame can, in principle, reattach to the surface, the (approximate) analytical solution does not predict a nearby reattachment point for low Z_f values, see $Z_f = 0.1$ in Figure 9-3. For other small values of Z_f a direct comparison shows that near the trailing edge the agreement of the (approximate) analytical solution with the numerical solution is often poor. Reattachment is not observed for larger values of e. The exponential term in Eq. (9-10) increases dramatically as x increases in the downstream direction.

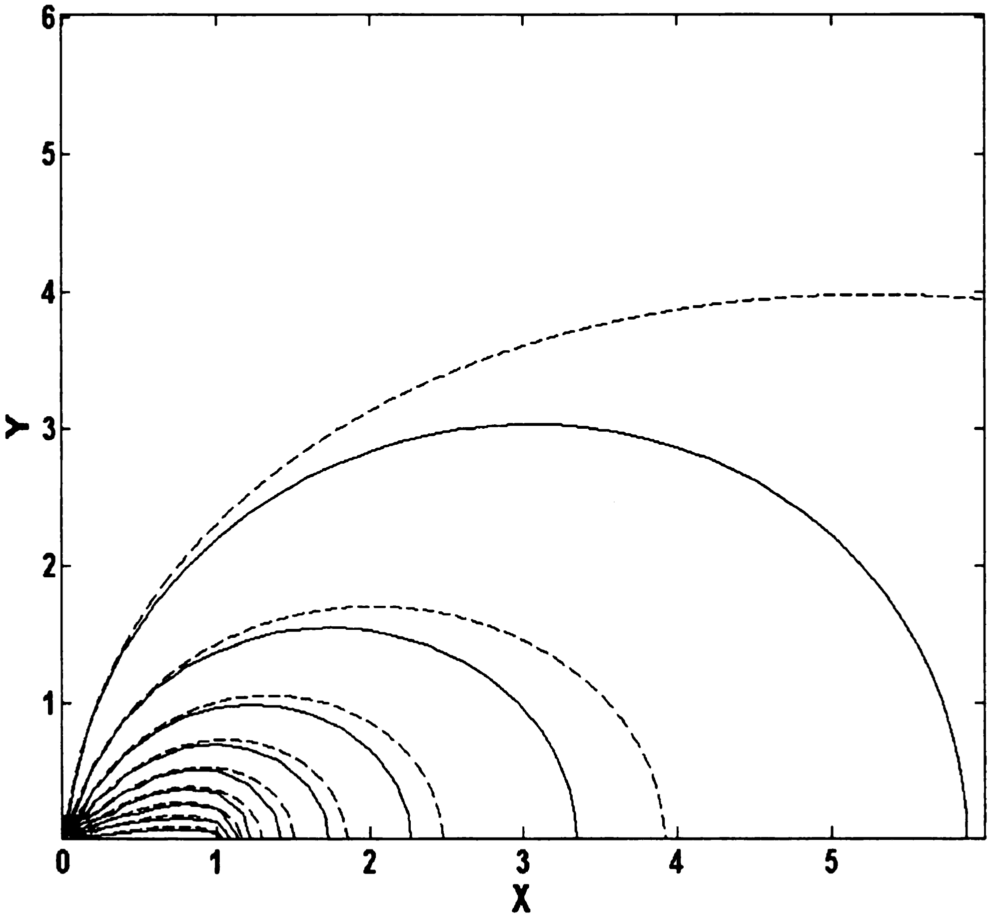

Figure 9-3. Comparison of approximate analytical solution and numerical solution of $e(\partial Z / \partial x) + d(\partial Z / \partial y) = \nabla^2 Z$ for $e = 0.1$ and $d = 0$. (Solid line: numerical solution; Dashed line: lowest order analytical solution given by Eq. (9-9)).

Figure 9-4 and Figure 9-5 give contours of Z_f for different streamwise and transverse velocities e, d. When $e = d = 0$, the curves are exactly similar to those of Figure 9-2. The red dashed line in Figure 9-4 represents the approximate analytical solution when $Z_f = 0.5$ (i.e. the stoichiometric index is unity). As illustrated in Figure 9-4, for small velocities, the approximate analytical solution and the numerical solution show good agreement, and both solutions can be employed to study the problem. The Z_f contours sweep to the right and shrink when e increases for fixed d (relevant figures not shown here). For large e-values, the approximate analytical solution is not applicable to solve Eq. (9-7) especially to predict the behavior in the trailing edge (larger x values).

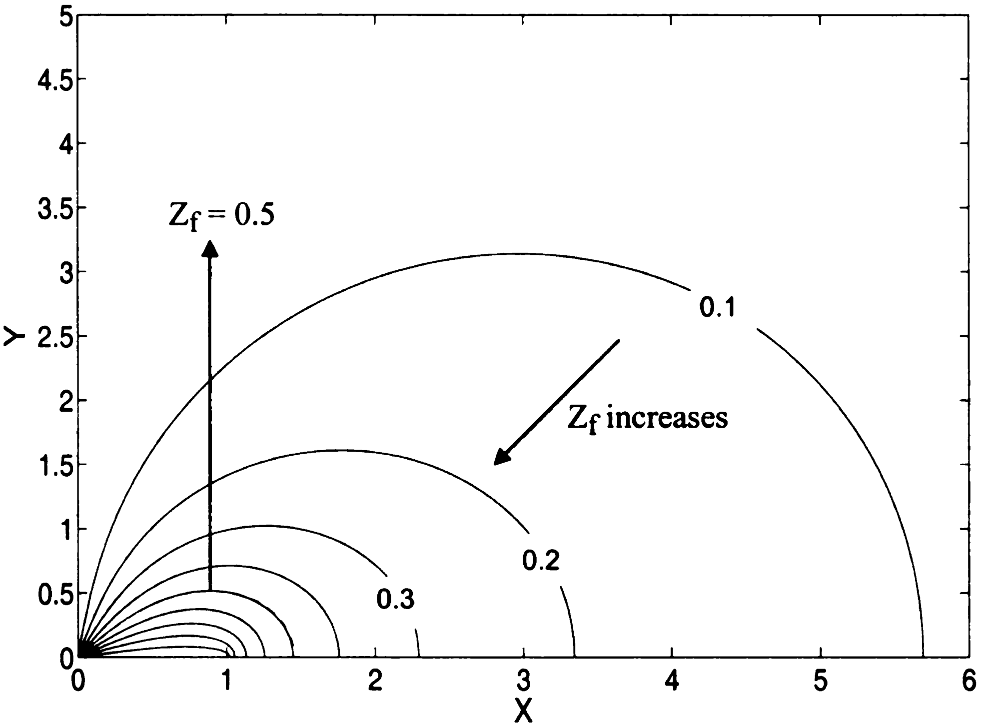

Figure 9-4. Contours of constant Z_f from the numerical solution of $e(\partial Z/\partial x) + d(\partial Z/\partial y) = \nabla^2 Z$ for $e = 0.05$, $d = 0.05$. Red dashed lines represent the approximate analytical solution for $Z_f = 0.5$.

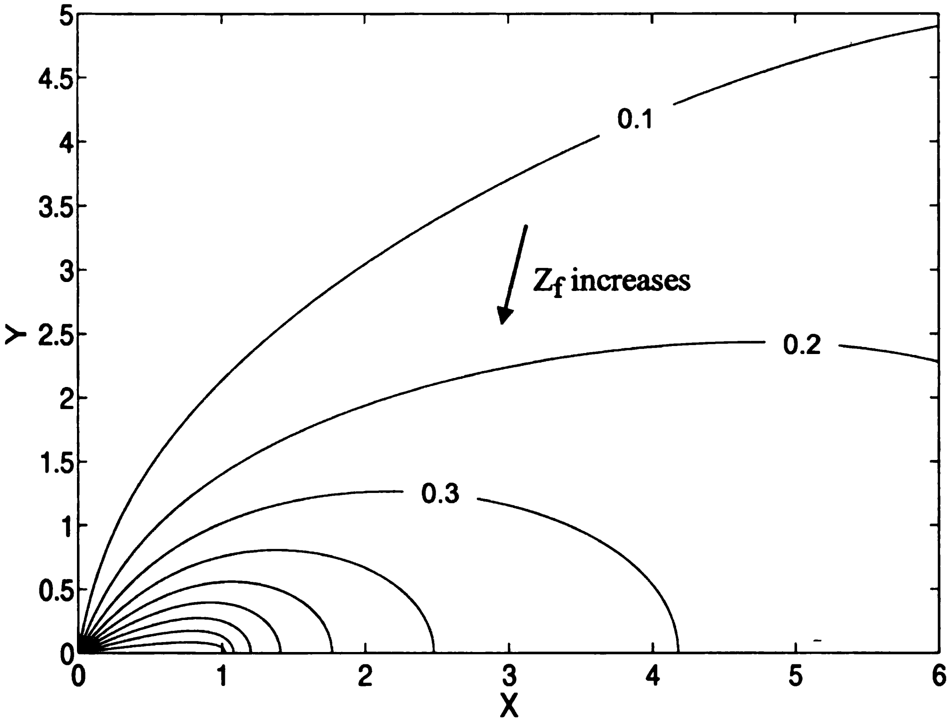

Figure 9-5. Contours of constant Z_f from the numerical solution of $e(\partial Z/\partial x)+d(\partial Z/\partial y)=\nabla^2 Z$ for $e = 0.8$, $d = 0.2$. Red dashed lines represent the approximate analytical solution for $Z_f = 0.5$.

9.4. Flame-Surface Interaction over Single and Multiple Solid Fuel Segments in a Channel Cross Flow

In solid fuel combustion, the surface heated by the flame decomposes to small volatile molecules. These molecules leave the surface and serve as gaseous fuel that mixes with incoming oxidizer. In the simplified model constructed to analyze the diffusion flame in the gas phase, a uniform inlet flow of a gaseous fuel ($Y_f = 1$) injected through the surface through one, two or three injection ports along the solid-gas interface represents the released volatiles. This numerical model is essentially a study of mixing and combustion of a fuel jet (or a series of jets) in a weak convective oxidizer crossflow.

In the model examined here, the incoming oxidizer is air ($Y_O=0.233$), which enters the channel at *5 cm/s*. The inflow Reynolds number is *630*, which ensures that the flow is laminar. Simulations are conducted using FLUENT version 6.2.16 [177], the mesh being developed in GAMBIT. The "cold" solution gives mixing and velocity contours without any reaction taking place. The flow is steady and the geometrical configuration of the computational domain is intended to mimic the domain of the theoretical solution except upstream of fuel inlet slot, where a 1 cm inert wall is placed. This 2-D computational domain with rectangular grids is illustrated in Figure 9-6.

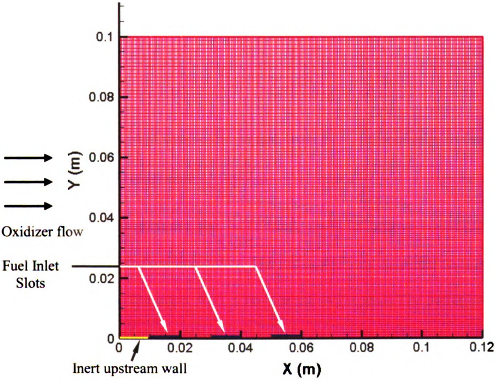

Figure 9-6. Schematic of the upstream section (12 cm x 10 cm) of computational domain with three 1 cm fuel inlet slots and 240 x 150 grids. Grid compression is applied in the y direction.

The gas phase flow field is computed using the finite volume SIMPLE-based scheme with under-relaxation techniques. The density is found by the incompressible ideal gas assumption (i.e. $\rho = f(T)$). The mixing law is applied to find the specific heat capacity. The thermal conductivity and viscosity are assumed constant. The constant dilution approximation is employed for the mass diffusivity. In this study, the fuel and oxidizer are ethane and air, respectively. A one step, second order, global gas-phase reaction is assumed that obeys Arrhenius kinetics. Zero gravity conditions are applied (g=0).

In the study of cross flow jets, a significant parameter that affects the flow field is the ratio of the jet to cross flow momentum, *r*, defined as

$$r = \left(\frac{\rho_j V_j^2}{\rho_{cf} V_{cf}^2}\right)^{1/2}, \qquad (9\text{-}11)$$

where subscripts j and cf denote the jet and cross flow, respectively. In the case of equal densities, Eq. (9-11) reduces to $r = V_j/V_{cf}$.

Boundary conditions: the isothermal, uniform inflow boundary condition is applied for the fuel and oxidizer inlets. The lower walls are insulated with zero fluxes and a no-slip condition. The upper wall is no-slip and isothermal. The outlet boundary uses a pressure outlet boundary condition.

The numerical model represents forced convective flow generated in a slow wind tunnel with finite dimensions in a realistic experiment (the *5 cm/s* flow speed is a typical flow speed in the MSU and NASA NCAs under "flamelet" conditions). The goal, as stated earlier, is to examine combustion for single and multiple streamwise fuel inlet segments. Using this model, the flame shape, mixing, and flow fields for three cases with lean, stoichiometic and rich conditions are numerically investigated. These cases use φ= *(0.5, 1, 1.7)*. In the fuel rich condition, the momentum ratio is $r = 1.025$, which decreases to *0.6* and *0.3* for stoichiometric and lean conditions, respectively. In simulations for two or three fuel segments, the fuel inflow temperature is taken to be *600 K*, which is close to a solid fuel decomposition temperature for a typical solid phase hydrocarbon fuel.

9.5. Discussion: Simulation for one fuel segment

Figure 9-7 to Figure 9-9 present temperature and oxygen mass fraction contours. For one fuel segment simulations, the fuel inflow temperature is taken to be *300 K*. As illustrated in these figures, $Y_O \approx 0$ underneath the flame as expected. Also, $Y_F \approx 0$ in the air above the flame. Comparison of Figure 9-7 to Figure 9-9 indicates that the flame moves downward toward the fuel surface for fuel lean conditions and it lies closest to the fuel surface in this condition. However, the global flame structure remains similar for all cases and does not vary significantly. The maximum flame temperature (T_f) occurs at a location where the flame sheet has a large curvature. The fuel inlet segment is located underneath this maximum T_f area.

At the flame leading edge, where the flame is attached to the surface, a comparison of theoretical and numerical results shows good agreement and either approach can be employed to predict the flame shape as well as the local concentration field. There are important differences, however, in the numerical model, the flame attachment point is in close proximity to the fuel inlet slot and attached to the *upstream* inert wall whereas it was located right at the fuel segment corner in the theoretical model. The numerical

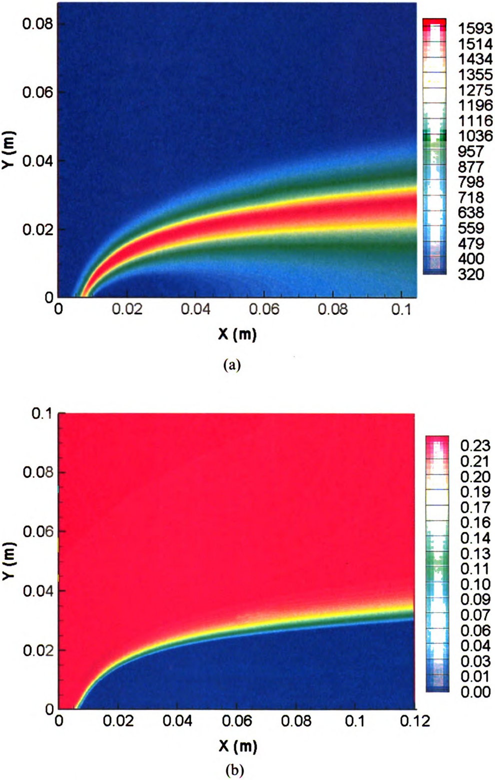

Figure 9-7. Contours of a) temperature and b) oxygen mass fraction in fuel rich conditions ($\varphi = 1.7$).

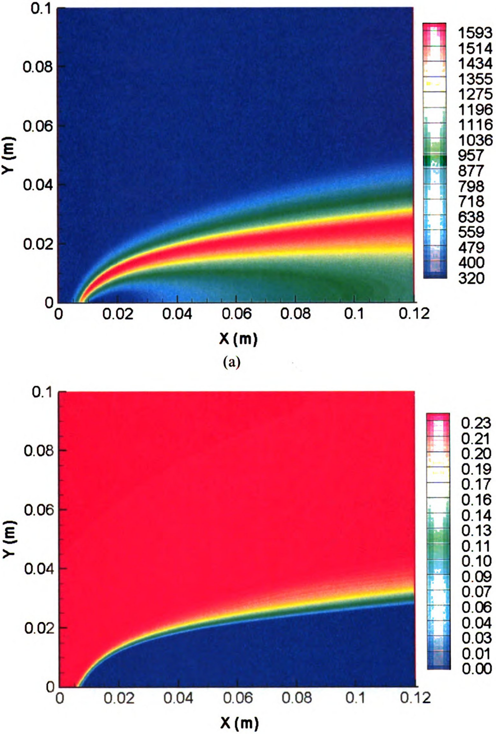

(a)

(b)

Figure 9-8 Contours of a) temperature and b) oxygen mass fraction in stoichiometric conditions ($\varphi = 1$).

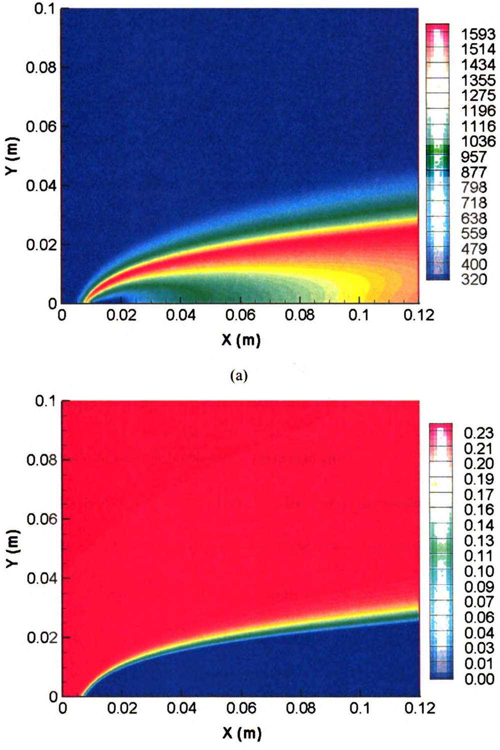

(a)

(b)

Figure 9-9 Contours of a) temperature and b) oxygen mass fraction in fuel lean conditions ($\varphi = 0.5$).

graphs show that near the trailing edge, the flame does not reattach to the surface. The agreement ranges widely and is often poor in this area.

This study demonstrates that theoretical predictions disagree in important features with numerical simulations. The suggestion is that the simulations are "sensitive" to certain quantities. Such a level of sensitivity suggests (but does not prove) instability.

The two-dimensional model, with its sensitivity to downstream conditions, suggests that a 2-D flamelet structure would be difficult to achieve in practice. The model examined here hints that the actual localized flames and flamelets attached to surfaces are more likely to be 3-D entities. This is, in fact, the case in laboratory experiments on flames in "near-limit" conditions, and it is also the case for flames observed over most propellants (see the extensive experimental analyses using advanced diagnostic techniques in [166]).

9.6. Discussion: Simulation for multiple fuel segments

Figure 9-10 shows the contours of oxidizer and fuel mass fractions near the flame leading edge. The simulations, just as for flame spread, show that $Y_O \approx 0$ underneath the flame and $Y_F \approx 0$ above the flame. The flame shifts downward and it lies closest to the fuel surface for the fuel lean condition. The flame structure remains the same for all three stoichiometries: its shape does not vary significantly. Similar to the previous case with one fuel inlet, the maximum T_f occurs above the fuel inlet slot, where the flame has a large curvature, in agreement with flame-spread results presented in our ASME publication [164].

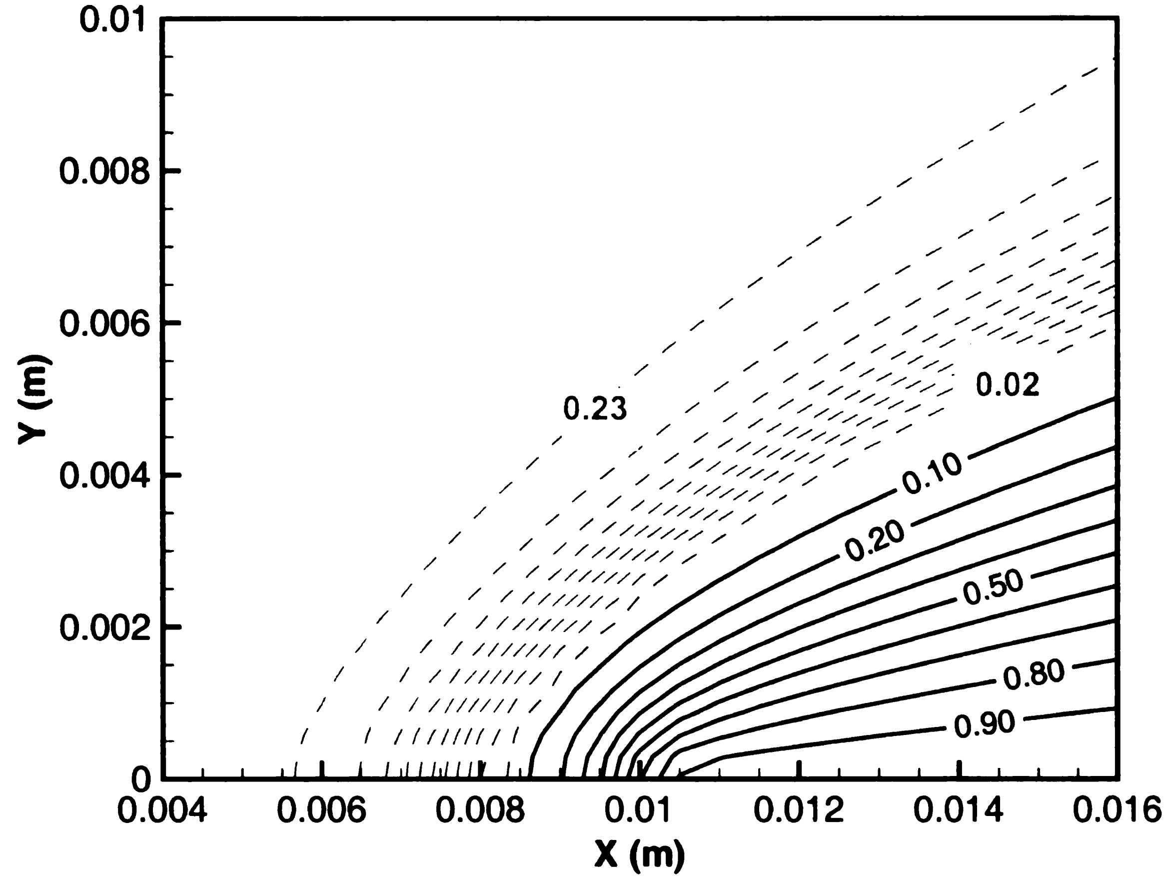

Figure 9-10. Y_O and Y_F contours near the leading edge (dotted line: oxidizer; solid line: fuel)

At the flame leading edge attachment point, both theoretical and numerical approaches can be employed to predict the flame shape and structure. However, near the flame trailing edge, the numerically-established flame *does not reattach* to the surface, being instead almost parallel to the wall. As illustrated in Figure 9-4 and Figure 9-5 for the approximate analytical solution with constant streamwise and transverse velocities, the flame trailing edge plunges towards the surface when the convective flow amplifies. A reattachment point in fact existed in those graphs, in direct contradiction with the present numerical simulations.

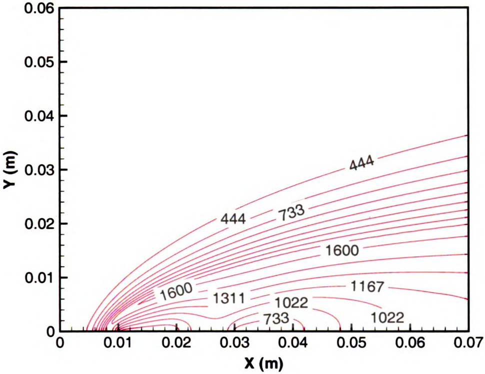

Figure 9-11. Temperature contours upstream of the flame for the case with *two* fuel inlet segments ($\varphi = 1$).

Figure 9-11 and Figure 9-12 illustrate contours of temperature for two and three fuel inlets, respectively. All cases here describe the stoichiometric condition ($\varphi = 1$).

Figure 9-13 presents reaction rate contours for the case with three fuel inlets. This figure shows that the maximum reaction rate is near the upstream fuel inlet. Product dispersion, observed in Figure 9-14, shows that product (here, CO_2) concentration field broadens toward the downstream.

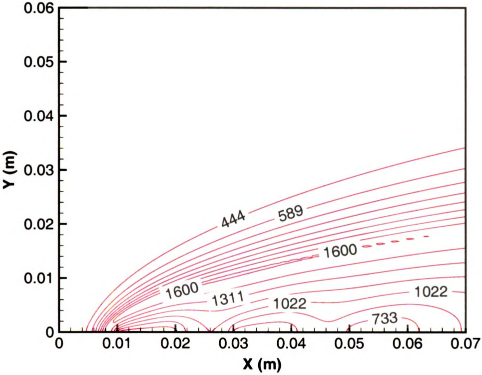

Figure 9-12. Temperature contours upstream of the flame for the case with *three* fuel inlet segments ($\varphi = 1$).

The study carried out here suggests: (1) The 2-D flame structure is unstable to minor changes in surface and far-field boundary conditions; (2) The flame-surface system with multiple fuel inlet segments in Section 9.6 can not resemble separate flamelets, one behind the other, displaying instead a single, attached flame. Separate flames cannot, it seems, exist directly downstream of one another unless the material contains its own oxidizer (e.g., propellants). Even for propellants the downstream flame(let)s must contend with passing product flow; (3) Multiple flames likely exist in the form of arrays in which individual flame fronts (flamelets) propagate toward the incoming oxidizer.

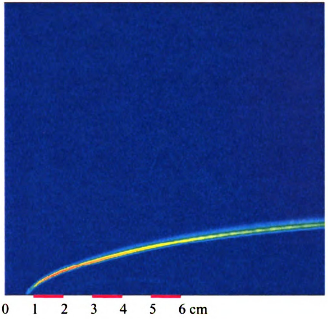

Figure 9-13 Reaction rate contours for the case with three fuel inlet segments ($\varphi = 1$).

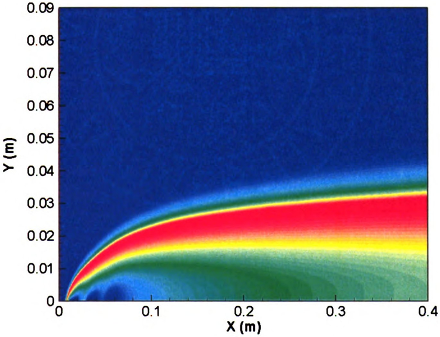

Figure 9-14. Product dispersion plot showing broadening of the CO_2 mass fraction ($\varphi = 1$). Three fuel inlet segments are employed (Figure is not to scale).

Unless the heterogeneous material contains oxidizer, the array is simply an advancing front [160]. In order to describe the burning of heterogeneous fuels and fuel/oxidizer mixtures, it is necessary to examine fully three-dimensional models.

Chapter 10 Flame and Flamelet Spread over Thin Fuels in Simulated Microgravity Conditions

Most previous research on flame spread over solid surfaces (e.g., Chapter 9) has examined flames in open areas. In this study, by contrast, the flame spreads in a narrow gap (e.g., the NCA), as occurs in fires behind walls or inside electronic equipment. This geometry leads to interesting flame behaviors not typically seen in open flame spread, and also reproduces some of the conditions experienced by microgravity flames.

Research groups at MSU and NASA have conducted two sets of experiments involving flame spread in a Narrow Channel Apparatus (NCA, available at MSU and NASA) in normal gravity, and the others taking place in actual microgravity in the NASA drop facilities. Three important variables are varied: oxygen concentration, flow velocity, and heat loss. Complete details of experiments in both facilities can be found in [155].

The research to be described in this chapter addresses flame and "flamelet" spread over thermally-thin fuels [160, 168, 178-182] in simulated reduced buoyancy conditions. When the oxidizer flow is reduced in the NCA, the initially uniform flame front becomes corrugated and breaks into separate flamelets. "Flamelets", as introduced before, are small, 3-D flame fragments that are formed when a wide, 2-D flame front weakens to the point where it can no longer be sustained, and breaks up into individual flames separated by distinct gaps of non-burning material [160]. This breakup behavior allows the flame to keep propagating below standard extinction limits by increasing the oxidizer transport to the flame, but has not been observed in other microgravity experiments due to the narrow samples employed. Breakup cannot be studied in typical (i.e., "open") normal gravity test facilities due to buoyancy-induced opposed flow velocities that are larger than the forced velocities in the flamelet regime.

In the experiments, *three contributors* to flamelet formation are varied. These contributors, which are controlling variables in real fires in confined spaces, are: (1) ambient oxygen concentration. Reducing the oxygen concentration weakens the flame, making it more susceptible to quenching; (2) the flow velocity of the incoming oxidizer. If the velocity is sufficiently high, the flame front is uniform. If it is too low, the flame may not receive sufficient oxygen for combustion [183]: at low enough flow rates it may break into flamelets or extinguish. Thus, flow velocity and oxygen concentration are related, in that each controls the amount of oxidizer reaching the flame, but in addition the flow contributes to convective heat loss from the flame; (3) heat loss to a nearby object. A metal or other substrate placed behind the thermally-thin test sample draws thermal energy, weakening the flame and making it more likely to fragment. A thick sample serves as its own heat sink by conducting heat into the interior of the solid.

Flamelets exist on the margins of flammability. The flamelet regime extends the range of material flammability to lower opposed flow velocities, lower oxygen concentrations, or higher heat loss by increasing the dimensionality of the flame (surface to volume ratio = S/V) and thus enhancing oxygen transport to the flame zone. Our colleagues, Drs. Olson and Miller, have evaluated the surface to volume ratio (S/V) for an ideal cylindrical flame (i.e. uniform flame) compared to the nearly spherical flamelets [155]. The increase in S/V ratio enhances the oxygen transport to the flamelets through the flame surface while focusing the heat release in a small volume, which then can provide sufficient heat flux to the unburned fuel beneath. This allows the flamelets to survive. They occur only under low oxygen flux conditions. Thus, the flamelet's multidimensional adaptation extends the material's flammability beyond the uniform flame extinction limit.

From a fire safety viewpoint, flamelets are by nature small and hard to detect, since they occur at the limits of extinction. They have been found for opposed flow and concurrent flow under similar low oxygen flow conditions [160]. They can persist indefinitely under the right conditions, and can flare up rapidly into a large fire when the environmental conditions become favorable. See Figure 10-1. It is standard practice on US spacecraft for the astronaut crew to turn off the ventilation to help with the extinguishment of a fire, both to eliminate the fresh oxygen supply and

Figure 10-1. A single flamelet (~6 mm wide) propagates steadily in an air flow of 0.5 cm/s in the NASA NCA. When the air flow is abruptly increased to 50 cm/s (100x), the flamelet grows 200% in less than 10 seconds. (Each photograph is 2 sec after the preceding one) [155].

to reduce the distribution of the smoke. If some tiny flamelets go undetected until the ventilation system is reactivated, the sudden increase in flow might allow the enduring flamelets to grow into a large fire very rapidly, posing a significant fire hazard.

In this chapter, the MSU NCA is briefly explained. A scaling analysis is carried out to determine the characteristic magnitudes of the various velocity sources in this NCA. The goal is to examine the suppression of buoyancy. It also aims at understanding the conditions under which flamelet phenomenon appears in experiments. Appendix B discusses the flammability maps generated from experimental data in the NCA and actual microgravity tests conducted in the NASA 5.18 second drop facility.

10.1. The Narrow Channel Apparatus (NCA) for normal gravity experiments

A Narrow Channel Apparatus (NCA) has been developed to study the phenomenon of flamelet spread in narrow gaps that have suppressed-buoyancy, high heat loss conditions [160, 168]. The NASA NCA, shown schematically in Figure 10-2a, reduces buoyant convection by limiting the channel vertical gap height (Figure 10-2b) to a value where vertical cellular flow caused by a hot source is small compared to the horizontal (streamwise) forced flow. This streamwise convective flow is forced through the duct at a controlled low speed between the copper bottom plate and the quartz top plate, with the sample held midway between the plates (Figure 10-2b). Tests can be done in either an upward facing orientation where the sample is viewed from above (quartz window on top, copper on the bottom), or the downward facing orientation, where the sample is viewed from below (copper on the top, quartz window on the bottom). Ignition occurs at a high flow (~ 20 cm/s), followed by a linear flow ramp down (~ 0.5 cm/s^2) to

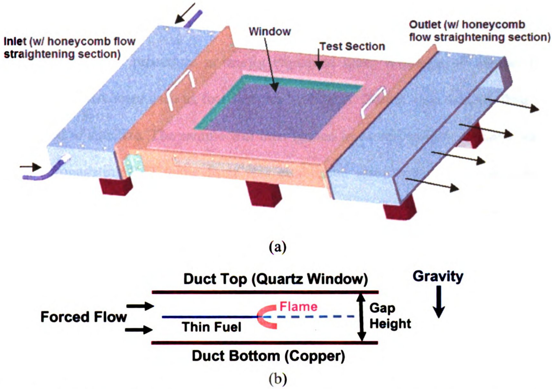

Figure 10-2. Schematic of the Narrow Channel Apparatus (NCA). a) Flow enters the left side through holes in the tube, and is distributed in the plenum section, straightened through screens and honeycomb, and then enters the test section. The flow exhausts from the right plenum. b) Side view of test section, showing the thin fuel suspended in the center of the narrow channel.

either a fixed flow for steady spreading at that flow, or a continuous very slow ramp down rate (~0.03 cm/s^2) until extinction occurs.

A color digital video image is recorded for each test, imaging through the quartz window onto the surface of the fuel sample. All video records from the normal gravity (upward facing or downward facing) and microgravity tests are analyzed. The analysis includes flame/flamelet spread rate, flamelet size, and burned fraction.

Microgravity experiments, conducted by our colleagues, Drs. Olson and Miller, in a low-speed wind tunnel drop rig [183] in the NASA Glenn Research Center's 5.18 second Zero Gravity Research Facility (ZGRF), are not reported in detail in this dissertation. The test procedure is briefly explained here. Whatman 44 ashless filter papers and PMMA were used as fuel samples by NASA. During each test, the flow was first allowed to stabilize. The sample was then ignited in normal gravity so that a stable, uniform, propagating 2-D flame front was established prior to the drop. Once stable flame propagation was observed and the flame spread away from the igniter (~5-10 seconds), the experiment package was released. Two on-board video cameras captured the flame before and during the drop, one from the side and one from the top. At the end of the drop, the chamber was evacuated to extinguish the flame.

10.2. Flame and flamelet spread in the NCA

Flames spreading across samples held in the center of the NCA (as shown in Figure 10-2b) break up into flamelets just as the microgravity flames described in [155]. However, we have time to observe the spread across the entire sample that took almost 250 seconds (4+ minutes) for the case shown in Figure 10-3, instead of only a few seconds as in the microgravity tests. For this test, the sample was ignited at 8 cm/s. The flow was ramped down to 4 cm/s at a rate of 0.5 cm/s^2 to reach the flamelet regime, followed by a slower ramp to 2 cm/s at the rate 0.03 cm/s^2. The flamelets continued to spread in the 2 cm/s air flow. As they approached the end of the sample, the air flow was quickly ramped back up (not shown) and the flamelets merged back into a single flame front. A gap spacing of 5 mm (i.e. h=1 cm in Figure 10-2b) on both sides of the sample was used to mimic the heat loss from the microgravity test in which a substrate at 2.5 mm existed on only one side of the sample.

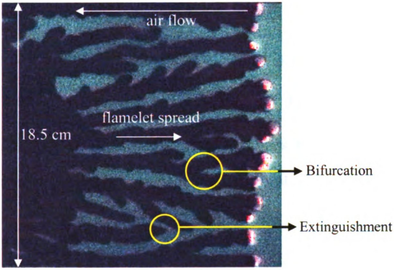

Figure 10-3. Flamelet tracks on the filter paper in the normal gravity NCA, illuminated with green LEDs. The uniform flame consumes the entire sample (black solid area at the left side of the image) and then breaks up into ~10 flamelets as the flow is reduced. The unburned paper between flamelets appears green, while the flamelet tracks are black. The flamelets are the luminous tips at the ends of the branching pattern [155]. The falmelet burned fraction is approximately 0.6.

As shown in Figure 10-3, some flamelets may bifurcate and some may extinguish. A detailed analysis has shown that there is extensive order in the seemingly random patterns [160, 179-182]. Olson and Miller's recent analysis [155] has also shown that the flamelet phenomenon is not an 'instability' consisting of a transitional state heading to extinction. Rather, the flamelet state is steady in terms of persistence, spread rate, fraction of sample burned, etc. Thus, the flamelet regimes in the flammability maps are a stable, near-limit, multidimensional flame adaptation to the limiting oxygen environment.

The flame and flamelet spread rates for the NCA (with *5 mm* gap) agree well with Zero Gravity Research Facility (ZGRF) data for a comparable *2.5 mm* substrate gap

[155]. Experiments with PMMA in the ZGRF showed that flamelets are not unique to cellulosic or charring fuels.

10.3. Velocity scaling analysis in Narrow Channel Apparatus

In the NCA, there are at least five velocities that can be used in a scaling analysis. As depicted in Figure 10-4, these are V_{flow}, V_{buoy}, V_{therm}, V_{diff}, and V_{blow}. Our scaling analysis evaluates the magnitudes of these characteristic velocities for typical NCA conditions. The scaling analysis is carried out by performing numerical simulations of narrow channel duct flows over short heated sections of the duct lower surface. These heated duct wall sections (we use $L = 0.5\ cm$ length of surface heated to 1500K) simulate the flamelets, see Figure 10-5. The strong local lower-wall heating produces thermal expansion and, in 1g, vertically directed buoyant flow. Our model does

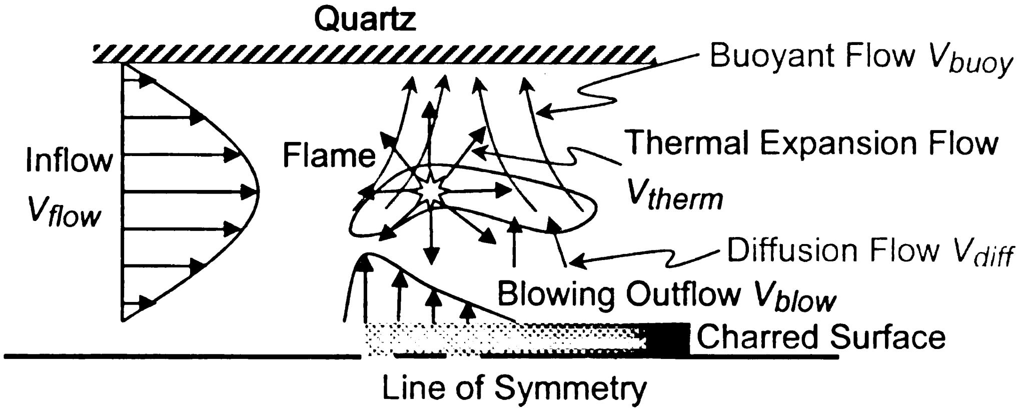

Figure 10-4. Definition of the various velocities that occur in the NCA. The sample is placed between top (quartz) and bottom walls. Inflow is left to right, while the flamelet moves right to left. In this figure, gravity vector points downward; buoyant velocity is upward.

not consider lower surface blowing (i.e., mass addition from thermal decomposition of the sample) although we estimate V_{blow} and V_{diff} using alternative methods. Three inflow speeds are used: $V_{flow} = (5,\ 10,\ 20)\ cm/s$. The simulations are 2-D, hence the duct is assumed infinitely wide. Simulations are conducted for *zero gravity* and *normal earth gravity*.

The simulation employs the FLUENT code, version 6.2.16 [177]. The inflow air enters the narrow channel *5 cm* upstream of the hot spot leading edge. The slug inflow velocity profile evolves into a parabolic profile before it reaches the hot spot. No-slip conditions are applied along the channel surfaces. The constant pressure outflow condition is applied at the channel exit *6 cm* downstream of the hot spot trailing edge. For the energy equation: the inflow has constant (ambient) temperature; the outflow has zero

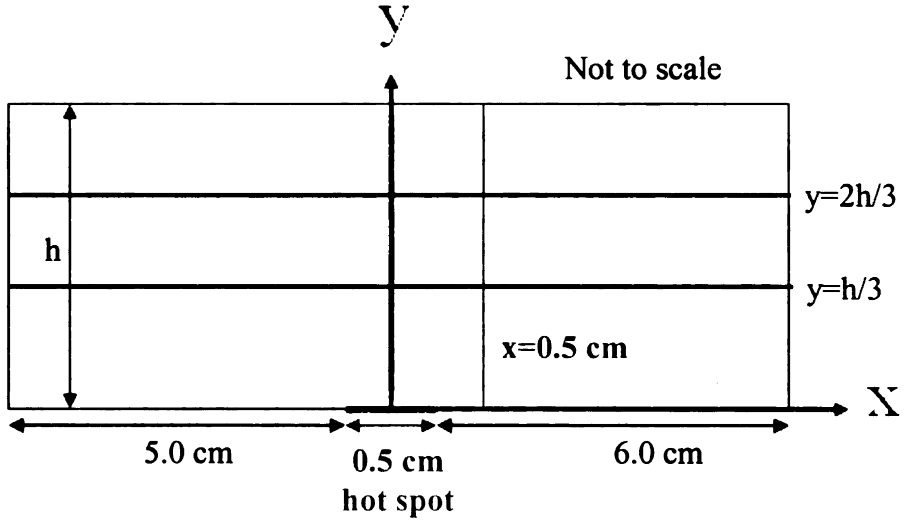

Figure 10-5. Schematic of geometry of numerical simulation used for velocity scale analysis. The channel height used was h=5 mm, and the hot spot was also 5 mm centered at x = 0 (the vertical (y) axis is located at x = 0). Flow velocity (5, 10, 20 cm/s) and gravity level (0g, 1g) were varied.

temperature gradient; the hot spot temperature is 1500K; the lower surfaces upstream and downstream of the hot spot are insulated; the top surface was insulated (zero normal gradient), except for a comparison test with constant temperature (300K). Under most flow conditions the differences caused by changing the top-surface boundary condition from T = 300K to zero heat flux (q''= 0) are negligible. As illustrated in Figure 10-6, for the lower-speed inflows the condition T = 300K changes the buoyant flow slightly. When

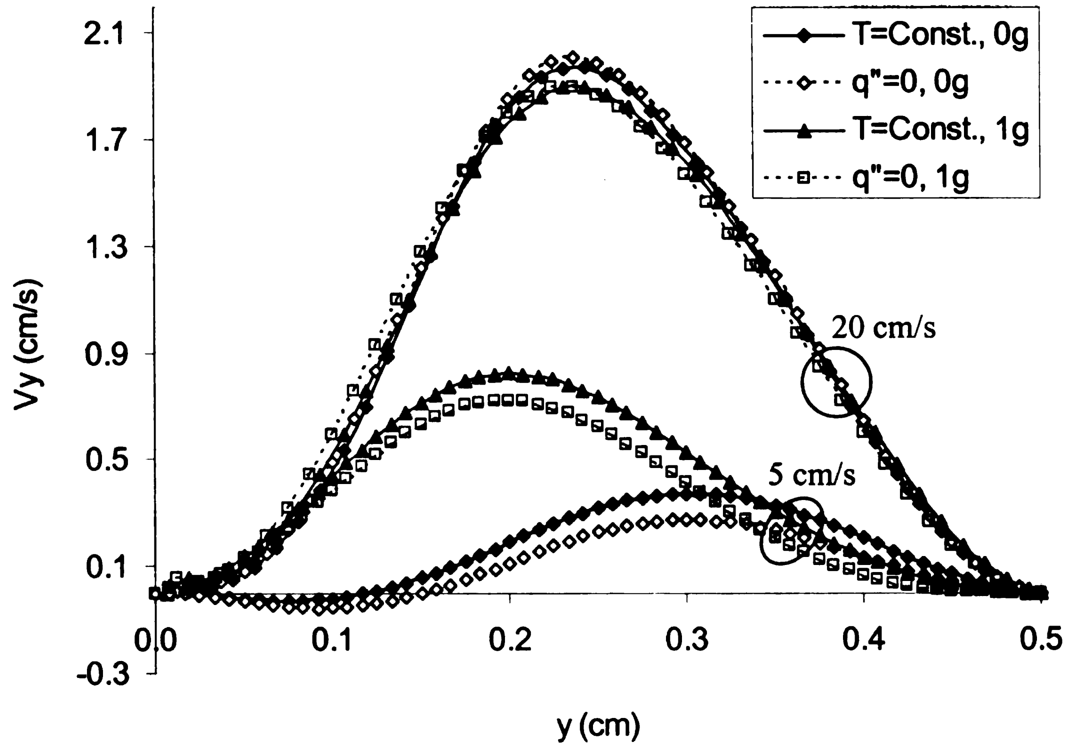

Figure 10-6. Numerical results for vertical velocity at $x=0$ for isothermal and adiabatic top wall boundary conditions under two inflow (forced flow) velocities: $V_{flow}= 5\ cm/s$ and $V_{flow}= 20\ cm/s$.

the inflow speed is higher (between *10-20 cm/s*) the difference in the flow fields between the two sets of boundary conditions is small (see Figure 10-6). Thus, we consider only $q''= 0$ at the top channel wall.

The characteristic magnitudes of V_{buoy} and V_{therm} are determined by comparing the velocity distributions for *zero* and ***normal gravity*** for identical values of V_{flow} and ***h***. The velocity distributions are evaluated along imaginary lines in the duct: two horizontal lines at ***(1/3)h*** and ***(2/3)h*** and two vertical lines located at the middle of the heated section simulating the flamelet ($x = 0$), and at $x = 2.5$ ***mm*** behind the downstream edge of the heated section, respectively. These locations are illustrated in Figure 10-5.

10.3.1. Results and discussion: Velocity scaling analysis in NCA

All surfaces except the heated section simulating the flamelet (T = 1500K) are insulated (q"= 0). Profiles of the heat flux ($-k\partial T/\partial Y$) along the heated surface (not shown here) delineate that the difference between the two gravity levels, 0g and 1g, for inflow velocities ≥10 cm/s is nearly negligible. The heat flux profiles (also called signatures) are valuable to determining how a solid material will heat up and can be eventually used to determine the ignition delay times.

Shown in Figure 10-7 is V_y as a function of x at $y = (1/3)h$; results at $y = (2/3)h$ are qualitatively similar. This figure shows that at zero gravity there is no downflow upstream of the flame, whereas at normal gravity there is a small downflow for the lowest value of the inflow velocity (*5 cm/s*); otherwise, there is not a substantial difference between normal and zero gravity profiles. The results also show that the largest and smallest values of V_y along these lines are always of greater magnitude for the higher flow velocity values. Although these extrema increase with V_{flow} the increase is not linear. The relationship is demonstrated for the zero-gravity case in Figure 10-8. The 2nd order fit through the data points yields a negative coefficient for the quadratic term. This indicates that as the forced flow is increased, it gradually overcomes the flow due to thermal expansion (since there is no buoyant flow in zero gravity). Note that the reason the thermal expansion velocity increases at all as the forced flow velocity is increased is because the heated section maintains a constant temperature. Hence, more thermal energy enters the flow as the velocity is increased.

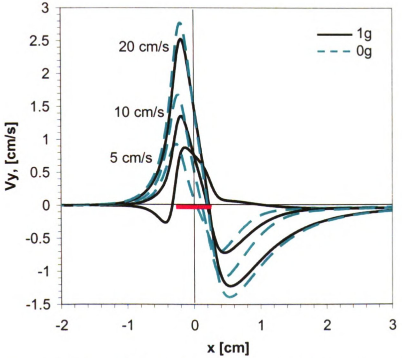

Figure 10-7. Numerical predictions of the vertical velocity component along the line $y = (1/3)h$ for three values of the inflow velocity at both normal and zero gravity.

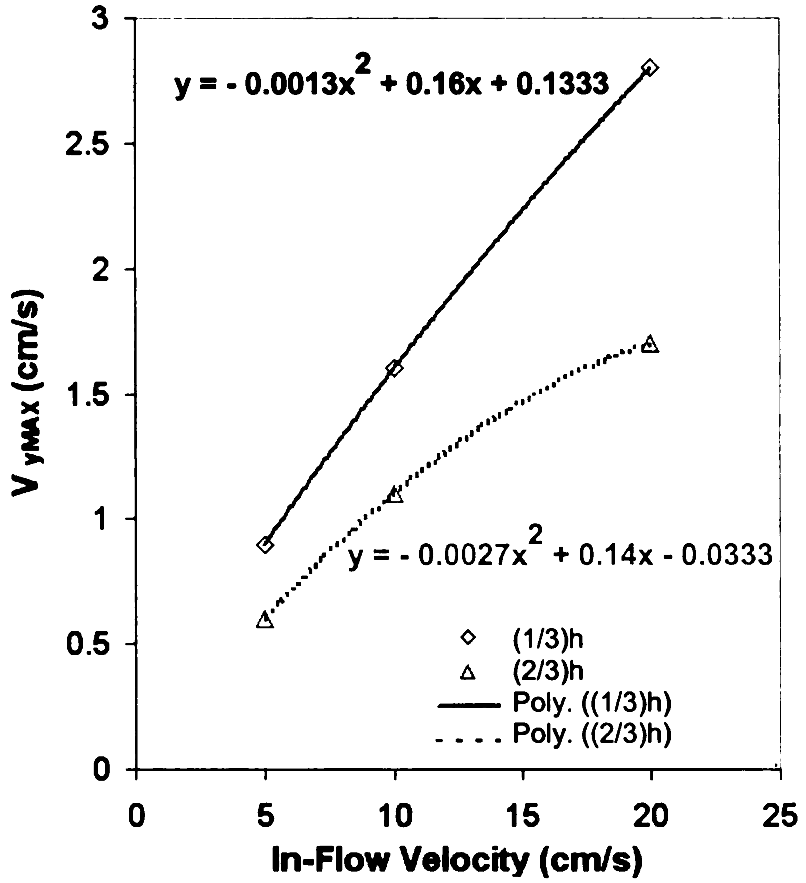

Figure 10-8. Maximum velocity for three values of the inflow velocity at $y = (1/3)h$ and $y = (2/3)h$ for zero gravity conditions.

Figure 10-9 shows the vertical version of Figure 10-7 at $x = 0$. The velocities are of the order of approximately *1 cm/s*. At $V_{flow} = 10$ and *20 cm/s* the normal and zero gravity vertical velocities are essentially identical, the maximum difference being ~ *0.2 cm/s*. At an inflow of *5 cm/s*, however, buoyancy plays a significant role and shifts the peak of the velocity to a lower height in the channel and raises the maximum value.

In Figure 10-10, the maximum and minimum V_y differences $[V_y(1g) - V_y(0g)]$ are examined along the line $y = (1/3)h$. The quantity $[V_y(1g) - V_y(0g)]$ in Figure 10-10 is

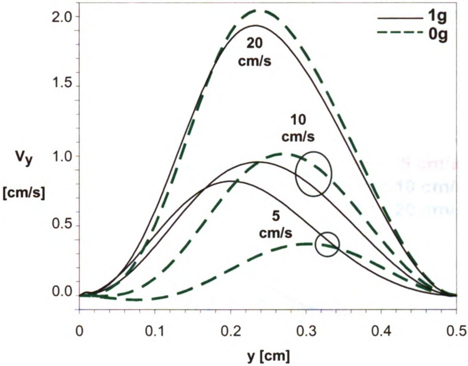

Figure 10-9. Numerical results of vertical velocity component for the six cases along a vertical slice centered above the hot spot at $x = 0$.

interpreted as the buoyant velocity. When $g = 0$ there is only thermal expansion: at normal gravity there is also buoyant flow. The magnitude of the buoyant velocity is larger at the lowest forced flow rate, and drops as the forced flow is increased. Negative values indicate the down-flow that is seen in the *1g* case ahead of the heated section.

The inset to Figure 10-10 shows the maximum and the minimum buoyant velocity as a function of forced flow, along with their difference. Here we note that the difference in the extrema approaches zero as the forced flow is increased. Contrasting Figure 10-8 and Figure 10-10, the thermal expansion velocity effect drops slowly as the forced flow velocity is increased, whereas the buoyant velocity drops more rapidly. At *10 cm/s* forced velocity, for instance, the maximum buoyant velocity is less than *1 cm/s*, while the maximum thermal expansion velocity is *1.5 cm/s*. Both are about 10% of the forced flow velocity.

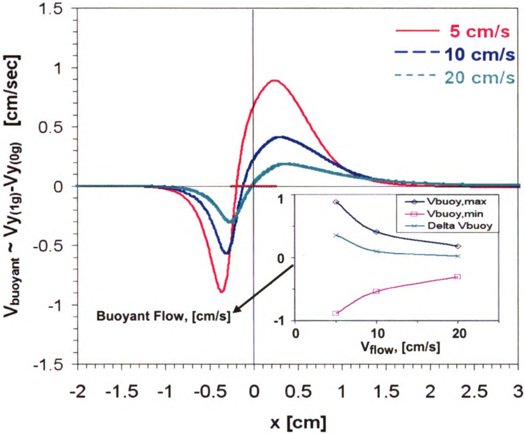

Figure 10-10. Numerical results of the buoyant velocity, calculated as the quantity $[V_y(1g) - V_y(0g)]$ along horizontal slice $y=(1/3)h$. Inset shows the trend in maximum buoyant flow as a function of forced flow.

For V_{blow} a different approach is used. Here, a Stefan flow is used to scale V_{blow}. First, we assume that $D_f \sim 0.3\ cm^2/s$ for a fuel vapor of moderate molecular weight at ~ $400\ ^oC$, a reasonable near-surface fuel temperature. Then, with $P_a = 1\ atm$ the fuel partial pressure gradient may be estimated as $(1\text{-}0)\ atm\ /\ 0.2\ cm = 5\ atm/cm$ using pure fuel at *1 atm* at the fuel surface that is totally consumed in the flame *2 mm* above the fuel. We find the result $V_{blow} \approx (D_f\ /P_a)dP_f\ /dy \sim (0.3/1)5 = 1.5\ cm/s$. Thus, V_{blow} is substantially smaller than, V_{flow}. For a V_{flow} value of approximately *10 cm/s*, V_{blow} is between 10-20% of this value.

It is also possible to evaluate V_{diff} in which constituents (e.g., oxygen) diffuse toward the flame. Here we use Fick's law: $V_{diff} = - D\partial Y_i/\partial x$. Putting $\partial Y_i/\partial x \sim (0.233 - 0)/(0.5\text{-}0) \sim 0.5\ cm^{-1}$ and multiplying by $D\sim 3\ cm^2/s$ (oxygen at flame temperature) gives $V_{diff}\sim 1.5\ cm/s$, which is of the same order of magnitude as V_{buoy} and V_{therm}.

These calculations suggest that when buoyancy is suppressed the other velocities are all of the same order of magnitude (e.g., 10-20% of the forced inflow velocity). When buoyancy is *not* suppressed, and the channel is not narrow, even though the forced inflow is reduced, V_{buoy} can become of the order of 30 cm/s [184]. This value is large enough to dominate these other velocities and to prevent the appearance of flamelets. This is the case in ordinary flame spread under standard 1g conditions. If, on the other hand, buoyancy is suppressed with a NCA, all of the velocities are of the same order of magnitude as the slow inflow rates. As a direct consequence the flamelet phenomenon occurs.

These results are in agreement with experiments of Olson and Miller [155] using a NCA in normal gravity and the NASA drop tower microgravity facility. The experiments confirmed that the NCA quantitatively captures the essential features of the microgravity tests for thin fuels in opposed flow. The NCA essentially suppresses buoyancy and serves to produce test conditions that can, to a satisfactory degree of accuracy, simulate the conditions achieved in actual microgravity. Under suppressed buoyancy conditions, a uniform flame front becomes corrugated and breaks into separate flamelets as the opposed flow is reduced. Flamelets were found under the same conditions in both the NASA drop facilities and in a NCA which suppresses normal gravity buoyancy. Good agreement was found between flame and flamelet spread rate and flamelet size between the two facilities. Experimentally-generated flammability maps (see Appendix B) constructed by Olson and Miller [155] delineate the uniform regime, the flamelet regime, and extinction limits for thin cellulose samples in microgravity and in the normal gravity NCA as a function of opposed flow velocity, heat loss, and oxygen concentration. The three regions representing (uniform) flame spread, flamelet spread and extinction generally agree over all classes of tests.

NASA's low gravity testing of spacecraft materials faces many limitations, including short test time and high cost. The short available test times in ground-based microgravity facilities make it difficult to study the flammability of thick materials or those of low flammability. The NCA, shown here to simulate microgravity conditions, provides an extremely long test time (of the order of minutes to tens of minutes) compared with the few-second time intervals available in ground-based drop facilities. Thus, the NCA provides a new method to study non-buoyant flame spread without the costs and limitations of actual low-gravity testing.

The applicability of the "buoyancy free" condition is not restricted to microgravity conditions. In fact, flame spread in tight gaps and narrow spaces is an important fire safety challenge in normal gravity conditions. In normal gravity, the flamelets are a fire hazard since they can persist in small gaps where they are hard to detect. When the air flow is increased, the flamelets can grow abruptly and generate a deadly fire.

Chapter 11 Conclusions

11.1. Conclusions: Jet fuel combustion

In Part I, combustion of jet fuel and jet fuel surrogates, which are blends of large molecular weight fuels with complex kinetics, was experimentally studied.

A well-defined baseline ethylene flame under incipiently sooting conditions was perturbed with the addition of 2000 ppm on a molar basis of either jet fuel or two jet fuel surrogates: 1) the six-component Utah/Yale surrogate that has previously shown good agreement for temperature profiles and extinction limits and has captured oxidation and pyrolysis trends of jet fuel in non-sooting diffusion flames; 2) the two-component Aachen surrogate that has been reported to mimic not only conditions of extinction and autoignition, but also to match the soot volume fraction behavior of jet fuel. In addition to attempting to validate the surrogate formulations with respect to the flame structure, a first experimental dataset for the pyrolysis and oxidation behavior of jet fuel in a diffusion flame at the onset of soot formation (incipient sooting conditions) is provided and can be used in parallel research efforts. The similarity in profiles of temperature, major species, and one minor species in all flames lends credence to the use of this perturbation approach to treat the flame as a flow reactor, with virtually identical conditions, except, of course, for the imposed perturbation. Principal conclusions follow for this part of the research.

The data for C7-C12 alkanes in Chapter 4 are consistent with the typical decomposition pattern for large alkanes with both surrogates showing reasonably good qualitative agreement with jet fuel in their pyrolysis trends. More quantitative agreement is difficult to achieve, because of the complex chromatograms of jet fuel with overlapping peaks due to isomerism.

Olefins are formed as the fuel alkanes decompose. Both jet fuel and surrogate doped flames show good agreement in their 1-pentene profiles. The agreement with respect to 1-hexene, on the other hand, is relatively poor with the Utah/Yale surrogate-doped flame and the Aachen surrogate-doped flame having concentrations a factor of 2.7 and almost 1.5 larger than jet fuel-doped flame, respectively. The agreement improves for smaller alkenes, such as propene, probably because the specific details of the fuel alkane structure are less important since many pathways can produce the smaller intermediates.

The concern in terms of significant aromatics discrepancy between jet fuel and the Utah/Yale surrogate that was reported for non-sooting flames in a previous study at Yale are not applicable in the present, and more relevant, situation of incipient sooting. In fact, good agreement was found between the jet fuel-doped and the surrogate-doped flames with respect to the location and magnitude of the benzene mole fraction peak, with the Aachen surrogate performing slightly worse and producing about 20 % less benzene than the others. Comparison of toluene mole fractions shows also reasonably good agreement between flames, with the Aachen surrogate still underperforming and underpredicting the peak magnitude by almost 30 %. Nevertheless, the somewhat worse, but still adequate, performance of the Aachen surrogate is compensated by its simplicity, since it consists of only two components as compared to the six components of the Utah/Yale surrogate.

Acetylene presents a unique behavior with peak concentrations nearly 19 times larger than in the previously studied non-sooting methane flames, as expected, since acetylene is a major contributor to soot formation. Furthermore, the profiles show a multimodal behavior, with a first local minimum that may be attributable to acetylene participation in the formation of soot precursors such as benzene and other large pyrolysis products, and a subsequent local minimum, which may be the result of its participation in surface growth of soot particles.

The influence of trace amounts of sulfur compounds in jet fuel or in the antistatic additives on the formation of soot precursors was examined. No distinct changes in the soot zone luminosity and thickness were observed, which suggests that the observed trends in terms of soot and soot precursors are not an artifact associated with the antistatic additive.

11.2. Recommendations and future work: Jet fuel combustion

Recommendations for the future work on jet fuel and jet fuel surrogate research are presented in a point form below:

1- Other surrogate candidates (e.g., MURI teams, SERDP) and their individual components can be examined systematically.

2- To the knowledge of the author, there exist no studies on the detailed chemical structure of F-T jet fuel flames. Moreover, surrogate formulations for F-T fuels have not been studied as comprehensively as JP-8 or Jet A surrogates. When these alternative fuels are commercialized, a daunting challenge will emerge: The need for proper (more complete) surrogate formulations with subsequent compilation of detailed reaction mechanisms from available (if available for *iso*-paraffinic components) mechanisms for surrogate components. F-T jet fuels and their surrogates can be systematically studied without a need to significant changes in the experimental procedure used in this work.

3- Preliminary computational predictions of the surrogate-doped ethylene flames by Professor Smooke at Yale did not show an acceptable agreement with experiments. The chemical kinetic mechanism in the computational model should be fine-tuned to improve agreement with experiments.

4- For guidance in the chemical analysis, sensitivity tests in the chemical kinetic model can be applied. Once more important species are realized, calibration curves are found for quantification of these species.

5- Specifically for the evaluation of acetylene profiles, Laser-induced Incandescence (LII) to measure soot volume fractions can be utilized.

6- Similar work can be performed at high pressures (up to 40 atm). A high pressure counterflow setup has been recently constructed at Yale. The GC/MS setup should be modified in such a way to make the sample loops portable for collection of gaseous samples from the high-pressure counterflow burner.

7- A reduced kinetics strategy can be implemented for both the Utah/Yale and the Aachen surrogates.

11.3. Conclusions: Biogas combustion and kinetics

The main conclusions of the technical research carried out in Part II on biogas combustion and chemical kinetic modeling are summarized below.

1) Biogas, produced from anaerobic digestion of biodegradable materials such as agricultural and municipal wastes, is presently a viable alternative fuel (e.g., for gas

turbines). It has principal chemical constituents CH_4, CO_2, N_2, and can be saturated with water vapor.

2) A laminar counterflow diffusion flame, as a fluid-dynamically simple configuration that intrinsically couples both chemistry and transport, was used in Chapter 6 to evaluate three reaction mechanisms and to understand thermo-chemical effects of each component. Both detailed mechanisms (GRI-Mech 3.0 and San Diego) give very close quantitative results. The GRI-Mech 1.2 reduced mechanism overpredicts the concentration of some minor species such as H radicals (important for chain branching reactions) although it satisfactorily predicts flame temperatures.

3) In Chapter 6, combustion characteristics such as equilibrium state properties, ignition delay times, and laminar flame speeds were investigated and characterized for blends of air premixed with diluted methane simulating biogas using a systematic chemical kinetics study and GRI-Mech 3.0 detailed kinetics mechanism. Correlations were found to predict the behavior of individual diluents (e.g., CO_2 or N_2) in a simulated biogas.

4) Detailed kinetic modeling yields to a comprehensive knowledge about chemical effects of CO_2, N_2, and H_2O addition to a methane gas. Besides chemical effects, each component in a fuel blend possesses thermal and transport effects as well as radiative effects.

5) The thermal and chemical structure of simulated biogas in diffusion flames was studied in Chapter 7. The numerical procedure allows quantitative comparison of the

chemical and thermal effects of the CO_2 content of biogas. Quantification of the chemical influences of biogas CO_2 content is vital because CO_2 dilution was shown to reduce soot precursors, NOx emissions, and greenhouse gas emissions even when flame temperature reduction is not feasible. The biogas, simulated as a CH_4-CO_2 mixture, is highly diluted with N_2 in the fuel stream. Four flames with nearly identical strain rates and stoichiometric mixture fractions are considered. These flames (Flames 1-4) have CO_2 mole fractions 0, 0.069, and 0.15, respectively. The boundary conditions for one of the biogas flames (Flame 3) are adjusted in order to ensure indistinguishable temperature profiles between that flame and the pure CH_4 flame (Flame 1). The principal conclusions of the research presented in Chapter 7 are:

5-1) As discussed in Section 7.2 the reduced mechanism with 22 species and 104 reactions fails to perform adequately for the chemical kinetics study of the biogas diffusion flame because it poorly tracks the minor species and chain branching radicals important in the detailed study of a simulated biogas.

5-2) The CO_2 dilution reduces the concentrations of H, OH, and O radicals. The thermal effects of CO_2 dilution on H, O, and OH radicals are nearly the same, whereas for H radicals, chemical influences predominate. The direct chemical effect of CO_2 on the concentration of CH_3 radicals is modest compared to its thermal effect. However, chemical effects of CO_2 are more pronounced for some intermediate species such as

CH_2O. The Flame 3 biogas (61%CH_4-39%CO_2) reduces the CH radical concentration suggesting a possible reduction of prompt NO.

5-3) The reduction in the peak of acetylene, an important soot precursor and surface growth species, suggests that biogas may be beneficial for soot suppression.

5-4) The NO profile shows a trend similar to the NO_2 profile with a significant decrease in peak values when CO_2 increases, even with the same temperature distributions. A typical AD plant biogas (Flame 3) having a flame temperature nearly identical to a pure CH_4 gas (in Flame 1) can reduce NO and NO_2 peaks by about 25% although it needs a mass flow rate almost 3× greater than the pure CH_4 flame. The NO and NO_2 mole fractions are reduced through both thermal and chemical effects. The thermal and chemical influences of CO_2 dilution on NO are nearly of the same order. However, it is demonstrated in the comparison of Flames 1 and 3 that the chemical influences of CO_2 slightly dominate the reduction of NO_2.

5-5) Biogas utilization reduces the net release of three green house gases (GHG): CO_2, CH_4, and N_2O. Burning CH_4, which is a very strong green house gas, prevents its release to atmosphere in landfills. A carbon dioxide emission index, $EICO_2$, is defined, which quantifies the ratio of the net emitted mass of CO_2 that leaves a counterflow domain to the mass of CH_4 burned. Flame 1, which utilizes pure CH_4, has the highest $EICO_2$ whereas the low quality landfill biogas Flame 4 shows the lowest value.

Contrasting four flames suggests that burning the renewable biogas fuel by the combustion process reduces the net release of CO_2 as opposed to burning a fossil fuel (methane or natural gas). Also, two different biogas compositions are compared; with a 2.5 % reduction in the flame temperature, the $EICO_2$ reduces by 15 % indicating that the relative release of CO_2 to atmosphere can be reduced with a slight diminishment of the heat release. The use of biogas reduces emissions of nitrous oxide (N_2O) mainly due to the chemical effects of CO_2 with only a weakly temperature-dependent influence.

5-6) The biogas mass flux is correlated to its consumption rate and the work associated with compression of biogas. Comparison of these flames suggests that in a practical design of biogas-driven combustors, a tradeoff between three factors emerges: the flame temperature, the biogas mass flow rate (and thus the required compression work), and the possible reduction of greenhouse gas emissions, and of NOx emissions and soot precursors.

6) Similar kinetics studies on the flame structure of CO_2 diluted methane blends can be employed for biogas-fired fuel cells and CO_2 diluted oxy-fuel combustion as well as the EGR modeling for IC engines.

11.4. Recommendations and future work: Biogas combustion and kinetics

Biogas chemistry is highly non-linear in the oxidation zone; however, scaling analysis, although rare in the context of chemical kinetics, can provide qualitative correlations to predict the biogas combustion behavior. More work is planned in the future study on scaling analysis along the lines of Section 6.4.

A complete sensitivity analysis to the heats of formation and reaction rates can be conducted for all reactions involving H_2O, CO_2 and N_2. This provides information to indicate the most responsible reactions for the chemical effects of each diluent in a simulated biogas.

Preliminary kinetic modeling of simulated biogas in a Well-Stirred Reactor (WSR) was performed, but not reported in this thesis, to study lean premixed biogas combustion. A WSR setup is being developed at MSU for subsequent validation of this kinetic modeling.

Large-scale gas turbine tests with real biogas fuels give qualitative suggestions especially to reduce emissions by modifications in turbine configuration and biogas compositions. Combustion instabilities in large-scale gas turbines utilizing a wide range of biogas compositions can also be investigated.

11.5. Conclusions: Flame Spread in Microgravity

In Part III, microgravity flame spread over solid fuels was investigated in collaboration with NASA Glenn Research Center. Diffusion flames near solid fuel surfaces were investigated numerically and analytically in two environments, namely, an "open" environment and a "confined near-limit" environment.

In Chapter 9, Surface-attached solid fuel flames in open environments were studied theoretically and numerically considering weak convection. An exact analytical solution was written for the mixture fraction equation ($\nabla^2 Z = 0$) when convective terms were considered negligible. This equation was also solved numerically and results were compared to the exact analytical solution to establish an applicable numerical scheme for weak convective flows. To take into account the role of the weak convective terms, a simple mathematical model was then solved both numerically and analytically.

Comparisons were made with the results of numerical modeling for a qualitatively similar problem in which a uniform inflow (or inflows) of a gaseous hydrocarbon from a surface segment (or segments) is issuing in a cross flow of air. Since the gas phase is of interest, various equivalence ratios were considered corresponding to various fuel inlet velocities. Near the flame upstream leading edge (attachment region), the results of the analytical and numerical models demonstrate strong agreement. Near the trailing edge, where the flame can reattach to the surface, the agreement is often poor; the flame simulated numerically stands nearly parallel to the surface and does not reattach to it. For the 2-D case, multiple fuel segments (slots) were subjected to a preliminary examination in order to mimic flames that consist of many consecutive fragments (flamelets). An interesting aspect of the multiple segments with fuel injection is the absence of significant reactant mixing prior to the reaction-rate maximum.

Perhaps the most important long-term impact of the research on flame and flamelet spread in a confined space (as conducted in Chapter 10) addresses the fire safety implications of flames and flamelets in narrow spaces in which combustible materials are placed in both close proximity and high density. Examples of fires originating in confined, narrow spaces abound, whether rare cases like the Swissair flight 111 accident of 1998 or simple domestic and industrial electrical or appliance fires originating undetected in tight spaces. In fact, since these flames/flamelets operate or "survive" in near-limit environments, detection is an important practical matter. A miniature flamelet is essentially an active ignition source or pilot flame, which will ignite into full flaming with inflow of fresh oxidizer. Once ignition occurs the flamelet undergoes transition into full, active flaming as a nascent fire. This scenario represents the most deadly feature of such near-limit flames.

Two-dimensional simulations in a narrow channel demonstrate, for small gap heights, that most of the gravitationally-induced buoyant flow caused by the flame is suppressed and has a negligible effect on the flow pattern for inlet velocities ≥ 5 cm/s. These calculations suggest that when buoyancy is suppressed or eliminated the other velocities in the system (blowing, thermal expansion, and diffusion) are all of the same order of magnitude, approximately 10-20% of the inflow velocity, and that when the inflow is correspondingly reduced to this level the flamelet phenomenon appears in the experiments. The results indicate that the buoyancy-suppressing NCA quantitatively captures the essential features of microgravity tests for thin fuels, and thus provides a viable method to study non-buoyant flame spread in a normal gravity laboratory without the limitations of actual low-gravity testing in ground-based drop facilities including the test time and cost.

11.6. Recommendations and future work: Flame Spread in Microgravity

Although the applicability of 2-D FLUENT simulations to the case of 3-D flamelets is not certain, the current 2-D model represented at present a viable simulation. A numerical effort at full-scale simulation can be attempted by upgrading the simulation strategy used in this work. Preliminary 3-D simulations using the NIST Fire Dynamics

Simulator (FDS) code were attempted. Flamelets were successfully produced over thin cellulosic fuels, however, at least four drawbacks were realized: 1) the solid thermal decomposition and the oxidizing kinetics of volatiles are simple and empirical even in the MSU modified code using the two-step Broido-Shafizadeh reaction scheme for cellulosic solid phase pyrolysis; 2) flamelet phenomenon was reproduced only with a non-realistic oxygen concentration of 47%; 3) the radiation mechanism was simple; 4) The computational time was excessively long. More work is needed in the 3-D modeling.

For the 2-D scaling analysis, it would be interesting to investigate whether the Narrow Channel in *1g* is the same as (or similar to) not having a channel top wall at all in *0g*. This can be shown by simulating the narrow channel with a large gap spacing (e.g., $h = 50\ mm$) in zero-gravity.

Appendix A

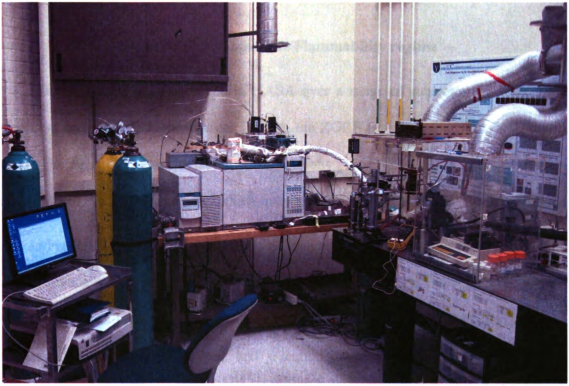

Figure A-1. Photograph of the experimental setup at Yale University. Right: the counterflow burner setup; center: the GC/MS setup; left: the data acquisition system.

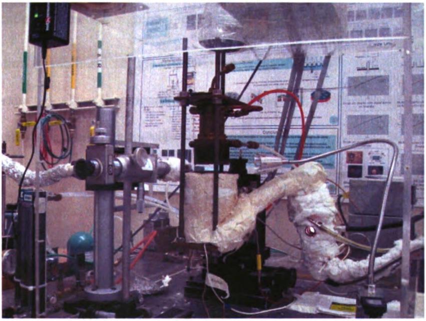

Figure A-2. The counterflow burner setup at Yale University.

Appendix B

Flammability maps: The Flammability regime

Flamelets have been observed in NASA over a range of substrate spacings, flow velocities, and oxygen concentrations in both the ZGRF tests and the NCA in both the upward facing and downward facing configurations [155]. The test results are used to make maps of the flamelet regime, which invariably occurs at the edge of flammability.

In Figure B-1, the flamelet regime is delineated by flow velocity and heat loss. The latter is inversely proportional to substrate spacing, as shown on the right axis. As the velocity decreases for a given heat loss (moving left on the figure), the flame becomes corrugated, breaks into flamelets, and eventually extinguishes at sufficiently low velocities. For a given velocity (5 cm/s), as the heat loss is increased (substrate spacing reduced, moving up on the figure), the same sequence of events occurs, with eventual extinguishment at sufficiently high heat loss values.

In addition to the baseline upward facing tests in the NCA, downward facing tests have been conducted where the apparatus was turned upside down so that the positions of the copper substrate and quartz viewing window were reversed. The goal of the downward facing tests was to determine whether the gravitational influence in the *1g* tests had been eliminated altogether, or whether the reversal of *g* would manifest itself in a variation in flame behavior. The results shown in Figure B-1 indicate that the flamelet and quenching boundaries are similar, though slightly narrower in the downward facing geometry. These differences indicate a limited role of gravity in the flame behavior.

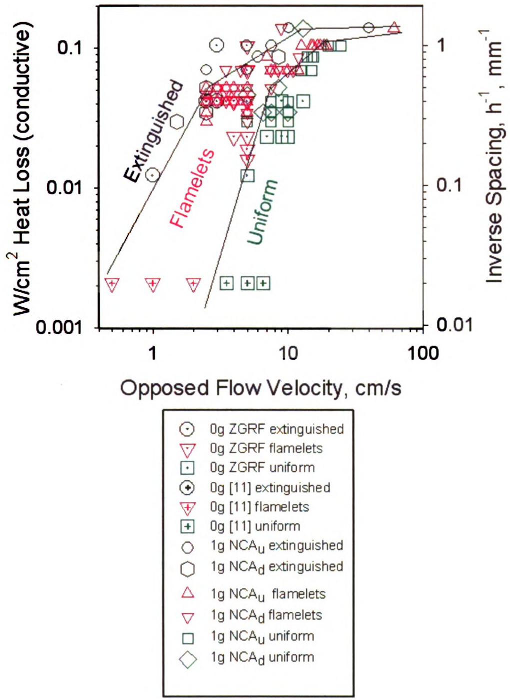

Figure B-1. Flammability map with opposed flow velocity and heat loss as axes, showing good agreement between Zero Gravity Research Facility tests and normal gravity tests in the NCA, both in the 'u'=upward facing orientation and 'd'=downward facing orientation [180, 181]. The flamelet regime is a near-limit zone. 0g data with 0.02 mm^{-1} spacing is from [185].

References

[1] G. Coppola, B. Coriton, and A. Gomez, "Highly turbulent counterflow flames: A laboratory scale benchmark for practical systems," *Combustion and Flame*, vol. 156, pp. 1834, 2009.

[2] T. Edwards and L. Q. Maurice, *J. Propuls. Power*, vol. 17(2), pp. 461–466, 2001.

[3] M. Colket, T. Edwards, S. Williams, N. P. Cernansky, D. L. Miller, F. Egolfopoulos, P. Lindstedt, K. Seshadri, F. L. Dryer, C. K. Law, D. Friend, D. B. Lenhert, H. Pitsch, A. Sarofim, M. Smooke, and W. Tsang, presented at 45th AIAA Aerospace Sci. Meet. Exhibit, 2007.

[4] P. Dagaut and M. Cathonnet, *Prog. Energy Combust. Sci.*, vol. 32, pp. 48-92, 2006.

[5] C. P. Wood, V. G. McDonell, R. A. Smith, and G. S. Samuelson, "Development and Application of a Surrogate Distillate Fuel," *J. Propuls. Power*, vol. 5, pp. 399-405, 1989.

[6] W. D. Schulz, "Oxidation Products of a Surrogate JP-8 Fuel," *ACS Petroleum Chemistry Division Preprints*, vol. 37, pp. 383-392, 1991.

[7] A. Violi, E. G. Eddings, A. F. Sarofim, S. Granata, T. Faravelli, and E. Ranzi, *Comb. Sci. and Tech.*, vol. 174, pp. 399-417, 2002.

[8] A. Agosta, N. P. Cernansky, D. L. Miller, T. Faravelli, and E. Ranzi, *Exp. Therm. Fluid Sci.*, vol. 28, pp. 701-708, 2004.

[9] C. J. Montgomery, S. M. Cannon, M. A. Mawid, and B. Sekar, "Reduced chemical kinetic mechanisms for JP-8 combustion," presented at 40th AIAA Aerospace Sci. Meet. Exhibit, Reno, Nevada, 2002.

[10] S. Humer, A. Frassoldati, S. Granata, T. Faravelli, E. Ranzi, R. Seiser, and K. Seshadri, *Proc. Combust. Inst.*, vol. 31, pp. 393-400, 2007.

[11] S. Honnet, K. Seshadri, U. Niemann, and N. Peters, "A Surrogate Fuel for Kerosene," *Proc. Combust. Inst.*, vol. 32, pp. 485-492, 2009.

[12] R. H. Natelson, M. Kurman, N. P. Cernansky, and D. L. Miller, *Fuel*, vol. 87, pp. 2339-2342, 2008.

[13] A. T. Holley, Y. Dong, M. G. Andac, F. N. Egolfopoulos, and T. Edwards, *Proc. Combust. Inst.*, vol. 31, pp. 1205–1213, 2007.

[14] S. S. Vasu, D. F. Davidson, and R. K. Hanson, *Combust. Flame*, vol. 152, pp. 125-143, 2008.

[15] E. Ranzi, available at: http://www.chem.polimi.it/CRECKModeling/kinetic.html, 2006.

[16] H. R. Zhang, E. G. Eddings, and A. F. Sarofim, *Proc. Combust. Inst.*, vol. 31, pp. 401–409, 2007.

[17] S. S. Vasu, D. F. Davidson, Z. Hong, V. Vasudevan, and R. K. Hanson, *Proc. Combust. Inst.*, pp. in press, 2009.

[18] S. S. Vasu, D. F. Davidson, and R. K. Hanson, *Combust. Flame*, pp. in press, 2009.

[19] T. Edwards, D. Minus, W. Harrison, E. Corporan, M. DeWitt, S. Zabarnick, and L. Balster, "Fischer-Tropsch Jet Fuels – Characterization for Advanced Aerospace Applications," presented at 40th AIAA/ASME/SAE/ASEE Joint Propuls. Conf. Exhibit, 2004.

[20] *A Review of United States Air Force and Department of Defense Aerospace Propulsion Needs*: Air Force Studies Board, The National Academic Press, Washington, D.C., 2006.

[21] L. Shafer, R. Striebich, J. Gomach, and T. Edwards, "Chemical Class Composition of Commercial Jet Fuels and Other Specialty Kerosene Fuels," *AIAA Paper 2006-7972*, 2006.

[22] T. J. Bruno and B. L. Smith, "Improvements in the Measurement of Distillation Curves - Part 2: Application to Aerospace/Aviation Fuels RP-1 and S-8," *Ind. Eng. Chem. Res.*, vol. 45, pp. 4381-4388, 2006.

[23] R. H. Natelson, M. S. Kurman, M. D. L., and N. P. Cernansky, "Oxidation of Alternative Jet Fuels and their Surrogate Components," presented at 46th AIAA Aerospace Sciences Meeting and Exhibit, 2008.

[24] M. S. P. Kahandawala, M. J. DeWitt, E. Corporan, and S. S. Sidhu, "Ignition and emission characteristics of surrogate and practical jet fuels," *Energy and Fuels*, vol. 22, pp. 3673, 2008.

[25] M. A. Mawid, "Development of a detailed chemical kinetic mechanism for JP-8 and Fischer-Tropsch-derived synthetic jet fuels," presented at 43rd AIAA/ASME/SAE/ASEE Joint Propulsion Conference, Reston, VA 20191-4344, United States, 2007.

[26] V. R. Katta, M. Mawid, B. Sekar, E. Corporan, J. Zelina, W. M. Roquemore, and C. J. Montgomery, "Comparison of chemical-kinetics models for JP-8 fuel in predicting premixed and nonpremixed flames," presented at AIAA/ASME/SAE/ASEE 42nd Joint Propulsion Conference, Reston, VA 20191-4344, United States, 2006.

[27] H. Pitsch, "FlameMaster, A C++ Computer Program for 0D Combustion and 1D Laminar Flame Calculations, Tech. rep., Institut f¨ur Technische Verbrennung, RWTH Aachen, may be downloaded from http://www.stanford.edu/group/pitsch/CES.htm."

[28] CHEMKIN 4.1 by Reaction Design Inc.

[29] P. Dagaut, A. El Bakali, and A. Ristori, "The combustion of kerosene: Experimental results and kinetic modelling using 1- to 3-component surrogate model fuels," *Fuel*, vol. 85, pp. 944, 2006.

[30] R. J. Kee, J. F. Grcar, M. D. Smooke, and J. A. Miller, "PREMIX: a Fortran program for modelling steady laminar one-dimensional premixed flame," Sandia Report SAND85-8240. Livermore, CA: Sandia National Laboratories, 1985.

[31] P. Glarborg, R. J. Kee, J. F. Grcar, and J. A. Miller, "PSR: a Fortran program for modeling well-stirred reactors," Sandia Report No.SAND86-8209. Livermore, CA: Sandia National Laboratories, 1986.

[32] A. E. Lutz, R. J. Kee, J. F. Grcar, and F. M. Rupley, "OPPDIF: A Fortran Program for Computing Opposed-Flow Diffusion Flames," *SAND96-8243, Unlimited Release*, 1996.

[33] J. A. Cooke, M. Bellucci, M. D. Smooke, A. Gomez, A. Violi, T. Faravelli, and E. Ranzi, *Proc. Combust. Inst.*, vol. 30, pp. 439-446, 2005.

[34] H. Bufferand, L. Tosatto, B. L. Mantia, M. D. Smooke, and A. Gomez, *Revised paper submitted to Combust. Flame*, 2008.

[35] D. E. Rosner, *Transport Processes in Chemically Reacting Flow Systems*. Mineola, New York: Dover Publications Inc., 2000.

[36] H. Bufferand, L. Tosatto, B. La Mantia, M. D. Smooke, and A. Gomez, "Experimental and computational study of methane counterflow diffusion flames perturbed by trace amounts of either jet fuel or a 6-component surrogate under non-sooting conditions," *Combustion and Flame*, vol. 156, pp. 1594-1603, 2009.

[37] S. Jahangirian, C. S. McEnally, and A. Gomez, "Experimental study of ethylene counterflow diffusion flames perturbed by trace amounts of jet fuel and jet fuel surrogates under incipiently sooting conditions," *Combustion and Flame*, vol. 156, pp. 1799–1809, 2009.

[38] T. Lu and C. K. Law, "Toward accommodating realistic fuel chemistry in large-scale computations," *Progress in Energy and Combustion Science*, vol. 35, pp. 192, 2009.

[39] T. Lu and C. K. Law, "Strategies for mechanism reduction for large hydrocarbons: n-heptane," *Combustion and Flame*, vol. 154, pp. 153, 2008.

[40] T. Lu and C. K. Law, "Linear time reduction of large kinetic mechanisms with directed relation graph: n-Heptane and iso-octane," *Combustion and Flame*, vol. 144, pp. 24, 2006.

[41] T. Lu and C. K. Law, "On the applicability of directed relation graphs to the reduction of reaction mechanisms," *Combustion and Flame*, vol. 146, pp. 472, 2006.

[42] P. Pepiot-Desjardins and H. Pitsch, "An efficient error-propagation-based reduction method for large chemical kinetic mechanisms," *Combustion and Flame*, vol. 154, pp. 67, 2008.

[43] P. Pepiot-Desjardins and H. Pitsch, "An automatic chemical lumping method for the reduction of large chemical kinetic mechanisms," *Combustion Theory and Modelling*, vol. 12, pp. 1089, 2008.

[44] A. Gomez, B. L. Manita, L. Tosatto, and H. Bufferand, "Manual of the GC/MS System for Probing the Chemcical Structure of Flames," Yale University 2008.

[45] L. Tosatto, B. L. Mantia, H. Bufferand, P. Duchaine, and A. Gomez, *Proc. Combust. Inst.*, in press, 2009.

[46] L. Tosatto, B. L. Mantia, H. Bufferand, P. Duchaine, and A. Gomez, "Chemical structure of a methane counterflow diffusion flame perturbed with the addition of either JP-8 or a jet fuel surrogate," *Proceedings of the Combustion Institute*, vol. 32, pp. 1319, 2009.

[47] G. Bikas, *Kinetic Mechanisms for Hydrocarbon Ignition, Doktor der Ingenieurwissenschaften thesis, http://deposit.ddb.de/cgi-bin/dokserv?idn=964932857, RWTH Aachen University, Fakult¨at f¨ur Maschinenwesen*, 2001.

[48] E. Ranzi, M. Dente, G. Bozzano, A. Goldaniga, and T. Faravelli, *Prog. Energ. Combust. Sci.*, vol. 27, pp. 99–139, 2001.

[49] C. K. Law, *Combustion Physics*. New York: Cambridge University Press, 2006.

[50] K. Seshadri and F. A. Williams, "Laminar flow between parallel plates with injection of a reactant at high Reynolds number," *Intl. J. Heat Mass Transfer*, vol. 21, pp. 251–253, 1978.

[51] M. H. Duby, W. Deng, K. Kim, T. Gomez, and A. Gomez, "Monodisperse Electrospray Multiplexing in the Multi-Jet Mode," *Journal Aerosol Sci.*, vol. 37, pp. 306-322, 2006.

[52] C. Shaddix, K. Brezinsky, and I. Glassman, *Proc. Combust. Inst.*, vol. 24, pp. 683–690, 1992.

[53] R. G. Butler and I. Glassman, *Proc. Combust. Inst.*, pp. in press, 2009.

[54] A. Hamins, D. T. Anderson, and J. H. Miller, "Mechanistic studies of toluene destruction in diffusion flames," *Combust. Sci. Technol.*, vol. 71, pp. 175–95, 1990.

[55] C. S. McEnally and L. D. Pfefferle, *Combust. Sci. Technol.*, vol. 131, pp. 323–44, 1998.

[56] C. S. McEnally, L. D. Pfefferle, B. Atakan, and K. Kohse-Höinghaus, *Prog. Energy Combust. Sci.*, vol. 32, pp. 247-294, 2006.

[57] I. Glassman, *Combustion*, 3rd ed: Academic Press, 1996.

[58] A. Gomez, G. Sidebotham, and I. Glassman, *Combust. Flame*, vol. 58, pp. 45-57, 1984.

[59] R. L. Axelbaum, W. L. Flower, and C. K. Law, "Dilution And Temperature Effects Of Inert Addition On Soot Formation In Counterflow Diffusion Flames," *Combust. Sci. Technol.*, vol. 61, pp. 51-73, 1988.

[60] B. M. Kumfer, S. A. Skeen, and R. L. Axelbaum, *Combust. Flame*, vol. 154, pp. 546–556, 2008.

[61] T. Edwards, *J. Propuls. Power*, vol. 19, pp. 1089–1107, 2003.

[62] D. C. Rapp: Pennsylvania State University, PA, 1996.

[63] R. M. Fristrom, *Flame Structure and Processes*. New York: Oxford University Press, 1995.

[64] B. A. V. Bennett, C. S. McEnally, L. D. Pfefferle, M. D. Smooke, and M. B. Colket, "Computational and experimental study of axisymmetric coflow partially premixed ethylene/air flames," *Combust. Flame*, vol. 127, pp. 2004-2022, 2001.

[65] H. R. Zhang, E. G. Eddings, and A. F. Sarofim, "Criteria for selection of components for surrogates of natural gas and transportation fuels," *Proceedings of the Combustion Institute*, vol. 31, pp. 401, 2007.

[66] H. R. Zhang, E. G. Eddings, A. F. Sarofim, and C. K. Westbrook, "Fuel dependence of benzene pathways," *Proceedings of the Combustion Institute*, vol. 32, pp. 377, 2009.

[67] Y. Yang, A. L. Boehman, and R. J. Santoro, *Combust. Flame*, vol. 149, pp. 191–205, 2007.

[68] H. F. Calcote and D. M. Manos, *Combust. Flame*, vol. 49, pp. 289-304, 1983.

[69] S. R. Turns, *An Introduction to Combustion,* 2nd ed., McGraw-Hill, 2000.

[70] Z. Yang, M. Chaos, and F. L. Dryer, *"Surrogate Composition Effects: A Comparison of Surrogate Mixture Candidates with Combustion Targets (H/C, TSI, CN)", presented at the Surrogate Fuels Working Group meeting, January 6th 2008, Reno, Nevada. Available at: MURI website.*, 2006.

[71] D. B. Olson, J. C. Pickens, and R. J. Gill, *Combust. Flame*, vol. 62, pp. 43-60, 1985.

[72] R. C. Santana, P. T. Do, M. Santikunaporn, W. E. Alvarez, J. D. Taylor, E. L. Sughrue, and D. E. Resasco, "Evaluation of different reaction strategies for the improvement of cetane number in diesel fuels," *Fuel*, vol. 85, pp. 643, 2006.

[73] C. P. Henry, *Enhanced Antistatic Additives for Hydrocarbon Fuels and Solvents, US Patent No. US2007/0220803 A1*, 2007.

[74] R. K. Cheng, D. Littlejohn, W. A. Nazeer, and K. O. Smith, "Laboratory Studies of the Flow Field Characteristics of Low-swirl Injectors for Adaption to Fuel-Flexible Turbines," presented at Proceedings of GT2006 ASME Turbo Expo 2006, GT2006-90878.

[75] <http://bio-fuelsources.com/>.

[76] P. Griebel, R. Bombach, A. Inauen, Schären R., S. Schenker, and P. Siewert, "Flame characteristics and turbulent flame speeds of turbulent high-pressure lean premixed methane/air flames," *ASME paper GT2005-68565*, 2005.

[77] A. Wellinger and A. Lindberg, "Biogas Upgrading and Utilization," *IEA Bioenergy Task 24: Energy from biological conversion of organic waste.*

[78] A. Rojey, *Natural Gas Production, Processing and Transport*. Technip, Paris, 1996.

[79] G. P. Smith, D. M. Golden, M. Frenklach, N. W. Moriarty, B. Eiteneer, M. Goldenberg, C. T. Bowman, R. K. Hanson, S. Song, W. C. Gardiner, V. V. L. Jr., and Z. Qin, "GRI-Mech 3.0," *http://www.me.berkeley.edu/gri_mech/*, 2000.

[80] N. R. Scott, S. Zicari, K. Saikkonen, and K. Bothi, "Characterization of Dairy-Derived Biogas and Biogas Processing," presented at 2006 ASABE Annual International Meeting, Portlan, Oregan, 2006.

[81] I. Gokalp and E. Lebas, "Alternative Fuels for Industrial Gas Turbines (AFTUR)," *Applied Thermal Engineering*, vol. 24, pp. 1655, 2004.

[82] M. Persson, "Biogas Upgrading and Utilization as Vehicle Fuel," *Proceeding of The Future of Biogas in Europe III: Visions and Targets 2020, European Biogas Workshop, University of Southern Denmark, Esbjerg, Denmark*, 2007.

[83] M. N. Sannaa, "The Development of Biogas Technology in Denmark: Achievements & Obstacles," in *Department of Environment, Technology and Social Studies, Roskilde University RUC, Denmark*, 2004.

[84] P. A. Gerin, F. Vliegen, and J.-M. Jossart, "Energy and CO_2 Balance of Maize and Grass as Energy Crops for Anaerobic Digestion," *Bioresource Technology*, vol. 99, pp. 2620, 2008.

[85] P. Börjesson and M. Berglund, "Environmental systems analysis of biogas systems-Part I: Fuel-cycle emissions," *Biomass and Bioenergy*, vol. 30, pp. 469, 2006.

[86] Y. Lafay, B. Taupin, G. Martins, G. Cabot, B. Renou, and A. Boukhalfa, "Experimental study of biogas combustion using a gas turbine configuration," *Experiments in Fluids*, vol. 43, pp. 395, 2007.

[87] United States Environmental Protection Agency (EPA) web page. Available online at www.epa.gov.

[88] R. Bütikofer, "Biotech to Biofuels: How New Technologies are Changing Transatlantic Relations," *Energy Security and Global Warming Conference, San Diego*, 2007.

[89] J. B. Holm-Nielsen, "The future of biogas in Europe III: Visions and Targets 2020," *European Biogas Workshop and Study Trip, University of Southern Denmark, Esbjerg, Denmark*, 2007.

[90] M. Moliere, "Expanding fuel flexibility of gas turbines," *Proc. IMechE Vol. 219 Part A: J. Power and Energy*, pp. 109, 2005.

[91] D. Yomogida and N. D. Thinh, "Thermal analysis of a simple-cycle gas turbine in biogas power generation," presented at Proceedings of the Heat Transfer and Fluid Mechanics Institute, 1995.

[92] D. E. Yomogida, N. D. Thinh, V. M. Tiangco, and Y. Lee, "Thermal efficiency projections of a simple-cycle gas turbine in biogas power generation," presented at American Society of Mechanical Engineers, Burmingham, UK, 1996.

[93] C. A. Palmer and M. R. Erbes, "Simulation methods used to analyze the performance of the GE PG6541B gas turbine utilizing low heating value fuels," presented at American Society of Mechanical Engineers, International Gas Turbine Institute (Publication) IGTI, Portland, OR, USA.

[94] H. Hanagudu, "Biogas fired industrial gas turbines a technological and potential assessment," presented at American Society of Mechanical Engineers (Paper), Cincinnati, OH, USA.

[95] G. Wiltsee and H. Emerson, "Clean power from microturbines using biogas," *BioCycle*, vol. 45, pp. 53, 2004.

[96] B. Krautkremer and J. Muller, "Mikrogasturbine - Eine Alternative zur Nutzung von Biogas (Micro gas turbine - An alternative use of biogas)," *VDI Berichte*, pp. 181, 2005.

[97] N. Goldstein, "Microturbines, gas engines link biogas to the grid," *BioCycle*, vol. 47, pp. 59, 2006.

[98] E. Wheless and J. Pierce, " Siloxanes in Landfill and Digester Gas Update," *Los Angeles County Sanitation Districts and SCS Energy, California*, 2004.

[99] E. J. Dolak and J. P. Armstrong, "The correlation of IR microturbine combustion performance while burning diluted gaseous fuel supplied by a fuel mixing facility," presented at Proceedings of the ASME Turbo Expo, Reno-Tahoe, NV, United States.

[100] S. Naing, T. Yamada, and K. Nakanishi, "Analysis of micro gas turbine cogeneration system with biogas storage," presented at Collection of Technical Papers - 4th International Energy Conversion Engineering Conference, San Diego, CA, USA.

[101] D. Bohn and J. Lepers, "Effects of biogas combustion on the operation characteristics and pollutant emissions of a micro gas turbine," presented at American Society of Mechanical Engineers, International Gas Turbine Institute, Turbo Expo (Publication) IGTI, Atlanta, GA, United States.

[102] M. R. Johnson, D. Littlejohn, W. A. Nazeer, K. O. Smith, and R. K. Cheng, "A comparison of the flowfields and emissions of high-swirl injectors and low-swirl injectors for lean premixed gas turbines," *Proceedings of the Combustion Institute*, vol. 30, pp. 2867, 2005.

[103] H. C. Mongia, Held, T.J., Hsiao, G.C. and Pandalai, R.P., "Challenges and progress in controlling dynamics in gas turbine combustors," *Journal of Propulsion and Power*, vol. 19(5), pp. 822-829, 2003.

[104] D. Littlejohn and R. K. Cheng, "Fuel effects on a low-swirl injector for lean premixed gas turbines," *Proceedings of the Combustion Institute*, vol. 31, pp. 3155, 2007.

[105] Y. Lafay, "Biogas Combustion in Gas Turbines," P. Communication, Ed., October 2007.

[106] T. Leung and I. Wierzba, "The effect of hydrogen addition on biogas non-premixed jet flame stability in a co-flowing air stream," *International Journal Of Hydrogen Energy*, vol. 33, pp. 3856-3862, 2008.

[107] M. Zheng, G. T. Reader, and J. G. Hawley, "Diesel engine exhaust gas recirculation--a review on advanced and novel concepts," *Energy Conversion and Management*, vol. 45, pp. 883, 2004.

[108] J. Staniforth and K. Kendall, "Biogas powering a small tubular solid oxide fuel cell," *Journal of Power Sources*, vol. 71, pp. 275, 1998.

[109] J. Staniforth and K. Kendall, "Cannock landfill gas powering a small tubular solid oxide fuel cell -- a case study," *Journal of Power Sources*, vol. 86, pp. 401, 2000.

[110] K. Kendall, C. M. Finnerty, G. Saunders, and J. T. Chung, "Effects of dilution on methane entering an SOFC anode," *Journal of Power Sources*, vol. 106, pp. 323, 2002.

[111] H. Kobayashi, H. Hagiwara, H. Kaneko, and Y. Ogami, "Effects of CO_2 dilution on turbulent premixed flames at high pressure and high temperature," *Proceedings of the Combustion Institute*, vol. 31, pp. 1451, 2007.

[112] B. J. P. Buhre, L. K. Elliott, C. D. Sheng, R. P. Gupta, and T. F. Wall, "Oxy-fuel combustion technology for coal-fired power generation," *Progress in Energy and Combustion Science*, vol. 31, pp. 283, 2005.

[113] F. H. V. Coppens and A. A. Konnov, "The effects of enrichment by H_2 on propagation speeds in adiabatic flat and cellular premixed flames of $CH_4+O_2+CO_2$," *Fuel*, vol. 87, pp. 2866-2870, 2008.

[114] P. Glarborg and L. L. B. Bentzen, "Chemical effects of a high CO_2 concentration in oxy-fuel combustion of methane," *Energy & Fuels*, vol. 22, pp. 291-296, 2008.

[115] S. C. Li and F. A. Williams, "NOx formation in two-stage methane-air flames," *Combustion and Flame*, vol. 118, pp. 399, 1999.

[116] T. Lieuwen, V. McDonell, E. Petersen, and D. Santavicca, "Fuel flexibility influences on premixed combustor blowout, flashback, autoignition, and stability," *Proceedings of the ASME Turbo Expo*, vol. 1, pp. 601-615, 2006.

[117] C. Zhang, A. Atreya, and K. Lee, "Sooting structure of methane counterflow diffusion flames with preheated reactants and dilution by products of combustion," *Twenty-Fourth Symposium (International) on Combustion, The Combustion Institute, Pittsburgh*, pp. 1049, 1992.

[118] A. R. Masri, Dibble, R.W., Barlow, R.S., *Combustion and Flame*, vol. 91, pp. 285-309, 1992.

[119] F. S. Liu, H. S. Guo, G. J. Smallwood, and O. L. Gulder, "The chemical effects of carbon dioxide as an additive in an ethylene diffusion flame: Implications for soot and NOx formation," *Combustion And Flame*, vol. 125, pp. 778-787, 2001.

[120] F. Liu, H. Guo, and G. J. Smallwood, "The chemical effect of CO2 replacement of N2 in air on the burning velocity of CH4 and H2 premixed flames," *Combustion and Flame*, vol. 133, pp. 495, 2003.

[121] J. Park, D. J. Hwang, K.-T. Kim, S.-B. Lee, and S.-I. Keel, "Evaluation of chemical effects of added CO_2 according to flame location," *International Journal of Energy Research*, vol. 28, pp. 551, 2004.

[122] H. Guo and G. J. Smallwood, "A numerical study on the influence of CO_2 addition on soot formation in an ethylene/air diffusion flame," *Combustion Science and Technology*, vol. 180, pp. 1695-1708, 2008.

[123] D.-J. Hwang, J. Park, C.-B. Oh, K.-H. Lee, and S.-I. Keel, "Numerical study on NO formation in CH_4-O_2 -N_2 diffusion flame diluted with CO_2," *International Journal of Energy Research*, vol. 29, pp. 107, 2005.

[124] J. Park, S.-G. Kim, K.-M. Lee, and K. Kim, "Chemical effect of diluents on flame structure and NO emission characteristic in methane-air counterflow diffusion flame," *International Journal of Energy Research*, vol. 26, pp. 1141, 2002.

[125] J. Park, J. S. Park, H. P. Kim, J. S. Kim, S. C. Kim, J. G. Choi, H. C. Cho, K. W. Cho, and H. S. Park, "NO emission behavior in oxy-fuel combustion recirculated with carbon dioxide," *Energy and Fuels*, vol. 21, pp. 121, 2007.

[126] F. Hermann, T. Zeuch, and J. Klingmann, "The effect of diluents on the formation rate of nitrogen oxide in a premixed laminar flame," presented at ASME Turbo Expo 2004, Vienna, Austria, 2004.

[127] S. Gordon and B. J. McBride, "Computer Program for Calculation of Complex Chemical Equilibrium Compositions, Rocket Performance, Incident and Reflected Shocks and Chapman-Jouguet Detonations," NASA Report SP-273 1971.

[128] G. P. Smith, D. M. Golden, M. Frenklach, N. W. Moriarty, B. Eiteneer, M. Goldenberg, C. T. Bowman, R. K. Hanson, S. Song, W. C. Gardiner, V. V. L. Jr., and Z. Qin, "GRI-Mech 3.0," *http://www.me.berkeley.edu/gri_mech/*.

[129] San Diego reaction mechanism, Center for Energy Research, UC San Diego, Available online at: http://maeweb.ucsd.edu/~combustion/.

[130] J. Li, "Experimental and Numerical Studies of Ethanol Chemical Kinetics," Ph.D. Thesis, Princeton University, 2004.

[131] R. G. Gilbert, K. Luther, and J. Troe, "Theory of thermal unimolecular reactions in the fall-off range. ii. weak collision rate constants," *Ber. Bunsenges. Phys. Chem.*, vol. 87, pp. 169-177, 1983.

[132] J. C. Hewson and M. Bollig, "Reduced mechanisms for NOx emissions from hydrocarbon diffusion flames," *Twenty-Sixth Symposium (International) on Combustion, The Combustion Institute*, pp. 2171–2179, 1996.

[133] C. T. Bowman, R. K. Hanson, D. F. Davidson, J. W. C. Gardiner, V. Lissianski, G. P. Smith, D. M. Golden, M. Frenklach, and M. Goldenberg, "Gri-mech 2.11," in *http://www.me.berkeley.edu/gri mech/*.

[134] A. Kazakov and M. Frenklach, "Reduced Reaction Sets based on `GRI-Mech 1.2`," *http://www.me.berkeley.edu/drm/*.

[135] C. J. Sung, J. B. Liu, and C. K. Law, "Structural response of counterflow diffusion flames to strain rate variations," *Combustion and Flame*, vol. 102, pp. 481, 1995.

[136] A. E. Lutz, R. J. Kee, J. F. Grcar, and F. M. Rupley, "OPPDIF: A Fortran Program for Computing Opposed-Flow Diffusion Flames," *SAND96-8243, Unlimited Release*, 1996.

[137] R. J. Kee, J. A. Miller, and G. H. Evans, "A computational medel of the structure and extinction of strained, opposed flow, premixed methane–air flame,"

Proceedings of the 22nd Symposium (International) on Combustion. The Combustion Institute, pp. 1479, 1988.

[138] N. Peters and R. J. Kee, *Combustion and Flame*, vol. 68, pp. 17-29, 1987.

[139] M. V. Petrova and F. A. Williams, "A small detailed chemical-kinetic mechanism for hydrocarbon combustion," *Combustion and Flame*, vol. 144, pp. 526, 2006.

[140] L. J. Spadaccini and M. B. Colket Iii, "Ignition delay characteristics of methane fuels," *Progress in Energy and Combustion Science*, vol. 20, pp. 431, 1994.

[141] E. L. Petersen, J. M. Hall, S. D. Smith, J. de Vries, A. R. Amadio, and M. W. Crofton, "Ignition of lean methane-based fuel blends at gas turbine pressures," *Journal Of Engineering For Gas Turbines And Power-Transactions Of The Asme*, vol. 129, pp. 937-944, 2007.

[142] F. N. Egolfopoulos, D. X. DU, and C. K. Law, *Combustion Science and Technology*, vol. 83, pp. 33-75, 1992.

[143] F. N. Egolfopoulos, D. L. Zhu, and C. K. Law, *Twenty-Third Symposium (International) on Combustion, The Combustion Institute*, pp. 471-478, 1990.

[144] H. Kobayashi, K. Seyama, H. Hagiwara, and Y. Ogami, "Burning velocity correlation of methane/air turbulent premixed flames at high pressure and high temperature," *Proceedings of the Combustion Institute*, vol. 30, pp. 827, 2005.

[145] M. Metghalchi and J. C. Keck, *Combustion and Flame*, vol. 38, pp. 143–157, 1980.

[146] S. Jahangirian, A. Engeda, and I. S. Wichman, "Thermal and chemical structure of biogas counterflow diffusion flames," *Energy and Fuels,* Published online October 9, DOI:10.1021/ef9002044, 2009.

[147] G. J. Rortveit, J. E. Hustad, S.-C. Li, and F. A. Williams, "Effects of diluents on NOx formation in hydrogen counterflow flames," *Combustion and Flame*, vol. 130, pp. 48, 2002.

[148] T. L. Berry Yelverton and W. L. Roberts, "Soot surface temperature measurements in pure and diluted flames at atmospheric and elevated pressures," *Experimental Thermal and Fluid Science*, vol. 33, pp. 17, 2008.

[149] F. Liu, H. Guo, G. J. Smallwood, and O. L. Gulder, "The chemical effects of carbon dioxide as an additive in an ethylene diffusion flame: implications for soot and NOx formation," *Combustion and Flame*, vol. 125, pp. 778, 2001.

[150] K. P. Schug, Y. Manheimer-Timnat, P. Yaccarino, and I. Glassman, "Sooting Behavior of Gaseous Hydrocarbon Diffusion Flames and the Influence of Additives," *Combustion Science and Technology*, vol. 22, pp. 235, 1980.

[151] D. X. Du, R. L. Axelbaum, and C. K. Law, "The influence of carbon dioxide and oxygen as additives on soot formation in diffusion flames," *Symposium (International) on Combustion*, vol. 23, pp. 1501-1507, 1990.

[152] S. Jahangirian and A. Engeda, "Biogas Combustion and Chemical Kinetics for Gas Turbine Applications," *Proceedings of 2008 ASME International Mechanical Engineering Congress and Exposition, Boston, USA, IMECE2008-66667.*

[153] J. A. van-Aardenne, F. D. Dentener, J. G. J. Olivier, J. A. H. W. Peters, and L. N. Ganzeveld, "Emission Database for Global Atmospheric Research," *The EDGAR 3.2 Fast Track 2000 dataset (32FT2000)*, 2005.

[154] Y. Long and I. S. Wichman, "Structure of Attached Flames Spreading over Condensed Fuels," presented at Central States Sections Meeting, The Combustion Institute, 2005.

[155] S. L. Olson, F. J. Miller, S. Jahangirian, and I. S. Wichman, "Flame spread over thin fuels in actual and simulated microgravity conditions," *Combustion and Flame*, vol. 156, pp. 1214, 2009.

[156] Y. Long, "A Numerical Study of Flame Spread over Thin Cellulosic Fuels in Microgravity," in *Michigan State University, Ph.D. Thesis*, 2006.

[157] H. D. Ross, *Microgravity Combustion*. San Diego: Academic Press, 2001.

[158] I. S. Wichman, "Theory of Opposed-Flow Flame Spread," *Progress in Energy and Combustion Science*, vol. 18, pp. 553-593, 1992.

[159] L. Massa, T. L. Jackson, J. Buckmaster, and M. Campbell, "Three Dimensional Heterogeneous Propellant Combustion," *Proc. Comb. Inst.*, vol. 29, pp. 2975-2983, 2002.

[160] S. L. Olson, F. J. Miller, and I. S. Wichman, "Characterizing Fingering Flamelets Using the Logistic Model," *Combustion Theory and Modelling*, vol. 10, pp. 323-347, 2006.

[161] J. Buckmaster, "The Modeling of Heterogeneous Propellant Combustion," presented at Central States Sections Meeting, The Combustion Institute, 2006.

[162] J. N. DeRis, "Spread of a Laminar Diffusion Flame," *Proc. Comb. Inst.*, vol. 12, pp. 241-252, 1969.

[163] I. S. Wichman and F. A. Williams, "A Simplified Model of Flame Spread in an Opposed Flow along a Flat Surface of a Semi-Infinite Solid," *Combustion Science and Technology*, vol. 32, pp. 91-123, 1983.

[164] Y. Long, S. Jahangirian, and I. S. Wichman, "Flame-Surface Interaction and Flamelet Microstructure over Single and Multiple Solid Fuel Segments in a Channel Cross Flow," *Proceedings of the 2006 ASME International Mechanical Engineering Congress and Exposition, Chicago, USA, IMECE2006-15068*, 2006.

[165] S. Bhattachajee and R. A. Altenkirch, "The Effect of Surface Radiation on Flame Spread in a Quiescent Microgravity Environment," *Combustion and Flame*, vol. 84, pp. 160-169, 1991.

[166] V. Yang, T. B. Brill, and W. Z. Ren, "Solid Propellant Chemistry, Combustion, and Motor Interior Ballistics," *Progress in Astronautics and Aeronautics*, vol. 185, 2000.

[167] Transportation Safety Board of Canada Report Number A98H0003, 1998.

[168] L. M. Oravecz, I. S. Wichman, and S. L. Olson, *Proceedings of the 1999 ASME International Mechanical Engineering Congress and Exposition*, vol. 364-4, pp. 183-187, 1999.

[169] R. Friedman, B. Jackson, and S. Olson, "Testing and Selection of Fire-Resistant Materials for Spacecraft Use," *NASA TM-2000-209773*, 2000.

[170] R. Vance and I. S. Wichman, "Heat Transfer Analysis of a Diffusion Flame Leading Edge Near a Cold, Chemically Inert Surface," *International Journal of Heat And Mass Transfer*, vol. 43, pp. 921-933, 2000.

[171] I. S. Wichman, Z. Pavlova, B. Ramadan, and G. Qin, "Heat Flux from a Diffusion Flame Leading Edge to an Adjacent Surface," *Combustion and Flame*, vol. 118, pp. 652-668, 1999.

[172] I. S. Wichman, "On Diffusion Flame Attachment Near Cold Surfaces," *Combustion and Flame*, vol. 117, pp. 384-393, 1999.

[173] D. L. Urban, J. S. Goldmeer, and Z. G. Yuan, "Interactions between Flames on Parallel Solid Surfaces," presented at 4th Inter. Microg. Comb. Workshop. NASA CP–10194, 1997.

[174] S. Rouvreau, P. Joulain, H. Y. Wang, P. Cordeiro, and J. L. Torero, *Proc. Comb. Inst.*, vol. 29, pp. 2527-2534, 2002.

[175] P. Cordeiro, G. Legros, S. Rouvreau, P. Joulain, and J. L. Torero, " Detailed Description of the Structure of a Low Velocity Laminar Diffusion Flame in Microgravity," presented at 7th International Workshop on Microgravity Comb. and Chemically Reacting Systems, Cleveland, 2003.

[176] K. K. Kuo, *Principles of Combustion*: John Wiley & Sons, 1986.

[177] FLUENT Software, by ANSYS, Inc., WWW.FLUENT.COM.

[178] I. S. Wichman, L. M. Oravecz-Simpkins, and S. Tanaya, "Experimental Study of Flamelet Formation in a Hele-Shaw Flow," presented at 3rd Joint Mtg. U.S. Sections Combustion Institute, 2003.

[179] S. L. Olson, F. J. Miller, and I. S. Wichman, "Describing Near-Limit Flamelet Fingering Behavior Using Bio-Mathematical Population Models," presented at Fourth International Symposium on Scale Modeling, 2003.

[180] S. A. Tanaya, M.S. Thesis, in *Michigan State University*, 2004.

[181] K. L. Aditjandra, M.S. Thesis, in *Michigan State University*, 2005.

[182] I. S. Wichman, S. Tanaya, K. Aditjandra, L. Yang, S. L. Olson, and F. J. Miller, "A Simulated Zero-Gravity Flame Spread Apparatus," presented at Central States Section of the Combustion Institute Annual Meeting, Cleveland, OH, 2006.

[183] S. L. Olson, *Combust. Sci. Tech.*, vol. 76, pp. 233-249, 1991.

[184] T. Hirano, S. E. Noreikis, and T. E. Waterman, "Measured Velocity and Temperature Profiles Near Flames Spreading Over a Thin Combustible Solid," *Combustion and Flame*, vol. 23, pp. 83-96, 1974.

[185] S. L. Olson, T. Kashiwagi, O. Fujita, M. Kikuchi, and K. Ito, *Combustion and Flame*, vol. 125, pp. 852-864, 2001.